Atmos. Chem. Phys., 17, 15245–15270, 2017
https://doi.org/10.5194/acp-17-15245-2017

Atmospheric Chemistry and Physics
Open Access
EGU

BrO and inferred Br_y profiles over the western Pacific: relevance of inorganic bromine sources and a Br_y minimum in the aged tropical tropopause layer

Theodore K. Koenig[1,2], Rainer Volkamer[1,2], Sunil Baidar[1,2,a], Barbara Dix[1], Siyuan Wang[2,3,b], Daniel C. Anderson[4,c], Ross J. Salawitch[4,5,6], Pamela A. Wales[5], Carlos A. Cuevas[7], Rafael P. Fernandez[7,8], Alfonso Saiz-Lopez[7], Mathew J. Evans[9], Tomás Sherwen[9], Daniel J. Jacob[10,11], Johan Schmidt[12], Douglas Kinnison[13], Jean-François Lamarque[13], Eric C. Apel[13], James C. Bresch[13], Teresa Campos[13], Frank M. Flocke[13], Samuel R. Hall[13], Shawn B. Honomichl[13], Rebecca Hornbrook[13], Jørgen B. Jensen[13], Richard Lueb[13], Denise D. Montzka[13], Laura L. Pan[13], J. Michael Reeves[13], Sue M. Schauffler[13], Kirk Ullmann[13], Andrew J. Weinheimer[13], Elliot L. Atlas[14], Valeria Donets[14], Maria A. Navarro[14], Daniel Riemer[14], Nicola J. Blake[15], Dexian Chen[16,d], L. Gregory Huey[16], David J. Tanner[16], Thomas F. Hanisco[17], and Glenn M. Wolfe[17,18]

[1]Department of Chemistry & Biochemistry, University of Colorado, Boulder, CO, USA
[2]Cooperative Institute for Research in Environmental Sciences (CIRES), Boulder, CO, USA
[3]Department of Chemistry, University of Michigan, Ann Arbor, MI, USA
[4]Department of Atmospheric & Oceanic Science, University of Maryland, College Park, MD, USA
[5]Department of Chemistry & Biochemistry, University of Maryland, College Park, MD, USA
[6]Earth System Science Interdisciplinary Center, University of Maryland, College Park, MD, USA
[7]Department of Atmospheric Chemistry and Climate, Institute of Physical Chemistry Rocasolano, Spanish National Research Council (CSIC), Madrid, Spain
[8]Argentine National Research Council (CONICET), FCEN-UNCuyo, UNT-FRM, Mendoza, Argentina
[9]Wolfson Atmospheric Chemistry Laboratories (WACL), Department of Chemistry, University of York, York, UK
[10]John A. Paulson School of Engineering and Applied Sciences, Harvard University, Cambridge, MA, USA
[11]Department of Earth and Planetary Sciences, Harvard University, Cambridge, MA, USA
[12]Department of Chemistry, Copenhagen University, Copenhagen, Denmark
[13]National Center for Atmospheric Research (NCAR), Boulder, CO, USA
[14]Department of Atmospheric Science, Rosenstiel School of Marine & Atmospheric Sciences (RSMAS), University of Miami, Miami, FL, USA
[15]Department of Chemistry, University of California, Irvine, CA, USA
[16]School of Earth & Atmospheric Sciences, Georgia Tech, Atlanta, Georgia, USA
[17]Atmospheric Chemistry and Dynamics Laboratory, NASA Goddard Space Flight Center, Greenbelt, MD, USA
[18]Joint Center for Earth Systems Technology, University of Maryland, Baltimore County, Baltimore, MD, USA
[a]now at: Chemical Sciences Division, National Oceanic and Atmospheric Administration (NOAA), Boulder, CO, USA
[b]now at: National Center for Atmospheric Research (NCAR), Boulder, CO, USA
[c]now at: Department of Chemistry, University of Drexel, Philadelphia, PA, USA
[d]now at: Department of Chemical Engineering, Carnegie Mellon University (CMU), Pittsburgh, PA, USA

Correspondence: Rainer Volkamer (rainer.volkamer@colorado.edu)

Received: 28 June 2017 – Discussion started: 7 July 2017
Revised: 5 December 2017 – Accepted: 7 December 2017 – Published: 22 December 2017

Published by Copernicus Publications on behalf of the European Geosciences Union.

Abstract. We report measurements of bromine monoxide (BrO) and use an observationally constrained chemical box model to infer total gas-phase inorganic bromine (Br_y) over the tropical western Pacific Ocean (tWPO) during the CONTRAST field campaign (January–February 2014). The observed BrO and inferred Br_y profiles peak in the marine boundary layer (MBL), suggesting the need for a bromine source from sea-salt aerosol (SSA), in addition to organic bromine (CBr_y). Both profiles are found to be C-shaped with local maxima in the upper free troposphere (FT). The median tropospheric BrO vertical column density (VCD) was measured as 1.6×10^{13} molec cm^{-2}, compared to model predictions of 0.9×10^{13} molec cm^{-2} in GEOS-Chem (CBr_y but no SSA source), 0.4×10^{13} molec cm^{-2} in CAM-Chem (CBr_y and SSA), and 2.1×10^{13} molec cm^{-2} in GEOS-Chem (CBr_y and SSA). Neither global model fully captures the C-shape of the Br_y profile. A local Br_y maximum of 3.6 ppt (2.9–4.4 ppt; 95 % confidence interval, CI) is inferred between 9.5 and 13.5 km in air masses influenced by recent convective outflow. Unlike BrO, which increases from the convective tropical tropopause layer (TTL) to the aged TTL, gas-phase Br_y decreases from the convective TTL to the aged TTL. Analysis of gas-phase Br_y against multiple tracers (CFC-11, H_2O / O_3 ratio, and potential temperature) reveals a Br_y minimum of 2.7 ppt (2.3–3.1 ppt; 95 % CI) in the aged TTL, which agrees closely with a stratospheric injection of 2.6 ± 0.6 ppt of inorganic Br_y (estimated from CFC-11 correlations), and is remarkably insensitive to assumptions about heterogeneous chemistry. Br_y increases to 6.3 ppt (5.6–7.0 ppt; 95 % CI) in the stratospheric "middleworld" and 6.9 ppt (6.5–7.3 ppt; 95 % CI) in the stratospheric "overworld". The local Br_y minimum in the aged TTL is qualitatively (but not quantitatively) captured by CAM-Chem, and suggests a more complex partitioning of gas-phase and aerosol Br_y species than previously recognized. Our data provide corroborating evidence that inorganic bromine sources (e.g., SSA-derived gas-phase Br_y) are needed to explain the gas-phase Br_y budget in the upper free troposphere and TTL. They are also consistent with observations of significant bromide in Upper Troposphere–Lower Stratosphere aerosols. The total Br_y budget in the TTL is currently not closed, because of the lack of concurrent quantitative measurements of gas-phase Br_y species (i.e., BrO, HOBr, HBr, etc.) and aerosol bromide. Such simultaneous measurements are needed to (1) quantify SSA-derived Br_y in the upper FT, (2) test Br_y partitioning, and possibly explain the gas-phase Br_y minimum in the aged TTL, (3) constrain heterogeneous reaction rates of bromine, and (4) account for all of the sources of Br_y to the lower stratosphere.

1 Introduction

Gas-phase Bromine in the atmosphere can be divided into organic and inorganic species. Inorganic bromine in the gas phase (Br_y) can be further divided into active bromine ($BrO_x = Br + BrO$), reservoir species (HBr, HOBr, $BrNO_2$, and $BrONO_2$), and photolabile compounds (Br_2 and BrCl). Atomic bromine (Br) and bromine monoxide (BrO) rapidly interconvert, primarily by reaction with O_3 and photolysis.

Reactions of BrO_x have a number of important impacts on the troposphere. First, BrO_x participates in catalytic reaction cycles that destroy ozone (von Glasow et al., 2004; Read et al., 2008; Saiz-Lopez and von Glasow, 2012; Schmidt et al., 2016; Simpson et al., 2015; Wofsy et al., 1975). Second, BrO_x modifies NO_x ($= NO + NO_2$) by increasing the ratio of NO_2 / NO (Bloss et al., 2010), and is an overall sink of NO_x (Schmidt et al., 2016) among other chemical effects (Custard et al., 2015; Evans et al., 2003; Lary, 2005). Third, BrO_x adds to oxidative capacity and exerts a number of competing effects on HO_x ($= OH + HO_2$). In particular, the lower ozone leads to a lower production of OH radicals from ozone photolysis, lower NO_x leads to a decrease in the OH / HO_2 ratio, and HOBr photolysis increases the OH / HO_2 ratio. Fourth, BrO_x is thought to be the primary oxidant of mercury in the atmosphere (Coburn et al., 2016; Goodsite et al., 2004; Holmes et al., 2006) and an important loss mechanism for dimethyl sulfide (Boucher et al., 2003). Fifth, the net-effect of BrO_x impacts on O_3, NO_x, and HO_x leads to an increase in the lifetime of CO, hydrocarbons, and climate-active gases such as methane (Lelieveld et al., 1998; Parrella et al., 2012; Saiz-Lopez and von Glasow, 2012).

Bromine also has important impacts on the stratosphere, where the ozone destruction potential is ~ 60 times greater than that of chlorine (on a per atom basis; Sinnhuber et al., 2009). Historically, the source of stratospheric bromine has been thought to be analogous to chlorine, resulting from the source gas (SG) injection (SGI) of longer-lived organic bromine species (LLS) – of both anthropogenic and natural origin – into the stratosphere. However, measurements of stratospheric Br_y generally exceed the abundance of Br_y that can be explained from SGI of LLS alone (Carpenter et al., 2014; Salawitch et al., 2005). Very short-lived species (VSLS; e.g., bromoform, $CHBr_3$, dibromomethane, CH_2Br_2) directly add to SGI, and their photolysis and oxidation in the troposphere adds Br_y as product gas (PG) injection (PGI) into the LS (lower stratosphere; Ko et al., 2003). Recent measurements of elevated BrO in the free troposphere (FT) suggest sea-salt sources may contribute to Br_y in the FT (Volkamer et al., 2015; Wang et al., 2015; Schmidt et al., 2016), but the relative contribution of sea-salt-derived Br_y and VSLS-derived PGI contributions to stratospheric Br_y injection has not, to our knowledge, previously been experimentally evaluated. One objective of the CONvective TRansport of Active Species in the Tropics (CONTRAST) and the Airborne Tropical TRopopause EXperiment (ATTREX) field campaigns

(January and February 2014) in Guam was to provide observational constraints to Br_y from aircraft measurements of BrO in the upper troposphere–lower stratosphere (UTLS) over the tropical western Pacific Ocean (tWPO; Chen et al., 2016; Jensen et al., 2016; Pan et al., 2017; Werner et al., 2017).

Differential optical absorption spectroscopy (DOAS) measurements of BrO have been made in the tropics from satellites (Chance, 1998; Richter et al., 2002; Theys et al., 2011; Wagner et al., 2001), ground-based Multi-AXis–DOAS (MAX-DOAS; Theys et al., 2007), balloon profiles (Dorf et al., 2006, 2008; Pundt et al., 2002), and airborne platforms (Volkamer et al., 2015; Wang et al., 2015; Werner et al., 2017). In addition to DOAS, microwave radiometry has also been employed to measure BrO (Millán et al., 2012; Stachnik et al., 2013). Chemical ionization mass spectrometry (CIMS) measurements of atmospheric Br_y, using I^- or SF_6^-, have largely been limited to BrO, although BrCl, HOBr, and Br_2 have also been detected (Le Breton et al., 2017; Chen et al., 2016; Neuman et al., 2010).

Here we describe measurements of BrO by the University of Colorado airborne MAX-DOAS instrument aboard the NCAR/NSF Gulfstream V (GV) aircraft during the CONTRAST field campaign (January and February 2014) in Guam. The GV carried a suite of in situ and remote-sensing instruments designed to characterize atmospheric composition targeting bromine species, including bromocarbons and inorganic bromine species as well as dynamical properties. An overview of the campaign is available in Pan et al. (2017). The campaign consisted of 17 research flights (RFs). Numerous flights were in or near clouds and thus presented challenges for DOAS retrievals. We focus the analysis on portions of five flights shown in Fig. 1: RF03, RF04, RF06, RF07, and RF15, which were conducted in largely cloud-free air. RF03, RF04, and RF07 were chosen for vertical profiles over the tWPO, covering altitudes from the boundary layer up to the lower tropical tropopause layer (TTL) on 19, 21, and 27 January 2014. The flight paths of RF06 and RF15 were to the north of Guam and targeted the Northern Hemisphere extratropical jet stream on 25 January and 25 February 2014, respectively. For RF15, the GV crossed the jet stream and sampled the Northern Hemisphere LS.

The measurements and models are presented in Sect. 2. Section 3 describes the DOAS measurements aboard the GV, as well as measurements used to constrain a chemical box model to infer total gas-phase inorganic bromine (Br_y); this includes sensitivity studies and a discussion of different chemical regimes for heterogeneous chemistry that recycles Br_y. Section 4 discusses the results by comparing with two global models (GEOS-Chem and CAM-Chem), and places them in context with the existing literature. The atmospheric implications of tropospheric halogens for atmospheric composition and our understanding of bromine sources are summarized and discussed. Section 5 presents the conclusions and provides an outlook.

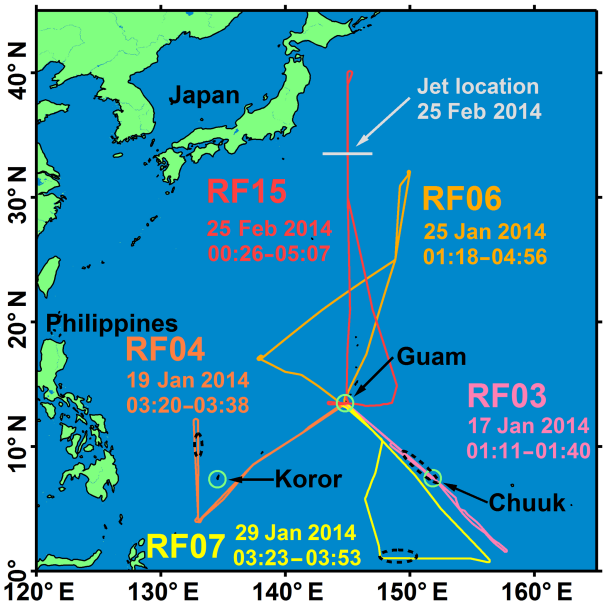

Figure 1. Flight tracks with the locations of profile case studies (0–15 km) used in this work. For northbound flights, RF06 and RF15, the times reflect periods used for detailed modeling. For RF03, RF04, and RF07, the locations of the vertical profiles are indicated by the black dashed ellipses, and the times listed are those of the profiles, and low-level flight legs in the boundary layer.

2 Experimental

The University of Colorado Airborne Multi-AXis Differential Optical Absorption Spectroscopy (CU AMAX-DOAS) instrument aboard the GV measured trace gases including the halogen oxides BrO and IO, as well as NO_2. Additional species such as formaldehyde (HCHO), O_3, H_2O, and glyoxal (CHOCHO) can also be retrieved. Other instruments and measurements aboard the GV included but were not limited to the following: the Advanced Whole Air Sampler (AWAS), which measured species including halocarbons and a variety of chemical tracers; the HIAPER Atmospheric Radiation Package (HARP), which measured actinic flux and photochemical rates; a trace organic gas analyzer (TOGA), which measured organic species including halocarbons and aldehydes; chemiluminescent measurements of NO, NO_2, and O_3; the Picarro CRDS instruments, which measured CO_2 and CH_4; a vacuum ultra violet (VUV) fluorescence instrument (Aerolaser), which measured CO; the In Situ Airborne Formaldehyde (ISAF) instrument, which measured HCHO; and an ultra-high sensitivity aerosol spectrometer (UHSAS), which measured size-resolved Aitken and accumulation mode aerosol. The measurements used in this work are summarized in Table 1.

Table 1. Instruments aboard the NSF GV research aircraft used to constrain the box model.

Instrument	Parameters used in this work	Time resolution
AMAX-DOAS	BrO, NO_2	30 s
AWAS	Ethane, Propane, Isobutane, n-Butane, CFC-11, Benzene	minutes*
Chemiluminescence	NO, NO_2, O_3	1 s
HARP	Actinic flux (upward and downward) is used to calculate photolysis rates	1 s
ISAF	HCHO	1 s
PICARRO	Methane	1 s
TOGA	Propane, Isobutane, n-Butane, HCHO, CFC-11, Benzene	2.8 min
UHSAS	Aitken and accumulation mode aerosol surface area	1 s
Aerolaser VUV fluorescence	CO	2 s
GV	Pressure, temperature, water, location	1 s

* AWAS samples were collected at intervals determined in flight by an operator.

2.1 The CU AMAX-DOAS instrument

The CU AMAX-DOAS instrument has been deployed during field campaigns in urban air (Baidar et al., 2013; Oetjen et al., 2013), and over remote oceans (Dix et al., 2013; Volkamer et al., 2015), and is described in detail in these papers. Briefly, the CU AMAX-DOAS consists of a wing-mounted pylon containing a motion-stabilized telescope and two spectrographs housed in the interior of the aircraft. Scattered sunlight enters the telescope along a well-defined field of view (vertical dispersion of 0.17°) and is actively motion-stabilized with a pointing accuracy better than 0.2° in real time (Baidar et al., 2013; Volkamer et al., 2015). Elevation angles (EAs) above geopotential horizontal are positive, those below are negative, and zero EA points forward of the aircraft. Viewing windows provide an unobstructed view to shallow angles (−30 to +30°) as well as zenith and nadir geometries. Light entering the telescope travels through fiber optic bundles to two spectrograph-detector units, each consisting of an Acton SP2150 spectrograph coupled to a PIXIS400B CCD. The units are operated synchronously, integrating spectra every 30 s. One Acton SP2150/PIXIS400B CCD unit (AP1) covers the spectral range from 330 to 470 nm with 0.7 nm full width half maximum (FWHM) optical resolution. The other (AP2) measures 440–700 nm at 1.2 nm FWHM resolution. Spectra collected on AP1 are used for the measurement of BrO, glyoxal, HCHO, H_2O, IO, NO_2 (360 and 450 nm), and O_4 (360 nm); spectra on AP2 are used for the measurement of NO_2 (560 nm), and O_4 (477 nm). In this work only BrO, NO_2 (360 nm), and O_4 (360 nm) results will be presented, using EA 0° spectra collected with 30 s integration times. Zenith spectra with at least 2 min integration times collected at low altitude under relatively clear skies were used as reference spectra, with the nearest qualifying spectrum in time being used. In all instances, the reference was from the same RF. The specific settings used are discussed in Sect. 2.1.1.

Differential slant column densities (dSCDs) of BrO are the primary data product from the AMAX-DOAS. O_4 dSCDs are used to constrain atmospheric radiative transfer in one of two ways: optimal estimation to obtain explicit aerosol extinction profiles, or parameterization using a ratio of measured O_4 dSCDs with those modeled in a Rayleigh atmosphere. Combination of this radiative information with the BrO dSCDs is used to obtain BrO mixing ratios as vertically resolved profiles (Volkamer et al., 2015) through optimal estimation and along the flight track by a parameterization method (Dix et al., 2016). These processes are outlined in greater detail in Sect. 2.1.2.

When using parameterization data in the box model, we account for the fact that the AMAX-DOAS instrument detects photons scattered at a variety of distances along the line of sight. The median photon is scattered 5–70 km forward of the plane, depending on altitude and aerosol conditions. This difference between air masses sampled by AMAX-DOAS and the in situ observations was accounted for as follows: when the aircraft maintains its heading, AMAX-DOAS data are taken to correspond to the air mass where the median photon was scattered, which is then sampled by in situ instruments with some delay (typically 4.5–6.0 min). The atmosphere used for radiative transfer modeling accounts for this delay using model information from the same location. When the aircraft changes heading, the AMAX-DOAS data are matched to the in situ data nearest in altitude and latitude.

2.1.1 DOAS retrieval

Trace gases were fitted using the DOAS method (Platt and Stutz, 2008) using the QDOAS software package (Danckaert et al., 2012). The wavelength calibration for each spectrum is precisely determined by measuring the mercury atomic emission at 404.7 nm. This slit function was further refined by fitting two wavelength-dependent degrees of freedom, using the Kurucz spectrum as reference (Chance and Kurucz, 2010; Kurucz et al., 1984). The slit function was fixed for final calibration of the instrument wavelength mapping. High-resolution laboratory cross sections (species and references given in Table 2) are convolved with the instrument

Table 2. DOAS fitting windows used in fitting BrO, O_4, and NO_2 in QDOAS software.

Cross section	Wavelength window		
	BrO 335–359 nm[h]	O_4 350–387.5 nm[i]	NO_2 356–380 nm[j]
BrO[a]	×	×	×
HCHO[b]	×	×	×
NO_2 [c]	×	×	×
O_4 [d]	×	×	×
O_3 [e]	×	×	×
$O_3 \times \lambda$ [e]	×	×	×
Ring[f]	×	×	×
Ring $\times \lambda$ [f, g]	×	×	×

[a] Wilmouth et al. (1999) at 228 K.
[b] Meller and Moortgat (2000) at 298 K.
[c] Vandaele et al. (1998) at 220 K.
[d] Thalman and Volkamer (2013) at 296 K. The O_4 in the BrO window was not fitted, but rather constrained to the value obtained in the O_4 optimized fit and scaled to the wavelength of the O_4 peak at 350 nm.
[e] Serdyuchenko et al. (2014) at 223 and 243 K, the wavelength scaled O_3 uses the 223 K cross section. This and the 243 K cross section are orthogonalized to the 223 K cross section.
[f] Ring was calculated using the QDOAS (Danckaert et al., 2012) tool using the reference spectrum for wavelength calibration.
[g] This matches the treatment in Langford et al. (2007).
[h] The BrO window used a polynomial of order 6 and a linear offset correction. O_3 and NO_2 were orthogonalized to the first 3 terms of the polynomial.
[i] The O_4 window used a polynomial of order 5 and a linear offset correction. O_3 and NO_2 were orthogonalized to the first 3 terms of the polynomial.
[j] The NO_2 window used a polynomial of order 5 and a linear offset correction.

function for analysis. Broadband extinction including Mie and Rayleigh scattering is accounted for by a polynomial. Trace gases with broad-band absorption components such as O_3 and NO_2 are orthogonalized to this polynomial. A linear intensity offset is included in some settings to account for instrumental stray light and imperfect knowledge of the Ring effect (Grainger and Ring, 1962). Absorption by relevant species is fitted simultaneously using the non-linear Marquardt–Levenberg algorithm with full non-linear treatment reserved for shift, stretch, and intensity offset (Danckaert et al., 2012). This is done in finite wavelength windows targeting specific trace gases. The analysis settings for BrO, NO_2, and O_4 (360 nm) are summarized in Table 2.

BrO was analyzed using a four-band analysis in the window 335–359 nm. The broader window was chosen to maximize information on other absorbers. The overlapping O_4 was accounted for by first determining accurate O_4 dSCDs using an optimized fit window, and prescribing these O_4 dSCDs in the BrO fit. Information on O_4 in the BrO fitting window is maximized at wavelengths of greatest differential absorption by this dimer, namely at the peak at 343 nm and the shoulder at the window edge at 359 nm. The O_4 cross section has been scaled to reflect the shorter path length of photons through the atmosphere at the lower wavelengths, using a λ^{-4} dependence, which is based on the assumption that Rayleigh scattering dominates. The mixing ratio of NO_2 was retrieved for the RF15 case study and was used to constrain the box model (Supplement and Fig. S1).

2.1.2 Radiative transfer modeling

Simulations were run using the Monte Carlo radiative transfer model McArtim (Deutschmann et al., 2011) in a 1-D spherical atmosphere. Aerosol extinction is accounted for by taking advantage of the fact that the atmospheric profile of $[O_4]$ is highly predictable, namely it scales as the square of the $[O_2]$, which has an essentially constant mixing ratio at altitudes of interest and scales linearly as a function of density (Spinei et al., 2015; Thalman and Volkamer, 2013). Comparison of modeled and measured O_4 SCDs (slant column densities) is done in one of two ways: parameterization (Dix et al., 2016) of aerosol effects using a ratio, or retrieval of explicit aerosol profiles (Baidar et al., 2013; Volkamer et al., 2015). The high accuracy of the Rayleigh scattering cross sections represented in the radiative transfer model and O_4 dSCD measurements used by the parameterization method has been independently evaluated by laboratory measurements (Thalman et al., 2014), and field observations in the absence of (Spinei et al., 2015) and in the presence of aerosols (Volkamer et al., 2015).

The parameterization method is discussed in detail in Dix et al. (2016). Briefly, the method makes use of the fact that spectra recorded with EA 0° are strongly sensitive to the atmospheric layer at instrument altitude. Recorded EA 0° spectra are analyzed using reference spectra that largely cancel out column contributions from above and below the instrument. The conversion of dSCDs into VMRs (volume mixing ratios) is realized by calculating box air mass factors for a Rayleigh atmosphere and applying a scaling factor constrained by O_4 dSCDs to account for aerosol extinction. The color ratio of the measured intensities at 477 and 640 nm is used to identify and filter measurements affected by clouds. Cloud filtering is manually quality controlled using aircraft video data and adapted where needed. An iterative VMR retrieval scheme corrects for trace gas profile shape effects. Profile information is gained from DOAS measurements during ascents and descents, and interpolated above the aircraft based on CAM-Chem profiles. For stratospheric absorbers like BrO and NO_2, a stratospheric correction is included. The magnitude of the stratospheric correction is characterized by periodically upward looking EA 10° spectra and interpolated between successive EA 10° measurements, assuming profile shapes from CAM-Chem. During portions of RF15, the telescope pointing exhibited a small positive bias of less than 1°. This effect was well characterized at all times, and has been accounted for in the analysis. To account for horizontal concentration gradients, especially near the jet, photons are modeled in a horizontally homogenous atmosphere constructed using measurements and models for the zonal location of the median photon scattering. Errors are the total of the following three components added in quadrature: (1) a parameterization error of 30 % but no better than 0.5 ppt, (2) the standard error of the mean of the component 30 s dSCDs, (3) the

quadratic mean of the proportional dSCD errors of the component 30 s dSCDs.

For the optimal estimation method, aerosol profiles are retrieved by seeking to reproduce the measured O_4 SCDs. O_4 SCDs are primarily sensitive to aerosol extinction over other aerosol radiative properties, which are set to values expected to be typical of the local atmosphere. Settings are summarized in Table S1 in the Supplement. Where O_4 dSCDs are lower than modeled, aerosol extinction is increased to achieve better agreement (Volkamer et al., 2015). An onion peeling approach is used to retrieve an initial aerosol profile, which is adjusted by hand until modeled and measured O_4 SCDs converge (Baidar et al., 2013). Extinction profiles retrieved at 200 m vertical resolution at 360 nm are presented in Fig. S2a1–a3. Total aerosol optical depth was 0.304 in RF03, 0.272 in RF04, and 0.231 in RF07. Agreement between measured and modeled O_4 is better than 2×10^{42} molec^2 cm^{-5} (8×10^{-4} optical density) and often better than 1×10^{42} molec^2 cm^{-5} (4×10^{-4} optical density) as shown in Fig. S2b1–b3. An Ångström exponent (α) of 1 is assumed in adjusting the aerosol extinction from the 360 nm derived using O_4 to 350 nm relevant for BrO. Air mass factors for each measurement were modeled at 500 m resolution, the grid resolution used for BrO profile retrieval. The a priori profile was a constant mixing ratio of 0.05 ppt BrO (though retrievals were all found to be insensitive to the choice of the a priori profile). The a priori error was set to be 2000 % for RF03 and 10 000 % for RF04 and RF07. The lower error for RF03 was chosen to increase the stability of the profile retrieval from 0.5 to 2.0 km, because the presence of a small cloud interfered with some spectra that have been excluded from the inversion. dSCD errors are propagated into the diagonal terms of the error covariance matrix. The error covariance matrix was constructed with an effective height of 0.5 km, resulting in nearest-neighbor off-diagonal terms. The resulting averaging kernels for the inversion are shown in Fig. S2d1–d2. For RF04 and RF07 they typically peak sharply near 1, indicating independent information for all layers. The effects of lower a priori error and removal of data collected in the presence of clouds are apparent in the averaging kernel profile for RF03, which has a gap near the surface. The mean averaging kernel peak values are 0.728, 0.953, and 0.962 for RF03, RF04, and RF07, respectively. The total degrees of freedom are 18.2, 17.2, and 26.9 for RF03, RF04, and RF07 profiles, respectively.

2.2 Other measurements

A number of other instruments were aboard the NCAR GV during the CONTRAST field campaign (Pan et al., 2017). Data used to constrain the box model are summarized in Table 1. More detailed descriptions of the instruments can be found in the Supplement.

2.3 Model descriptions

Data from the AMAX-DOAS and other instruments were combined and used to initialize a box model (Wang et al., 2015) in order to examine partitioning of inorganic bromine (Br_y), specifically the ratio BrO / Br_y, and infer gas-phase Br_y from the BrO measurements. In addition, BrO, Br_y, and Br_y speciation were also obtained from two chemical transport models: the Goddard Earth Observing System with Chemistry model (GEOS-Chem; Schmidt et al., 2016; Sherwen et al., 2016) and the Community Atmospheric Model with Chemistry model (CAM-Chem; Fernandez et al., 2014) for purposes of comparison.

2.3.1 Box model

The box model has been previously described in Wang et al. (2015). The model calculates gas-phase Br_y partitioning, and is constrained to measurements of chemical species and meteorological parameters as summarized in Table 1 and Sect. 2.2. The model was initialized every 5 min along the flight track. In general, data collected at a time resolution of $\sim$ 30 s or at higher frequency were averaged into 5 min bins, and used as inputs to the box model; lower frequency data were linearly interpolated. For profile case studies, horizontal homogeneity was assumed and in situ and remote-sensing data were matched by altitude. For horizontal case studies, the AMAX-DOAS data were matched with in situ data sampled from the location of the median photon, as elaborated below. The primary box-model output is the ratio BrO / Br_y computed with 30 % error (Dix et al., 2013; Wang et al., 2015). This is added in quadrature with the BrO errors outlined above in Sect. 2.1.2 when computing the error in Br_y. Sensitivity studies were conducted to bound the impacts of uncertainties in chemical kinetics and available surface area; these are described further below.

Box model sensitivity studies

The four box-model cases (0–3) are summarized in Table 3. Cases 0–2 use different constraints for the amount of aerosol surface area available for heterogeneous chemical reactions, and case 3 adjusts the gas-phase kinetics of bromine reactions.

The base case (case 0) used JPL (Jet Propulsion Laboratory) kinetics and UHSAS measured surface area. Size-specific particle concentrations for particles between 84 nm and 1 µm were measured by the UHSAS and were used to compute a surface area, assuming spherical particles. This is taken to be the minimum aerosol surface area available, because a previous optical closure study using AMAX-DOAS and High Spectral Resolution Lidar (HSRL; Volkamer et al., 2015) found that the airborne UHSAS may underestimate particle size by about a factor of 2 for reasons that are currently not well understood. Examination of CONTRAST

data confirms that this is again the case (Supplement and Fig. S3)

The first chemical sensitivity study (case 1) is identical to case 0, but used the measured UHSAS surface area multiplied by 4, based on results of these optical closure studies. The rationale for case 1 is that heterogeneous and multiphase chemistry (uniformly represented using heterogeneous kinetics in the box model) can be determinative to the gas-phase lifetime of Br_y reservoir species (i.e., HBr, and to a lesser extent also HOBr and $BrONO_2$). The fact that measured surface area is a lower limit has implications for heterogeneous reaction rates, bromine recycling, and the BrO / Br_y ratio, and case 1 provides the best estimate of the available aerosol surface area.

The second sensitivity study (case 2) explores the possible effect of ice particles on bromine partitioning. Even very low ice concentrations add significant surface area that has the potential to rapidly impact local chemistry. CDP (cloud droplet probe) and 2D-C (two-dimensional cloud probe) measure super-micron-sized particles, cloud droplets, and ice. Sparse ice particles present a sampling challenge, and measurements were used as qualitative indicators for the presence of ice. 2D-C sometimes detected the presence of ice under conditions when ice should have sublimed, which may be due to rapid gravitational settling of ice particles. There might be insufficient time for the gas-phase Br_y partitioning to equilibrate to the surface area of such ice particles, and as a result case 2 likely indicates a lower limit of gas-phase Br_y. Case 2 used an ice climatology constructed from GEOS-5 data (Molod et al., 2015) whenever 2D-C indicated the presence of ice. An additional sensitivity study (not shown) explored the potentially large surface area contribution from super-micron particles (not measured by UHSAS) that are visible in the CDP data at lower altitudes and found no significant difference from case 1.

Finally, the third sensitivity study (case 3) used the Br_y kinetics suggestion of Kreycy et al. (2013) to represent the conversion of BrO and $BrONO_2$. This is mediated by the reaction $BrO + NO_2$ and the photolysis of $BrONO_2$. Kreycy et al. (2013) investigated BrO, O_3, and NO_2 concentrations in the polar stratosphere at sunset and found the measured variations with respect to solar zenith angle deviated from theory based on JPL kinetics (Sander et al., 2011). Their recommended modifications of $k_{BrO+NO_2,\,Kreycy} = 0.75 \times k_{BrO+NO_2,\,JPL}$ and $J_{BrONO_2,\,Kreycy} = 1.27 \times J_{BrONO_2,\,JPL}$ are used only for our case 3. These changes are relevant only in stratospheric air, where $BrONO_2$ is a significant daytime reservoir species.

Box model heterogeneous chemical regimes

The following heterogeneous chemical regimes (HCRs) are distinguished to evaluate partitioning among Br_y and BrO_x species:

HCR1 – low surface area density (SA): $SA < 2 \times 10^{-3}\,cm^2\,m^{-3}$. Partitioning among BrO_x and the reservoirs is well approximated as three independent (gas-phase) equilibria of BrO_x with the Br_y reservoir species HOBr, HBr, and $BrONO_2$. HBr is typically the major Br_y species, and the BrO_x / Br_y ratio is low (0.20–0.40). This regime is most relevant in the upper FT and convective TTL (all box-model cases). These regions are further characterized by low O_3 and high J_{BrO} (photolysis rate of BrO) and as a result Br atoms make up near-half or the majority of BrO_x. The BrO / Br_y ratio is typically less than 0.15, and Br_y estimates are moderately sensitive to the available SA.

HCR2 – moderate SA: $2 \times 10^{-3} < SA < 1 \times 10^{-2}\,cm^2\,m^{-3}$. Heterogeneous reactions have the potential to shift the HBr / BrO_x equilibrium dramatically. HBr does not readily photolyse, and reacts slowly with OH radicals to form BrO_x in the gas phase. As a result, heterogeneous reactions are the dominant loss process for HBr. Further, HOBr and O_3 can facilitate the heterogeneous conversion of condensed-phase bromide back into the gas phase. In this regime HBr / Br_y is strongly sensitive to the available SA as well as the rates of heterogeneous reactions. The BrO_x / Br_y ratio can increase rapidly from 0.20 to 0.70 (depending strongly on SA; see Sect. 3.3 and Fig. S4). The upper limit of BrO_x / Br_y is sensitive to both $[H_2O]$ vapor and $[O_3]$, which control the concentration of HO_x. The abundance of HO_x is important due to the reactions $BrO + HO_2 \rightarrow HOBr + O_2$, and to a lesser extent $Br + OH \rightarrow HOBr$ and $Br + HO_2 \rightarrow HBr + O_2$. HCR2, which is relevant in the mid- and upper FT and convective TTL (base case) and the upper FT and the convective TTL (case 1). The SA that accompanies the presence of ice (case 2) is such that HCR2 is eliminated. The BrO / Br_y ratio is strongly correlated with SA, changing by up to a factor of 4 between cases 0 and 1. O_3 and H_2O concentrations and changes to J_{BrO} over this regime in the FT and TTL modulate BrO / Br_y between 0.14 and 0.40 (see Fig. 5).

HCR3 – high SA: $SA > 1 \times 10^{-2}\,cm^2\,m^{-3}$. Heterogeneous reactions have the potential to eliminate HBr as a meaningful gas-phase Br_y reservoir. HOBr is the main Br_y reservoir species. In the HCR3 regime, BrO_x / Br_y is insensitive to SA, as gas-phase reactions become limiting, and typically varies between 0.20 and 0.50. Further increasing SA, such as by including super-micron particles measured by the CDP, does not modify the chemistry. This regime is relevant from the surface to the lower FT and in the aged TTL/stratosphere (case 0), surface to mid-FT and aged TTL/stratosphere (case 1), and in the entire model atmosphere (case 2). In the troposphere, BrO / Br_y increases with altitude (from 0.15–0.25 near the surface to 0.45–0.50 in the mid-FT), due to decreasing humidity and O_3 concentration ($molec\,cm^{-3}$), as well as the increasing value of J_{HOBr} with altitude. In the aged TTL, low humidity, low oxygenated volatile organic compounds (OVOCs), and high O_3 give rise to $BrO / Br_y > 0.35$. In the stratosphere, $BrONO_2$ becomes a

Table 3. Box model sensitivity studies probing the effects of aerosol surface area, ice, and kinetics for $BrONO_2$.

Box model case	Surface areas	Kinetics
Case 0	UHSAS measured surface area	JPL (Sander et al., 2011)
Case 1	UHSAS measured surface area $\times 4$*	JPL idem
Case 2	UHSAS measured surface area $\times 4$ and GEOS-Chem ice climatology	JPL idem
Case 3	UHSAS measured surface area $\times 4$ and GEOS-Chem ice climatology	Kreycy et al. (2013)

* Based on results of optical closure study in Sect. 3.1 and Fig. 3 of Volkamer et al. (2015).

significant Br_y reservoir species, and caps the BrO / Br_y ratio near 0.50.

2.3.2 CAM-Chem

The 3-D chemistry climate model Community Atmospheric Model with Chemistry (CAM-Chem) is described in Lamarque et al. (2012). CAM-Chem includes all of the physical parameterizations of CAM4 (Neale et al., 2013) and a finite volume dynamical core (Lin, 2004) for the tracer advection. In the present configuration, meteorological analysis (from GEOS-5) specific to the observational periods are used to constrain the meteorological fields (horizontal wind components and temperature) in CAM-Chem. The horizontal resolution is $0.9° \times 1.25°$ and the vertical resolution of 52 levels includes full coverage of the troposphere and stratosphere, with a full representation of tropospheric and stratospheric chemistry. The VSLS version used here includes geographically distributed and time-dependent oceanic emissions of six bromocarbons ($CHBr_3$, CH_2Br_2, CH_2BrCl, $CHBrCl_2$, $CHBr_2Cl$, CH_2IBr) as well as an additional source of inorganic bromine and chlorine in the lower troposphere due to sea-salt aerosol (SSA) dehalogenation (Fernandez et al., 2014; Ordóñez et al., 2012; Saiz-Lopez et al., 2012). In particular, it considers heterogeneous processes for halogen species on a variety of surfaces including uptake and recycling of HBr, HOBr, and $BrONO_2$ on ice crystals and sulfate aerosols. The importance of these reactions, as well as the contribution from each independent VSLS and sea-salt source to the halogen burden of SG and PG species in the TTL, are discussed in Fernandez et al. (2014). CAM-Chem output was used to examine how well modeled coupled chemistry and dynamics captured the BrO observations of the AMAX-DOAS and Br_y inferred by the box model.

2.3.3 GEOS-Chem

GEOS-Chem (Bey et al., 2001) is a global 3-D model of atmospheric composition driven by assimilated meteorological observations from the NASA Global Modeling and Assimilation Office (GMAO). GEOS-Chem is driven by GEOS-FP meteorological data. In this study, GEOS-Chem was used to simulate the coupled effect of bromine chemistry with other physical and chemical processes, and to test how well it captures BrO measured by AMAX-DOAS and Br_y inferred by the box model. Stratospheric concentrations (monthly and diurnally varying) of Br_y are taken from a GEOS-CCM (chemistry climate model) simulation (Liang et al., 2010). Halogen chemistry in the model from Parrella et al. (2012) as referenced in Wang et al. (2015) has been updated (Schmidt et al., 2016; Sherwen et al., 2016, 2017a) and now includes more extensive heterogeneous chemistry including reactions on ice crystals and cross-halogen coupling. These changes have led to a reduction in modeled HBr / Br_y as well as Br_y washout, leading to an increase in BrO_x / Br_y (Schmidt et al., 2016).

3 Results and atmospheric modeling context

3.1 Bromine vertical profiles

The locations of the vertical profiles are shown in Fig. 1 with details as follows: (1) descent from RF03 on 17 January 2014 starting at 01:11 UTC at 9.0° N, 150.1° E at 12.2 km heading southeast, and ending at 01:40 UTC at 7.4° N, 151.8° E at 300 m over the Chuuk atoll; (2) ascent from RF04 on 19 January 2014 heading due north at 133.0° E starting at 03:20 UTC at 9.2° N at 400 m and ending at 03:38 UTC at 12.2° N at 13.2 km; and (3) ascent from RF07 on 29 January, heading due west at 1.1° N starting at 03:23 UTC at 150.5° E at 500 m, and ending at 03:53 UTC at 147.6° E at 13.8 km. These profiles represent conditions that are well suited to profile retrievals (solar zenith angle $< 70°$, mostly cloud free) and contain at least two measurements in each 500 m altitude bin.

Measured BrO profiles are shown in Fig. 2a, e, and i, and they exhibit significant variability. BrO concentrations in the lowest 500 m were 1.0 ± 0.5 ppt (RF03; Fig. 2a), 1.7 ± 1.2 ppt (RF04; Fig. 2e), and < 0.5 ppt (RF07, below detection limit; Fig. 2i). The uncertainty reflects the overall retrieval error here. The BrO variability was further characterized during level flight at low altitude following the RF03 descent over Chuuk and prior to the RF04 ascent. Mean mixing ratios retrieved from these data varied between 0.9 and 1.6 ppt BrO (RF03) and 1.6–4.4 ppt BrO (RF04). The higher value is not the result of a single outlier but rather represents the maximum of several minutes of data acquisition, for which retrieved BrO is greater than 3.5 ppt. These results suggest that BrO heterogeneity in the lowest 500 m is likely significant

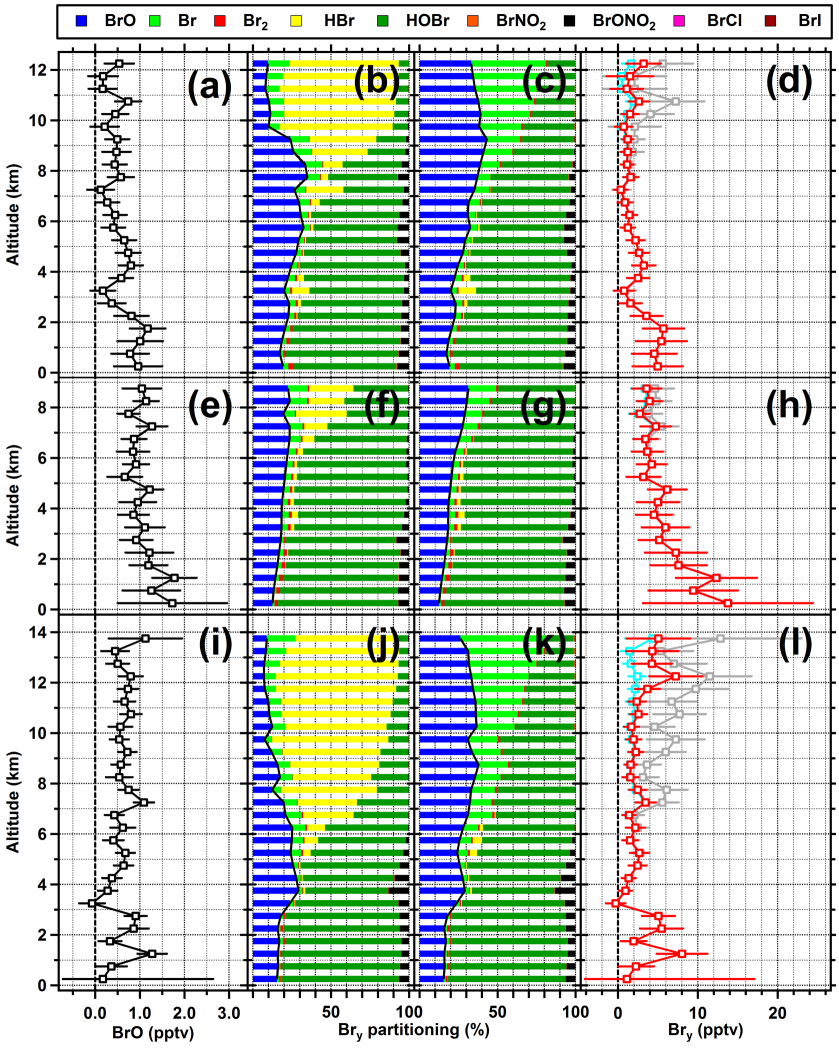

Figure 2. BrO, Br_y, and Br_y partitioning for RF03 **(a–d)**, RF04 **(e–h)**, RF07 **(i–l)**. BrO mixing ratios were obtained by optimal estimation. Partitioning of Br_y species: **(b, f, j)** case 0; **(c, g, k)** case 2; (black line) BrO / Br_y ratio. **(d, h, l)** Br_y from case 0 (grey); case 1 (red); case 2 (cyan).

on both local and regional scales. At these altitudes, AMAX-DOAS spectra average over path lengths of 5 km horizontally, which eases the comparison with model predictions on regional scales.

There is significant BrO variability also in the transition layer (TL: 0.5–2 km), where BrO mixing ratios are elevated relative to the lower FT. The mean mixing ratios below 2 km are 0.9 ± 0.4 ppt (RF03), 1.3 ± 0.6 ppt (RF04), and 0.7 ± 0.7 ppt (RF07). Unless otherwise noted, error bars reflect the variance in atmospheric variability, and retrieval errors with statistical leverage added in quadrature. The profiles also show variable structure through the lower and middle FT (2.0–9.5 km), with mean BrO mixing ratios of 0.5 ± 0.3 ppt (RF03), 1.0 ± 0.3 ppt (RF04), and 0.5 ± 0.2 ppt (RF07). In the upper FT and lowermost TTL (tropospheric air > 9.5 km), the mean BrO mixing ratios are 0.4 ± 0.2 ppt (RF03) and 0.6 ± 0.2 ppt (RF07).

The distribution of Br_y species was modeled for each altitude grid point separately for the three profiles. Figure 2 show results for cases 0 and 2. The additional error from modeling is not immediately apparent in Fig. 2d, h, and l because the 30 % error contribution (Sect 2.3.1) is relatively small compared to the error in the BrO measurements (mean proportional error of 54 %). Here we present results for case 0, leaving the other cases for the sensitivity study presented in Sect. 3.3. The profiles contain significant structure in aerosol SA, humidity, and O_3, which can be characterized in the context of the HCR1-3 regimes outlined in Sect. 2.3.1. HCR1 applies at altitudes above 7–10 km, while HCR3 dominates in the lower troposphere. The chemistry transitions from HCR3 to HCR2, and from HCR2 to HCR1, occur at 8.0 and

10.0 km (RF03), 6.0 and 7.0 km (RF04), and 5.5 and 9.0 km (RF07), respectively. The mean ratio BrO / Br_y from the surface through the mid-FT (< 9.5 km) is 0.24 ± 0.05 (RF03), 0.18 ± 0.03 (RF04), and 0.21 ± 0.05 (RF07). The inferred Br_y in the MBL and TL (< 2.0 km) is 4 ± 2 ppt (RF03), 9 ± 3 ppt (RF04), and 4 ± 3 ppt (RF07). All three flights have Br_y minima in the lower to mid-FT (2.0–9.5 km), for which the mean Br_y is 2 ± 1 ppt (RF03), 4 ± 1 ppt (RF04), and 2 ± 1 ppt (RF07).

In the lower troposphere, bromine chemistry resides in the HCR3 regime. There is significant variability in the BrO / Br_y ratio, which can be explained by the factors most important to HCR3 partitioning: humidity and O_3. Average water vapor mixing ratios below 6.5 km are 1.08 % (RF03), 1.28 % (RF04), and 0.97 % (RF07) and the mean O_3 is 30 ppb (RF03), 25 ppb (RF04), and 33 ppb (RF07). The higher humidity favors HOBr over BrO_x in RF04 compared to RF03 and RF07. Lower O_3 in RF04, particularly in two filaments with O_3 below 20 ppb between 1–2 and 3–4 km, further compounds the difference with the other two flights and drives BrO / Br_y to even lower values.

In the mid-FT, bromine chemistry resides in the HCR2 regime. The decreasing SA with altitude allows HBr to be an increasingly important reservoir (i.e., heterogenous processing of HBr becomes slow) and drives down the computed value of BrO / Br_y. In parallel, the trends in HCR3 chemistry from below continue in the mid-FT; i.e., BrO_x is increasingly favored over HOBr as $[H_2O]$ decreases and J_{HOBr} increases, and the Br / BrO ratio shifts toward Br as low temperatures and low $[O_3]$ slow $Br + O_3 \rightarrow BrO + O_2$, and J_{BrO} increases with altitude. Overall, BrO / Br_y remains roughly constant at 0.30 ± 0.07 (RF03), 0.23 ± 0.02 (RF04), and 0.17 ± 0.03 (RF07). The mean surface area in RF03 is ~ 3 times that in RF04, and RF07, driving the higher average value of the BrO / Br_y ratio. The variability in BrO / Br_y in RF03 and RF07 is also driven by greater variability in SA, which is relatively constant at these altitudes in RF04.

HCR1 applies in the upper FT and TTL, where HBr is the primary reservoir species of Br_y. The BrO_x / Br_y ratio is low, almost constant in the box model at these altitudes, with values of 0.10 ± 0.01 (RF03) and 0.09 ± 0.02 (RF07). The BrO_x–reservoir equilibria are relatively stable; changes in the BrO / Br_y ratio result from displacements of the Br / BrO partitioning. Observed mixing ratios of O_3 are low – decreasing from 26 ppb at 9 km to 18 ppb at 12.5 km in RF03, and varying between 23 and 24 ppb over the same altitudes in RF07, before dropping to 18 ppb at 14 km. Temperature decreases from 248 K at 9 km to 223 K at 12.5 km in RF03 and from 250 to 222 K over the same altitudes in RF07 then further to 213 K at 14 km. Measured J_{BrO} continues to increase with altitude. In the upper FT, the Br / BrO ratio is ~ 1, while in the TTL BrO is reduced to as little as 28 % of BrO_x, yet BrO remains well above the DOAS detection limit. Note that BrO is flat or only mildly increasing in the upper FT and TTL. However, the decrease in BrO / Br_y drives an increase in Br_y from 2.1 ppt at 9 km to 5.6 ppt at 12.5 km, with a maximum of 7.2 ppt Br_y at 11 km (RF03), and 3.6 ppt at 9 km to 12.8 ppt at 14 km (RF07).

3.2 TTL and LS

The BrO mixing ratios during flight track legs flown at a level altitude were retrieved using the parameterization technique outlined in Dix et al. (2016), as described in Sect. 2.1.2. Figures 3 and S5 show a number of tracers used to define the TTL and LS during RF06 and RF15. These are simplified into four regimes with simple, single-variable definitions that allow separation for ease of examination. The LS is defined as air above 12.5 km and $O_3 > 200$ ppb, and the TTL is above 12.5 km and $O_3 < 200$ ppb.

As can be seen in Fig. 3, the LS defined in this way is poleward of the jet stream and is characterized by consistently low H_2O and CO, and high O_3 varying between 200 and 900 ppb. The transition from the TTL to the LS is marked by greatest O_3, above the levels found elsewhere in the stratosphere. CFC-11, not shown in Fig. 3, is below 230 ppt in the stratosphere. The LS is further divided into the middleworld LS and overworld LS. The division from Hoskins (1991) of 380 K potential temperature (θ) is slightly modified to 377 K to obtain two contiguous regions (Fig. 3a). The transition from the middleworld to the overworld is also marked by high O_3, much like the LS entrance and exit.

The TTL is divided into the convective TTL defined as air masses with $H_2O / O_3 > 0.1\,\mathrm{ppm\,ppb^{-1}}$ and the aged TTL where $H_2O / O_3 < 0.1\,\mathrm{ppm\,ppb^{-1}}$. Observations from the profiling case studies are all in the convective TTL by these criteria. This is to be expected, given that the profiles are in the western Pacific warm pool, where convection to 15 km and above is persistent. The GV can only probe the TTL closer to the tropopause through latitudinal transects where the relevant region is at lower altitude. Figure S6 compares this classification to tracer–tracer classifications of the TTL from other works. The left panel uses the definition from Pan et al. (2014) as proxy for the TTL: $[H_2O] > [H_2O]_{\mathrm{stratospheric}}$, and $[O_3] > [O_3]_{\mathrm{tropospheric}}$. Using this definition, the convective TTL as defined here includes high-altitude tropospheric air and the aged TTL includes stratospheric air. The right panel correlates [CO] and $[O_3]$ examining CONTRAST RF15, as done in Chen et al. (2016). The aged TTL as defined in this work is nearly equivalent to the TTL-LMS (tropical tropopause layer–lowermost stratosphere) transition defined in Chen et al. (2016); i.e., [CO] is correlated with $[O_3]$ with a slope of -0.4. Exceptions to this are that portions of the convective TTL, and a mid-FT filament (RF07), fall on the same line (would be TTL-LMS in Chen et al., 2016), and portions of the aged TTL (RF06, RF15) organize as parallel lines with slopes of -0.03, which would classify as stratospheric in Chen et al. (2016).

As the tracer–tracer correlations make apparent, the aged TTL is characterized by O_3, H_2O, and CO changing in con-

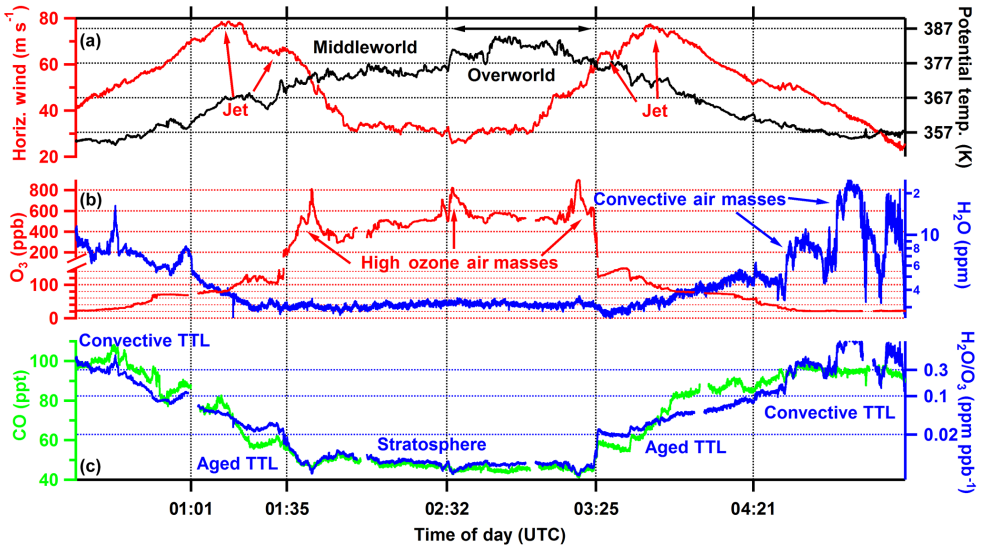

Figure 3. Meteorological and chemical tracers during RF15. **(a)** (Red) horizontal wind speed; (black) potential temperature (θ). The subtropical jet stream is visible where the horizontal wind maxima have tropospheric and stratospheric halves (indicated by arrows). The black arrow indicates the overworld (here: θ above 377 K). **(b)** (Red) O_3; (blue) H_2O. The troposphere–stratosphere transition is marked at 200 ppb O_3. Positive departures in H_2O mark convective air masses. **(c)** (Green) CO; (blue) H_2O / O_3 ratio. The 0.1 ppm ppb^{-1} line is used to separate the aged TTL from the convective TTL. The times marked indicate the transitions (from left to right) 01:01 convective TTL to aged TTL, 01:35 aged TTL to middleworld LS, 02:32 middleworld LS to overworld LS, 03:25 overworld LS to aged TTL, and 04:21 aged TTL to convective TTL.

cert. There is no consistent correlation between [O_3] and [H_2O], though both vary significantly. In contrast, there is a consistently strong inverse correlation between [O_3] and [CO]. The aged TTL is also characterized by concentrations of fine aerosol SA sufficient for HCR3 (or marginal HCR2). The aged TTL was probed during RF06 and RF15.

As the name suggests, the convective TTL is influenced by recent convection, and includes high-altitude air which is essentially tropospheric. Relative to the aged TTL, it is characterized by high H_2O and corroborated by elevated CO, low O_3, and low θ. Convective air masses are observed for sufficiently brief periods to be averaged over by AMAX observations. The convective TTL was probed briefly in RF03 and subsequently in RF06, RF07, and RF15. Figure S5 shows a region that was only observed in RF06 termed the convective TTL transition ($0.1 < H_2O / O_3 < 0.3$). Using the H_2O / O_3 criterion, this region is in the convective TTL, and tracer–tracer analysis corroborates an essentially tropospheric character. However, it shows no signs of recent convection, and concentrations of O_3, CO, and H_2O are similar to the aged TTL; hence the name TTL transition.

Bromine in the jet-crossing case studies

Comparing Figs. 4 and S7 to Fig. 2, the mean BrO 0.53 ± 0.08 ppt (RF06) and 1.01 ± 0.08 ppt (RF15) in air recently impacted by convection ($H_2O / O_3 > 0.3$ ppm ppb^{-1}) was similar to that observed at the highest altitudes in RF03 and RF07. Again, as in Fig. 2, the error from modeling is not always apparent in Figs. 4e and S7d (see Sect. 2.3.1). Chemically, Br_y partitioning was characterized as HCR1 (see Sect. 2.3.1), HBr dominated Br_y, and Br made up the majority of BrO_x. This drove BrO / Br_y down to 0.12 ± 0.01 (RF06) and 0.13 ± 0.03 (RF15) (compared to 0.10 ± 0.01 at 12.5 km in RF03 and 0.09 ± 0.02 at 14.0 km in RF07). The inferred Br_y in turn was 4.3 ± 0.5 and 7.9 ± 1.3 ppt for RF06 and RF15 in the TTL influenced by recent convection.

Portions of the convective TTL nearer to the aged TTL, including the convective TTL transition (see Sect. 3.2) in RF06, had more BrO, 0.9 ± 0.1 ppt (RF06) and 1.1 ± 0.5 ppt (RF15). This region included a rapid increase in aerosol surface area and ozone as the aircraft moved into lower stratospheric air. The increased SA lead to a transition from HCR1 to HCR2; however, the higher O_3 in the TTL gives rise to a higher BrO / Br_y compared to that of the mid- and upper FT. Overall, BrO / Br_y rose (RF06: 0.18 ± 0.05; RF15: 0.30 ± 0.12) and more than compensated for the increase in BrO, and as a result inferred Br_y stayed largely flat at 4.2 ± 0.6 ppt (RF06) and 4.4 ± 0.5 ppt (RF15).

Moving to the aged TTL in Figs. 4 and S7, BrO concentrations were elevated relative to the convective TTL (1.0 ± 0.2 ppt RF06 and 1.6 ± 0.1 ppt RF15). The greatest BrO mixing ratios in RF15 were observed nearest the stratosphere, since RF06 never reached the stratosphere this may in part explain the higher mean in RF15. Elevated O_3 caused BrO to dominate BrO_x. However, the high O_3 coupled with increased NO_2 caused $BrONO_2$ to make up to 20 % of day-

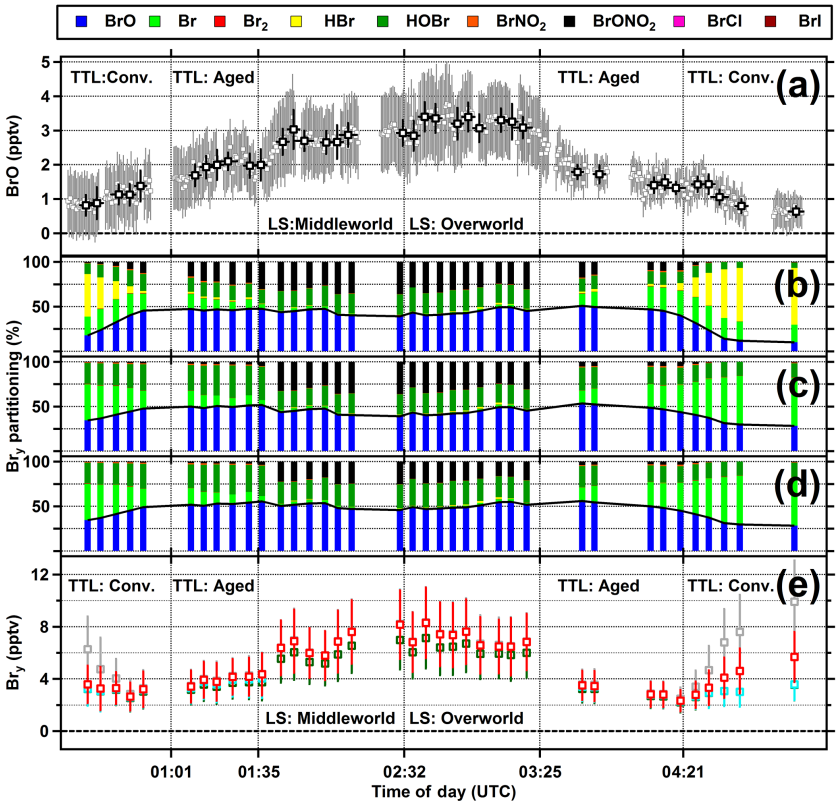

Figure 4. BrO, Br_y, and Br_y partitioning during the RF15 jet-crossing flight. **(a)** (Black) 5 min average BrO used for model input; (grey) 30 s data. **(b–d)** Partitioning of Br_y species from the box model for **(b)** case 0, **(c)** case 2, **(d)** case 3; (black line) BrO / Br_y ratio. **(e)** Br_y inferred along the flight track using the measured BrO and the modeled ratio; (grey) case 0; (red) case 1; (cyan) case 2; (dark green) case 3.

time Br_y for case 0, while $BrONO_2$ is converted to HOBr for the cases including efficient recycling. This had a limiting effect on BrO_x / Br_y as illustrated in Fig. S4. Chemical uncertainty in these air masses is driven by this increase in $BrONO_2$, see also Sect. 3.3. BrO / Br_y is high in the aged TTL (0.466 ± 0.008 in RF15), giving an inferred Br_y of 2.0 ± 0.3 ppt Br_y (RF06) and 3.49 ± 0.17 ppt (RF15). A contributing factor to this difference may again be that the highest Br_y values in RF15 are observed nearest the stratosphere, a region that RF06 did not sample.

BrO was observed to rise rapidly upon entering the stratosphere during RF15, i.e., from 1.97 ± 0.12 to 2.90 ± 0.16 ppt in the middleworld. Though the middleworld changes in BrO paralleled changes in O_3, but Br_y partitioning could not explain these changes. Instead, the BrO / Br_y ratio was rather constant at 0.44 ± 0.03. In the middleworld, O_3 and NO_2 mixing ratios were both higher than in the aged TTL, which caused $BrONO_2$ to be competitive with HOBr as a daytime reservoir species. Consequently the modeled BrO / Br_y ratio is suppressed with increasing O_3, which is consistent with Fernandez et al. (2014). Figure S4, illustrates that the magnitude of this suppression is strongest when SA is high, as is the case in the middleworld LS.

Following the climb into the overworld at the northern most point, the mean BrO slightly increased to 3.15 ± 0.13 ppt, and the largest mixing ratio of 3.35 ppt BrO (5 min average, 3.78 ppt is the 30 s maximum) was observed. Chemically, conditions were similar to the middleworld, $BrONO_2$ essentially replaced HOBr as a reservoir for Br_y, and the BrO / Br_y ratio remains flat. The small variations in BrO were mirrored by corresponding variations in BrO / Br_y leading to a consistent Br_y of 7.2 ± 0.6 ppt, without any overall trend in the overworld.

3.3 Box model sensitivity studies

The BrO-inferred Br_y estimates from the box model sensitivity studies (Table 3, Sect. 2.3.1) are summarized in Table 4. For detailed results from each model case see Table S3. Broadly, for case 0 in the lower FT (< 6.5 km), aged TTL, and stratosphere, the SA is high enough to remove HBr in the box model. As a consequence, Br_y estimates are insensitive to further increases in SA, and the BrO / Br_y ratio is solely determined by gas-phase chemistry. In contrast, between 6.5 and 13.5 km the inferred Br_y is sensitive to assumptions about the available SA and heterogeneous chemistry. The higher SA of case 1 leads to higher BrO / Br_y ratios

Table 4. Summary of BrO and Br_y mixing ratios over the tWPO.

Altitude	BrO ppt[a]	Br_y ppt[b]				
		case 0	case 1	case 2	case 3	pooled
MBL, 0–0.5 km	1.7 (1.0, 3.8)	13.8	13.8	13.8	13.8	13.8 (5.5, 30.2)
TL, 0.5–2.0 km	1.2 (0.6, 1.3)	5.8	5.8	5.8	5.8	5.8 (3.4, 8.7)
Lower FT, 2.0–6.5 km	0.7 (0.4, 0.9)	2.8	2.8	2.8	2.8	2.8 (1.6, 5.0)
Mid-FT, 6.5–9.5 km	0.6 (0.5, 1.0)	3.6	1.6	1.6	1.6	2.1 (1.3, 3.6)
Upper FT, 9.5–12.5 km	0.6 (0.3, 0.7)	6.2	2.1	1.7	1.7	2.1 (1.6, 4.4)
Convective TTL[c]	0.9 (0.5, 1.1)	4.8	3.3	2.6	2.6	3.3 (2.6, 4.3)
Aged TTL[d]	1.2 (0.9, 1.8)	2.7	2.7	2.6	2.6	2.7 (2.0, 3.5)
LS[e]	3.1 (2.8, 3.2)	6.9	6.9	6.9	6.0	6.9 (6.5, 7.4)

[a] BrO is reported as follows: median (1st quartile, 3rd quartile). [b] Br_y values are the medians for each of the chemical cases, the "pooled" values report the median (1st quartile, 3rd quartile) for cases 0, 1 and 2. Air masses above 12.5 km are classified as follows: [c] Convective TTL $H_2O / O_3 > 0.1$ ppm ppb^{-1}, [d] Aged TTL $H_2O / O_3 < 0.1$ ppm ppb^{-1}, [e] LS $O_3 > 200$ ppt.

that translate into lower estimates of Br_y (by up to a factor of 4) in the upper FT and TTL. Figure 5 illustrates the effect of adjusting the measured SA by UHSAS on BrO / Br_y (for sensitivity of BrO_x / Br_y see Fig. S4). The impact on the inferred Br_y is further apparent in Figs. 7 and S8. At 11 km, the Br_y inferred from case 1 changes from 6 ppt Br_y (case 0, grey) to 3 ppt Br_y (case 1, red). The sensitivity in the inferred Br_y is largest in air masses in the upper FT and TTL, which are in HCR1 and HCR2, and hence sensitive to aerosol SA. Assumptions about reaction probabilities on surfaces, γ, also play a role; SA and γ are indistinguishable and the product of SA $\times \gamma$ determines many heterogeneous reaction rates. The box model does not represent washout, and this too is indistinguishable from SA and γ as the total Br_y burden in the FT and above is the net result of the competition between Br_y sources, washout, and the heterogeneous reaction rates for $BrONO_2$, HBr, and HOBr.

When moving from case 0 to case 1, the altitude at which HCR3 shifts into HCR2 increases to higher altitudes, i.e., from 8.0 to 9.5 km (RF03), 6.0 to 8.0 km (RF04), and 5.5 to 9.5 km (RF07). The transition from HCR2 to HCR1 is not encountered in case 1 during RF03 and RF04, but it is observed for RF07 (the altitude of this transition shifts from typically 10.5 km, case 0, to 12.0 km, case 1). The convective TTL during both jet-crossing flights (which in case 0 is HCR1 and HCR2) shifts to HCR2 and HCR3 in case 1, with implications for the sensitivity to infer gas-phase Br_y. The remaining HCR2 air masses are those with the greatest H_2O / O_3 ratio, i.e., those that have the most convective character and are most similar to the upper FT.

In case 2, ice greatly increases SA and has the further effect of converting $BrONO_2$ to HOBr. The presence of ice shifts heterogeneous chemistry to higher SA than shown in Figs. 5 and S4, and all air moves into the HCR3 regime in the box model. Case 2 has no effect on Br_y estimates at altitudes below 6 km (no ice observed), and no significant effect in the aged TTL. A minor effect to increase the BrO / Br_y ratio is visible in the upper FT and convective TTL in Fig. S8 (cyan whiskers). Note that within case 2, BrO_x represents more than 80 % of total Br_y, a fraction that increases as ambient ozone is reduced (Fig. S4). Under these conditions, the ratio Br / BrO > 1 and atomic bromine becomes the dominant Br_y species within the convective TTL (see Figs. 2c, k

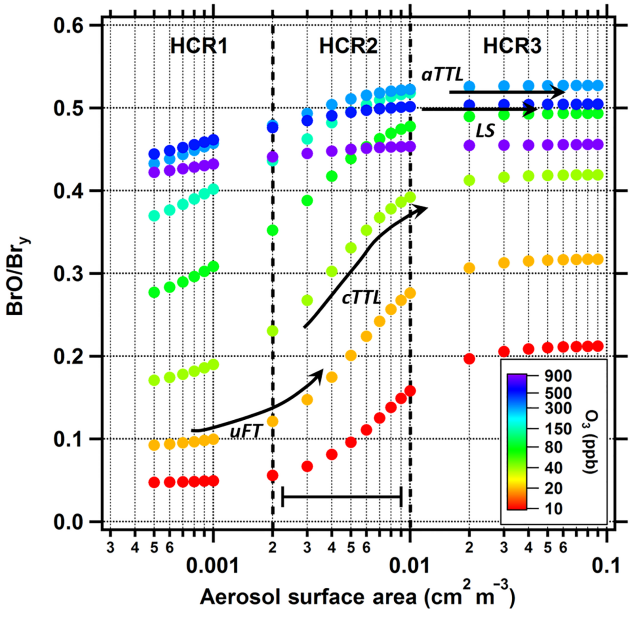

Figure 5. Sensitivity of the BrO / Br_y ratio to surface area (SA) and O_3 concentration. Conditions are representative of the upper troposphere. Dashed vertical lines mark the heterogeneous chemical regimes (HCRs; see Sect. 2.3.1). The horizontal bar at the bottom marks a factor of 4 in SA along the logarithmic abscissa (i.e., the difference between case 0 and case 1). Arrows mark the corresponding sensitivity of the BrO / Br_y ratio in the upper FT (uFT), convective TTL (cTTL), aged TTL (aTTL), and LS. The largest sensitivity is observed in the upper FT and convective TTL, while the aged TTL and LS are insensitive.

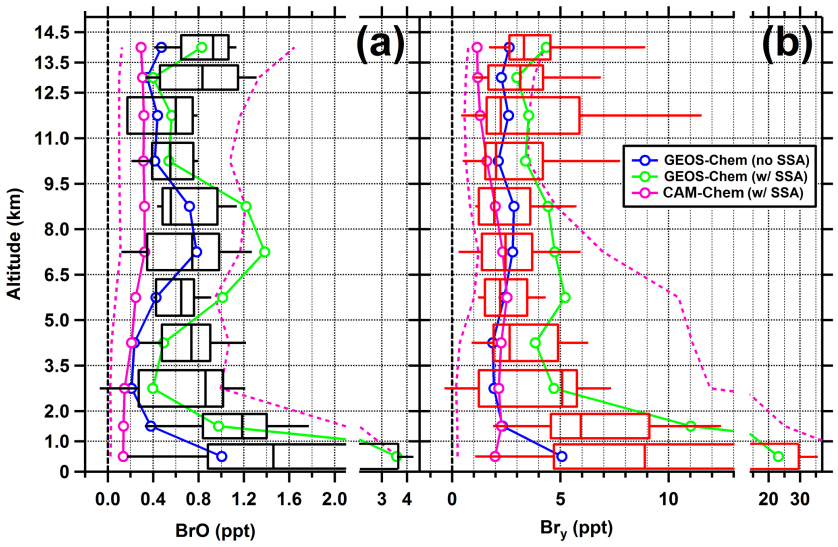

Figure 6. Tropospheric vertical profiles of BrO and Br_y over the tWPO and comparison with global models. Boxes and whiskers are for BrO observations (black) and inferred Br_y (red; box-model cases 0, 1, and 2). Boxes indicate the 25th and 75th percentile, whiskers the 5th and 95th percentile. Data points from the LS and aged TTL have been removed here to avoid bias, and emphasize tropospheric data. Lines indicate median global model profiles; the dashed magenta lines indicate the 5th and 95th percentile for CAM-Chem.

and 4c). Thus, current box-modeling results constrained with CONTRAST measurements and effective heterogeneous recycling are consistent with the proposed tropical rings of atomic halogens, where atomic bromine dominates inorganic bromine partitioning under the low ozone and ambient temperatures prevailing in the TTL (Fernandez et al., 2014; Saiz-Lopez and Fernandez, 2016).

Kreycy et al. (2013), proposed that $BrONO_2$ is relatively unstable, and recommend increasing $BrONO_2$ photolysis and decreasing $BrONO_2$ formation. Because ice similarly disrupts $BrONO_2$ both effects are included in case 3 to determine the maximum combined effect on $BrONO_2$. No discernible impact on Br_y is found for tropospheric air masses, and only a minor impact is visible in the stratosphere for the case studies of this work. The impact on Br_y partitioning in the stratosphere is visible in Fig. 4; however, the impact on BrO / Br_y can be difficult to discern. In the TTL BrO / Br_y increases by 2.9–6.5 % over case 0, and 1.5–3.1 % over case 2. The impact is greater in the aged TTL and hence greater in RF15 than RF06. The effect in the stratosphere is an increase in BrO / Br_y by 5.5–7.1 %, leading to a slight reduction in the inferred Br_y. Since BrO / Br_y is $\sim$ 50 %, the change in leverage is minimal, and the effect on inferred Br_y is not significant.

4 Discussion and atmospheric implications

4.1 Tropospheric BrO and Br_y

The overall median tropospheric BrO and Br_y profiles are shown in Fig. 6. These profiles exhibit a C-shaped profile characteristic of convective transport (Kley et al., 1996; Pan et al., 2017). To our knowledge, these are the first observations of C-shaped profiles for tropospheric inorganic bromine species (MBL into the convective TTL). The data are further summarized in Table 4. The median BrO profile decreases with altitude, from an MBL median of 1.72 ppt to a minimum around 0.5 ppt in the mid- to upper FT, and increases again in the convective TTL (see Fig. 6 and Table 4).

The trends in Br_y for the simulation case 1 (red in Fig. S8) are similar to those for BrO. Br_y decreases from a MBL median of 13.8 ppt toward a minimum of 1.6 ppt in the mid-FT where Br_y is roughly constant with altitude. Br_y begins to increase in the uppermost portion of the upper FT and reaches a local maximum in the convective TTL of 3.3 ppt. However, unlike BrO (which increases from the convective TTL to the aged TTL) gas-phase Br_y decreases from the convective TTL to the aged TTL, as is further discussed in Sect. 4.2 below (see also Fig. 7).

The box model sensitivity study medians are summarized in Table 4, and a comprehensive summary for all cases is given in Table S3. As seen in Fig. S8, a common feature to all model results is the C-shaped profile in Br_y, which is most pronounced in case 0, and least pronounced in case 2. The estimated Br_y concentration is most sensitive to chemical assumptions in the mid- and upper FT, as well as in the convective TTL, and responds sensitively to the available SA and assumptions about heterogeneous reaction rates that recycle bromine. Case 0 (grey in Fig. S8) has significantly more Br_y in all three regions, but especially in the upper FT, where the inferred Br_y is 3–5 times higher in case 0 compared to cases 1 and 2. Indications of an artificially high bias in Br_y for case 0

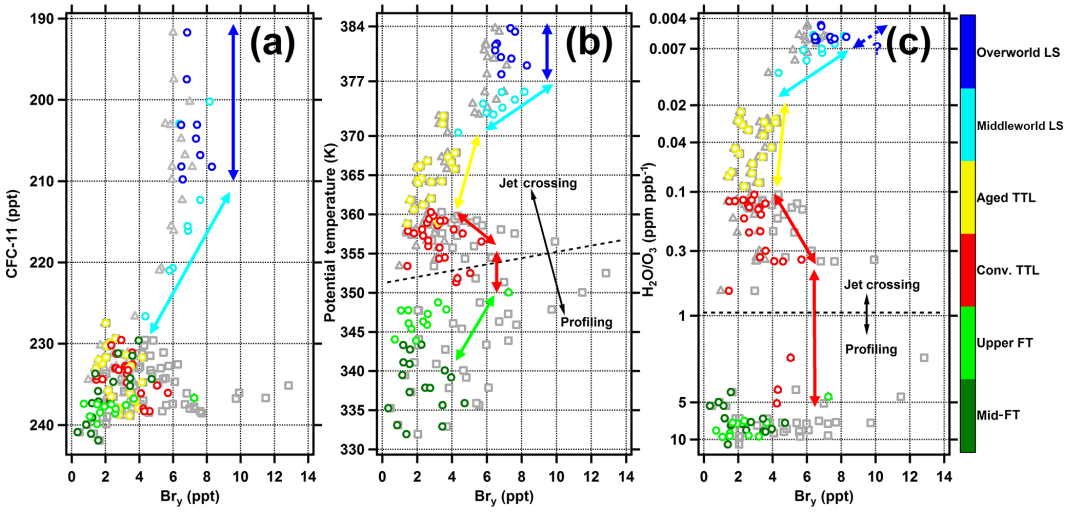

Figure 7. Br_y vertical structure in the UTLS; (colored circles) Br_y from box-model case 1; the color represents different air mass types. (grey squares) case 0; (grey triangles) case 3. Tracer correlations with **(a)** CFC-11, **(b)** potential temperature, and **(c)** H_2O / O_3 ratio have been constructed such that the top is more stratospheric, while the bottom is tropospheric. The dashed lines in **(b)** and **(c)** indicate separation between data from profiling and jet-crossing case studies – the data are inseparable in panel **(a)**.

arise from a step change in the Br_y vertical distribution between 12 and 13 km altitude (case 0). No similar step change is observed for model cases 1 and 2, which show a gradual and smooth Br_y increase from the mid-FT into the convective TTL. A previous optical closure study had revealed a low-bias in the UHSAS measured aerosol SA for reasons that are currently not well understood (Volkamer et al., 2015), which can lead to a high bias in inferred Br_y in the upper FT unless corrected (Wang et al., 2015). The step change in the Br_y profile for case 0 shown in Fig. S8, and the continuous behavior exhibited in case 1, provides corroborating evidence that SA is more accurately represented in case 1. The median Br_y from case 1 has thus been listed in Table 4. Case 2 (cyan in Fig. S8) has overall less Br_y in the mid- and upper FT, and TTL than case 1, and likely represents a lower limit for Br_y. If heterogeneous bromine recycling on the much larger ice SA is as effective as on aerosols, the potential impact of ice shifts the Br_y minimum from the mid-FT into the upper FT. The differences in Br_y from cases 1 and 2 are smaller than 0.5 ppt in the convective and aged TTL, as is indicated by the 1st quartiles in Table 4, and further discussed in Sect. 4.2.

4.2 Br_y structure in the UTLS

Figure 7 shows inferred Br_y against different tracers of the stratosphere and troposphere. Colored points show case 1, grey squares case 0, and grey triangles case 3. Figure 7a has vertically decreasing CFC-11 as an indicator of stratospheric photochemical processing, Fig. 7b, shows increasing θ indicating the stable vertical positions of different air masses locally, and Fig. 7c shows decreasing H_2O / O_3 on a logarithmic scale as an indicator of increasing stratospheric and decreasing tropospheric character. Thick dashed lines separate data from the jet-crossing and profiling case studies; trends continue smoothly across the separation. Consistently in Fig. 7, there is significant variability in the Br_y across the tropospheric–stratospheric interface. A distinct minimum in gas-phase Br_y is visible in the aged lower TTL, and Br_y increases both towards lower and higher altitudes, i.e., with decreasing CFC-11 (Fig. 7a), increasing θ (Fig. 7b), and decreasing H_2O / O_3 ratio (Fig. 7c). Figure 7a shows the correlation of Br_y against CFC-11, a tracer of photochemical age. CFC-11, similar to long-lived bromocarbons, does not photolyse significantly in the troposphere, where the mixing ratio is constant at about 237 ppt (Carpenter et al., 2014). TTL data has CFC-11 levels that are tropospheric or very near tropospheric, and the convective and aged TTL cannot be separated by CFC-11. This suggests that the aged TTL contains mostly tropospheric air, and contributions from the stratosphere are small. The photochemical liberation of Br_y from bromocarbons, including VSLS, in the aged TTL is indistinguishable from the variance in the convective inputs. CFC-11 decreases in the middleworld, consistent with the inferred Br_y increase. This matches the expected behavior as long-lived bromocarbons and possibly VSLS are photolysed along with CFC-11, liberating Br_y. However, this correlation does not extend into the overworld, where despite greater depletion of CFC-11 the Br_y expected to result from bromocarbon photolysis is not observed. Notably, gas-phase Br_y does not include aerosol bromide, which is unconstrained by CONTRAST observations. Gas-phase Br_y is not a conservative quantity, rather it is a lower limit of total bromine in the UTLS.

Taking [CFC-11] = 237 ppt as the definition of the tropopause, the gas-phase inorganic Br_y injected into the

stratosphere – the PGI – is found to be 2.6 ± 0.6 ppt Br_y for case 1. The slope of the Br_y–CFC-11 correlation fitted for all data is 0.15 ± 0.03. The middleworld points with 210 ppt < [CFC-11] < 230 ppt show the clearest correlation, with a slope of 0.22 ± 0.01. Assuming no other source or sink for Br_y, this indicates that on average CBr_y liberates Br_y at 0.15 (and up to 0.22) the rate of CFC-11 decay in the stratosphere. Modeling of sea-salt-derived Br_y in the troposphere without any contribution from organics suggests such sources are responsible for 2 ± 1 ppt Br_y in the TTL (Long et al., 2014). Additionally, previous CAM-Chem sensitivity studies determined that the contribution of sea-salt-derived bromine to the lower TTL was small (< 0.5 ppt) for the global-mean TTL (equivalent to the aged TTL here), but represented more than 3.6 pptv within strong convective regions such as the tWPO (equivalent to the convective TTL here; Fernandez et al., 2014). The difference between the regions in CAM-Chem is sensitive to the balance between recycling and washout process, which are uncertain. Thus, it is possible that the majority of the inorganic bromine in the TTL is related to sea-salt bromine sources. This is consistent with reports of underestimated Br_y in lower stratospheric air in the Southern Hemisphere subtropics that suggest an underestimation of stratospheric injection of 1.2 ppt Br_y when neglecting the sea-salt source (Wang et al., 2015).

Examining Fig. 7b, a similar story emerges. Potential temperature (θ) quite effectively separates the different air mass types (Hoskins, 1991). The LS has θ greater than 370 K, with the overworld defined here as $\theta > 377$ K. There is an inferred Br_y minimum of 2.3 ± 0.5 ppt between θ of 360 and 365 K. Then, Br_y increases with θ through the remainder of the aged TTL and the middleworld. In the overworld, Br_y is roughly constant with respect to θ, as it is versus CFC-11, and largely independent of the assumptions about the kinetics of $BrONO_2$ (compare blue and grey triangles in Fig. 7). We conclude that the Br_y minimum in the aged TTL is robust.

Figure 7c shows Br_y versus the H_2O / O_3 ratio. This panel more fully separates the aged and convective TTL and highlights the decrease in Br_y in the aged TTL. Br_y is nearly constant at 2.7 ± 0.9 ppt for values of H_2O / O_3 characteristic of the aged TTL; Br_y increases in the more humid and lower O_3 air at lower altitudes, as well as in the stratospheric middleworld. The H_2O / O_3 ratio is found to be the best tracer for the higher Br_y in the convective TTL; it also holds the most (albeit still limited) potential for capturing any trend in the overworld. While panels (a) and (b) do not reveal any trend for Br_y versus either CFC-11 or θ in the overworld, the fitted trend of Br_y versus H_2O / O_3 in panel (c) is neither different from zero nor statistically different from the trend in the middleworld.

4.3 Comparison with global models

Observed BrO and inferred Br_y in different portions of the atmosphere, as summarized in Table 4, are compared to output from GEOS-Chem and CAM-Chem global models in Fig. 6. Br_y from the experimentally constrained box-model estimates is compared with chemistry climate models, this is fundamentally a model-model comparison. However, significant information can be gleaned by leveraging the constraints on the box model and the representation of transport processes in the global models. Table 5 compares the corresponding partial and total tropospheric BrO VCDs. Examining the latter, the observations have a median value of 1.65×10^{13} molec cm^{-2}, while CAM-Chem predicts about 25 % of this value (0.41×10^{13} molec cm^{-2}). GEOS-Chem without SSA source that predicts 55 % or 0.91×10^{13} molec cm^{-2}; the closest to the observed value is GEOS-Chem with the SSA source predicts 125 % or 2.07×10^{13} molec cm^{-2}.

In the MBL, the high concentrations of BrO observed and inferred Br_y are intermediate between the GEOS-Chem simulations including and excluding the SSA Br_y source. The 95th percentile trace of CAM-Chem further illustrates that CAM-Chem captures instances where BrO is above 4 ppt near the surface, though examination of the specific case studies reveals it does not match the location of observations. GEOS-Chem roughly reproduces the near-surface vertical distribution of both BrO and Br_y with a TL partial VCD roughly twice that in the MBL (Table 5). For both BrO and Br_y when a SSA bromine source is excluded, the decrease with altitude is greater than observed, while the reverse is true when the SSA source is included; some intermediate profile seems to best reproduce the observations.

In the FT, the model simulations shown in Fig. 6 exhibit a high degree of variability. However, the variability in the observations spans a similar range. In the lower FT, the median observed BrO is between 0.6 and 0.9 ppt, and is larger than predicted by global models, which show less than 0.5 ppt between 2 and 5 km (Fig. 6a). Continuing up through the FT, the CAM-Chem median approximates the BrO and Br_y profile shapes reasonably well in the mid-FT, but follows the low end of the BrO observations, while tracking median box-modeled Br_y. As the 5th percentile and median CAM-Chem profiles in Fig. 6 help illustrate, CAM-Chem often has almost no BrO in the FT. GEOS-Chem shows significant enhancements of BrO and Br_y in the mid-FT, which are not observed. In the upper FT, consistent with the results from Wang et al. (2015), a SSA source best reproduces the median BrO observations. Furthermore, two global models with SSA source differ in their Br_y predictions in the upper FT by a factor of 3–4, bracketing the box-model-inferred Br_y. While excluding the SSA source from GEOS-Chem reproduces inferred Br_y in the mid-FT, it does not show the increase in inferred Br_y in the upper FT and convective TTL. Revisions to the ozone-induced source of HOBr from aerosol bromide at the air–water interface (Artiglia et al., 2017) – which is partic-

Table 5. Comparison of partial and total tropospheric BrO VCDs measured by AMAX-DOAS with different models. Values in parentheses indicate the 1st and 3rd quartile.

Altitude	BrO VCD $\times 10^{12}$ (AMAX-DOAS measurements)	BrO VCD (GEOS-Chem no SSA source)	BrO VCD (GEOS-Chem with SSA source)	BrO VCD (CAM-Chem)
MBL	2.1 (1.2, 4.7)	1.0 (0.2, 1.5)	3.6 (0.5, 9.0)	0.2 (0.1, 0.6)
TL	4.0 (2.8, 7.3)	2.0 (0.8, 3.3)	6.1 (3.1, 10.6)	0.4 (0.2, 1.3)
Lower FT	5.7 (2.9, 6.8)	2.1 (1.2, 4.1)	4.5 (2.4, 8.0)	1.4 (0.7, 2.2)
Mid-FT	2.2 (1.4, 3.2)	2.7 (1.7, 3.8)	4.6 (3.3, 5.9)	1.1 (0.7, 1.6)
Upper FT	1.3 (0.7, 1.7)	0.8 (0.4, 1.6)	1.2 (0.6, 2.2)	0.5 (0.3, 0.9)
TTL	1.1 (0.8, 1.5)	0.6 (0.2, 1.4)	0.7 (0.2, 1.7)	0.5 (0.3, 1.0)
Troposphere	16.5 (9.6, 25.2)	9.1 (4.5, 15.8)	20.7 (10.1, 37.4)	4.1 (2.4, 7.6)

ularly important in the tropical upper troposphere (Schmidt et al., 2016; see Sect. 4.5) – might explain the difference in behavior by global models.

In the TTL, GEOS-Chem (with and without the SSA source) shows some increase in BrO and Br_y at the highest altitudes, but only after a minimum in the same region. CAM-Chem does not show this increase in the median, though the 95th percentile makes it transparent that elevated BrO is predicted in certain instances. CAM-Chem includes an explicit representation of the stratosphere, and as a result captures more of the variability in the UTLS (not included in Fig. 5). Examination of CAM-Chem model output versus θ (Fig. S9) reveals a gas-phase Br_y minimum, albeit at lower θ (~ 350 K) and with less Br_y (1.2 ppt) than observed. As in Fig. 4, the CAM-Chem output with highest Br_y is more consistent with observations. Notably, CAM-Chem modeling of iodine chemistry (which has some similarities) has predicted a local minimum in gas-phase inorganic iodine in the TTL (Saiz-Lopez et al., 2015), consistent with observations (Volkamer et al., 2015; Dix et al., 2016).

Notably, while both BrO and Br_y are broadly consistent, partitioning of Br_y is different between the box-model and global models. The greatest difference is for HBr, where the tropospheric column abundance differs by over a factor of 15 over the total column, as shown in Table S2. Broadly, GEOS-Chem has more $BrONO_2$ and HBr, and less HOBr compared to the box model. When the SSA bromine source is excluded the BrO / Br_y ratio roughly matches as the different components cancel out (visible as the BrO and Br_y comparing similarly in Fig. 6a and b). Furthermore, O_3 is slightly higher in GEOS-Chem than observed, resulting in a greater BrO / BrO_x ratio. In CAM-Chem, however, Br_y partitioning is broadly similar to the box model, with the key exception of HBr. The larger amount of HBr in CAM-Chem is responsible for the agreement in Br_y in the FT, despite underestimating BrO observations. GEOS-Chem with a SSA source also has substantially more HBr near the surface, significantly lowering the BrO / Br_y ratio. Notably, the additional HBr in GEOS-Chem falls off more rapidly with altitude than in CAM-Chem, suggesting that transport, recycling, and/or washout are different between the global models. These differences manifest differently in the TTL, where HBr falls off more rapidly in CAM-CHEM than in GEOS-Chem. As Table S2 highlights, only in the upper FT (HCR1) is HBr in the global models consistent with that in the box model. This further reinforces the strong impact of uncertainties in HBr heterogenous chemistry when coupled to transport and washout.

4.4 Comparison with other studies

Tropospheric measurements of BrO and other Br_y species were obtained by two CIMS instruments over the tWPO during the same period as the AMAX-DOAS measurements described above. The Georgia Tech CIMS (GT CIMS) was on the same GV platform as the AMAX-DOAS and measured BrO and $Br_2 + HOBr$, with results summarized in Chen et al. (2016). There was no overlap between the tropospheric case studies presented here and those in Chen et al. (2016); the CIMS had calibration challenges for early flights, while cloudy conditions precluded AMAX-DOAS retrievals for later flights. The Manchester University CIMS (MU CIMS) was aboard the British Aerospace 146 (BAe-146) aircraft as part of the Coordinated Airborne Studies in the Tropics (CAST) project (Harris et al., 2017). During CAST, the BAe-146 had a ceiling altitude of 9 km on flights between and out of Guam, Chuuk, and Palau (Koror) which are indicated in Fig. 1. The MU CIMS sampled the troposphere during CAST in broadly the same region as the tropospheric case studies presented for the AMAX-DOAS during CONTRAST. Measurements from the MU CIMS cover BrO, Br_2, BrCl, and HOBr, all reported separately (Le Breton et al., 2017).

A comparison of tropospheric data from the AMAX-DOAS and the two CIMS instruments is presented in Fig. S10. The GT CIMS has a detection limit of ~ 1 ppt for BrO, which is substantially higher than that of MU CIMS and AMAX-DOAS. The BrO measured by MU CIMS and AMAX-DOAS is below the GT CIMS detection limit of greater than 75–90 % of the time for altitudes between 2 and 12.5 km. There are no GT CIMS measurements below 1 km, where AMAX-DOAS shows significant variability for BrO. While AMAX-DOAS mostly samples clear-sky con-

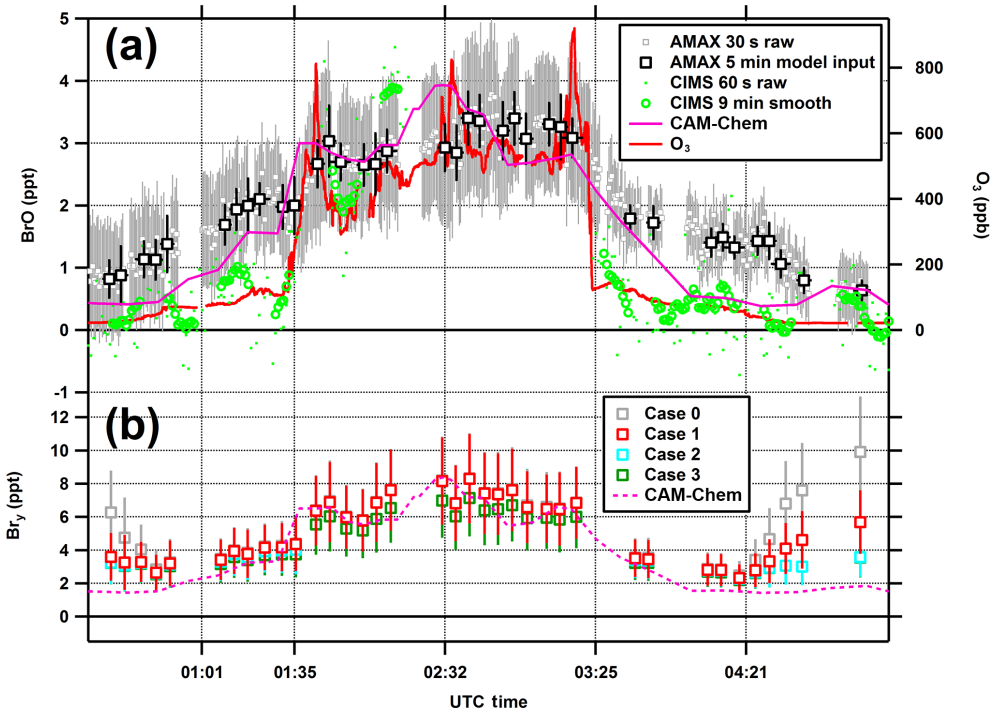

Figure 8. Comparison of BrO and Br_y along the RF15 flight track with CAM-Chem. **(a)** Raw output is shown for DOAS (grey) and GT CIMS BrO (green); along with the 5 min averages for DOAS (black squares), and a moving 9 min box average for GT CIMS (green circles); (blue line) CAM-Chem predicted BrO; (red line) measured O_3 to indicate the entrance of the LS; GT CIMS data are screened for $O_3 > 480$ ppb. **(b)** Comparison of box-model Br_y with CAM-Chem.

ditions, the GT CIMS was operating mostly during cloudy flights near convection. Such conditions favor the uptake of bromine into the condensed phase, and as a result the differences in the BrO measurements between these two instruments may in part reflect true differences in the sampled atmospheric conditions. Below 3.5 km AMAX-DOAS observes more BrO than the MU CIMS (Fig. S10a), though there is overlap in the distribution of observations. The MU CIMS does observe instances where BrO is high near the surface (Le Breton et al., 2017) corroborating the variability observed by the AMAX-DOAS. The AMAX-DOAS and MU CIMS data generally agree for BrO in the altitude range from 3.5 to 9.0 km (Fig. S10a). The measured Br_y from MU CIMS (i.e., $BrO + 2\times Br_2 + HOBr + BrCl$) is in rather good agreement with Br_y inferred from AMAX-DOAS over the 3.5 to 9.0 km altitude range, providing support for the overall veracity of our study (Fig. S10b). There are no MU CIMS measurements above 9 km. In the TTL, the differences between the GT CIMS and AMAX-DOAS are not readily resolved. These discrepancies are unlikely explained by atmospheric variability as is discussed below.

Both the AMAX-DOAS and GT CIMS operated concurrently aboard the GV during the RF15 case study, where elevated BrO was expected due to sampling of the overworld. CAM-Chem suggests that there should be 1–2 ppt BrO just prior to entering the LS (01:15 UTC of Fig. 8), which is in excellent agreement with between 1.3 and 2.1 ppt BrO observed by AMAX-DOAS in the aged TTL. By comparison, the GT CIMS observes no significant BrO in the aged TTL. Notably, the lack of change in BrO is consistent with a Br_y minimum; BrO would be expected to increase significantly by 25–150 % for constant Br_y given the change in physical and chemical conditions (see Fig. 5). Just prior to the entry into the stratosphere, GT CIMS reported 0.48 ± 0.58 ppt BrO, which is below the GT CIMS level of detection (0.6–1.6 ppt during RF15 for BrO; Chen et al., 2016), and significantly lower than both AMAX-DOAS and CAM-Chem. In the LS, GT CIMS BrO rapidly increases to ~ 3.8 ppt BrO (averaged for 02:09–02:14 UTC). The AMAX-DOAS measurements also rise, but more modestly to 2.9 ppt during the same period. The discrepancies cannot be readily explained by horizontal inhomogeneity, the air probed by the AMAX-DOAS has near-complete turnover within 12 min along the straight-line flight path. Notably, the GT CIMS does not report data when $[O_3]$ exceeds 480 ppb, owing to unrealistically high BrO that was measured, but is not trusted under such conditions. This data filter precludes a comparison of measurements in the remainder of the stratosphere.

First, tropospheric BrO profiles had recently been measured from aircraft over the tEPO during the TORERO field campaign (Volkamer et al., 2015). Tropospheric BrO VCDs from five case studies in pristine marine air showed sig-

nificant variability (0.5–3.0 $\times 10^{13}$ molec cm^{-2}; Volkamer et al., 2015; Wang et al., 2015). Dix et al. (2016) examined the TORERO BrO data set more fully, and found a campaign median tropospheric BrO VCD of 1.8 $\times 10^{13}$ molec cm^{-2} (this median excludes measurements below detection limit, and thus may be an upper limit). This is similar to the tropospheric BrO VCD of 1.6 $\times 10^{13}$ molec cm^{-2} measured over the tWPO in this study. However, there are important differences in the tropospheric BrO profile shape between the tEPO and tWPO. While we find 37 % of the BrO below 2 km over the tWPO, no significant BrO had been observed in the MBL and TL over the tEPO during TORERO, where essentially all (> 95 %) BrO was located above 2 km in the FT (Dix et al., 2016; Volkamer et al., 2015; Wang et al., 2015). Decreasing BrO with altitude had previously been observed during the TORERO RF04 case study (Wang et al., 2015). The overall TORERO data set supports observations of decreasing BrO in the lower TTL. The campaign mean BrO was 1.86 ± 0.16 ppt (95 % CI, $N = 162$) at 13.5 km, and decreased to 1.38±0.16 ppt BrO (95 % CI, $N = 78$) at 14.5 km. This is consistent with 0.9 to 1.2 ppt BrO in the TTL measured here. As noted in Dix et al. (2016), this decreasing BrO with altitude is highly significant during TORERO, and not inconsistent with results by Werner et al. (2017) as discussed below.

DOAS observations of BrO have also been reported from the Global Hawk platform at high altitudes (14–18 km) over the tWPO and tEPO (Stutz et al., 2017; Werner et al., 2017). The retrieved composite profile has BrO increase gradually from 0.7 ppt at 14.5 km to 1.1 ppt at 16.5 km, then more rapidly to 3.6 ppt at 18.5 km. The consistency between Br_y estimated from AMAX-DOAS of this work and the value of Br_y from Werner et al. (2017) is illustrated in Fig. 9. Werner et al. (2017) utilize a criterion of $CH_4 = 1790$ ppb to separate "young" air with more CH_4 and "old" air with less. Applying this same criterion to the CONTRAST DOAS data reproduces the TTL–LS separation. Utilizing the 10 K θ bins we find good agreement of Br_y in the TTL. In the LS, there is a mismatch wherein the Global Hawk and GV sampled old air at different θ. However, CH_4 concentrations span a similar range of 1690–1790 ppm indicating similar aging, and a general agreement for Br_y is also found in the LS. Notably, Werner et al. do not show a significant Br_y minimum in the TTL, probably due to the limited Global Hawk observations at $\theta < 355$ K, where such a trend is most apparent in our data. Moreover, the LS Br_y inferred in the Northern Hemisphere LS are consistent with the Br_y inferred under double tropopause conditions in the Southern Hemisphere midlatitude LS (Wang et al., 2015). Finally, CAM-Chem shows good agreement with the Br_y from the box model in this work below 340 K and above 360 K. However, between 340 and 360 K the model predicts systematically lower Br_y than inferred. Navarro et al. (2015) have shown that the CAM-Chem VSLS are consistent with CONTRAST observations. The PGI injection of VSLS, which are important for predicting Br_y profiles through the LS (Liang et al., 2010), are captured well by the model. The differences in the Br_y profile shape through the TTL are therefore unlikely to be related to VSLS alone, but most likely require additional processes.

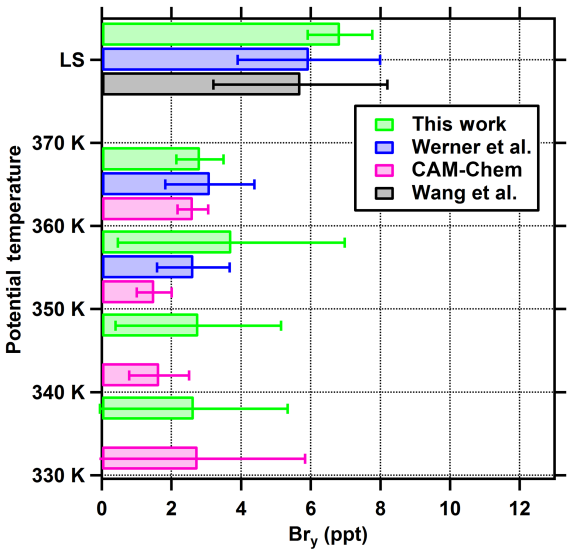

Figure 9. Br_y in the UTLS inferred from BrO observations, and comparison with CAM-Chem. Measurements probed BrO over the Southern Hemisphere eastern Pacific Ocean during TORERO (Wang et al., 2015); the Pacific Ocean during ATTREX (Werner et al., 2017), and over the Northern Hemisphere western Pacific Ocean during CONTRAST (this work). CAM-Chem results are from this work. For tropospheric air, data are presented in 10 K potential temperature (θ) bins. All stratospheric air is pooled (it was sampled at different θ, but is of comparable age; termed old in Werner et al., 2017). Bars indicate the mean Br_y in each bin, and error bars indicate the variances. For this work, cases 0–2 are pooled to calculate the means and variances.

Elevated concentrations of BrO (up to 3 ppt) in pristine air masses over the tEPO (Dix et al., 2016; Volkamer et al., 2015; Wang et al., 2015), and above Florida (Coburn et al., 2016) most likely reflect a variable influence of bromine sources from the lower atmosphere (e.g., SSA) downwind of marine convection (Long et al., 2014; Schmidt et al., 2016). Interestingly, the source region of the TORERO flights observed deep convective outflow that originated over the tWPO warm pool in the area south of the CONTRAST study area, where we observe significant BrO in the MBL consistent with SSA bromine sources. This is in contrast to low upper limits of less than 0.5 ppt MBL-BrO over the tEPO (Mahajan et al., 2012; Volkamer et al., 2015). Atmospheric models that represent sea-salt sources consistently predict several ppt BrO over tropical oceans (Long et al., 2014; Ordóñez et al., 2012; Schmidt et al., 2016; Yang et al., 2005). This conundrum is a primary reason why recent state-of-the-art models such as GEOS-Chem have decided not to represent the sea-salt source of bromine in their default configuration (Sherwen et al., 2016). The BrO profiles measured

during this study suggests that SSA is a significant source of bromine over the tWPO. The reason for the low BrO over the tEPO MBL (Volkamer et al., 2015; Wang et al., 2015) deserves further study.

4.5 Atmospheric implications

4.5.1 Relevance of halogens for atmospheric composition

Bromine is important for the oxidation of atmospheric mercury (Coburn et al., 2016; Goodsite et al., 2004; Holmes et al., 2006; Parrella et al., 2012), the destruction of ozone (von Glasow et al., 2004; Read et al., 2008; Saiz-Lopez and von Glasow, 2012; Schmidt et al., 2016; Simpson et al., 2015; Wofsy et al., 1975), and oxidative capacity. Recent first simultaneous measurements of BrO and IO over the entire height of the tropical troposphere (Volkamer et al., 2015) suggest that bromine and iodine together account regionally for 34 % of column-integrated ozone loss over the tEPO (Wang et al., 2015). Globally, the impact of bromine and other halogens reduces the ozone burden between 10 and 18 %, which is comparable to the ozone sink from the $HO_2 + O_3$ reaction (Saiz-Lopez et al., 2012, 2014; Sherwen et al., 2016, 2017b). Bromine oxidation of NO_x is an important NO_x sink, and contributes to ozone reduction by reducing the photochemical formation of ozone (Schmidt et al., 2016). Halogen chemistry is responsible for an 11 % reduction in global average OH radical concentrations (Schmidt et al., 2016), and increases the atmospheric lifetimes of methane from 7.47 to 8.28 years (Sherwen et al., 2016). However, the most recent papers (Schmidt et al., 2016; Sherwen et al., 2016) do not consider the SSA source when estimating the impacts of bromine and other halogens in the troposphere. This suggests that the above impacts may be lower estimates, as our results strongly support the need for a SSA source in the lower marine atmosphere.

Knowledge of heterogeneous/condensed-phase reactions is rapidly evolving. Recent work has found that an improved implementation of the condensed-phase reaction of HOBr with S(IV) significantly inhibits recycling of HOBr and lowers the global gas-phase Br_y burden by 50 % (Chen et al., 2017). Our models are not optimized to include these condensed-phase reactions, but including these sinks for Br_y would lower Br_y estimates from global models in Fig. 6 (and Table 5). However, recent laboratory observations of surface-active BrO_3^- (primary ozonide; Artiglia et al., 2017) also support the important role of O_3 reactive uptake for the heterogeneous recycling of gas-phase Br_y, which is most relevant in the upper troposphere (Schmidt et al., 2016). The surface activity of the primary ozonide suggests that recycling of Br_y to the gas phase may be in competition with bulk accommodation of HOBr and subsequent S(IV) chemistry, which would reduce the efficiency of Br_y washout. Furthermore, the role of organic surfactants is unclear. If organics reduce the rate of heterogeneous recycling, our Br_y estimates could be lower limits; if surfactants are neutral or accelerate heterogeneous reactions, our box-model-inferred Br_y would be rather insensitive since HBr is only a very minor reservoir species already. The impact of uncertain heterogeneous chemistry is transparent from Fig. 5 (and Fig. S4), and most relevant in the altitude range between 6.5 and 14.5 km, where Br_y inferred from BrO observations is sensitive to assumptions about heterogeneous chemistry, and estimated conservatively here. Uncertain heterogeneous chemistry is less relevant for our Br_y estimates in the aged TTL and LS (where the BrO / Br_y ratio is flat in Figs. 5 and S4). Future development of chemical transport and climate models needs to refine the representation of heterogeneous/multiphase reactions of halogens, which is currently highly simplified yet important to assess the impacts of tropospheric halogens for atmospheric composition and climate.

4.5.2 Inorganic bromine sources

The choice by recent global models (Schmidt et al., 2016; Sherwen et al., 2016) to estimate halogen impacts only based on CBr_y sources, i.e., without considering the SSA source, is justified by the ability to approximate the vertical profiles of BrO over the tEPO (Volkamer et al., 2015; Wang et al., 2015) reasonably well without a SSA source, and by the lack of any measurable BrO in the remote MBL over the tEPO (see Sect. 4.4). A key difference between profiles over the tWPO and tEPO is that significant BrO is measured in the MBL over the tWPO. This strongly supports the need for a SSA source. It also raises questions of whether models used to rationalize previous measurements accurately represent all atmospheric processes. Chiu et al. (2017) speculated that missing kinetic data to constrain $Br + OVOC$ reactions could obscure the need for a SSA source in models (Badia et al., 2017). Figure 6 illustrates that a SSA source is needed to explain inferred Br_y in the MBL, and that this source impacts atmospheric composition up to at least 3.5 km. The amount of inferred Br_y is well within the range predicted by two global models, but models that include SSA sources predict Br_y amounts that vary by a factor of 6–12 over this altitude range. In the mid-FT, the data remains inconclusive; there is no pressing need for a SSA source, but the range of inferred Br_y is not inconsistent either. Above 9.5 km the inferred Br_y increases with altitude. A Wilcoxon–Mann–Whitney rank test shows that the inferred Br_y in the upper FT and convective TTL is higher than that in the mid-FT with 98 % confidence, supporting a C-shaped profile of inferred Br_y. Models generally do not predict this increase, and profiles remain either flat or even decrease with altitude. This observation supports the speculation by Wang et al. (2015) that marine convection over the tWPO is a source of inorganic bromine. Our data provide previously missing evidence that support the widespread impact of inorganic bromine sources on the upper troposphere.

The mechanism driving the gas-phase Br_y minimum in the aged TTL is currently not well known, and could have dynamical or chemical reasons. The contribution of bromine to ozone destruction is largest in the vicinity of the tropopause (Fernandez et al., 2014; Salawitch et al., 2005; Schmidt et al., 2016; Sherwen et al., 2016), and the observed reduction in gas-phase Br_y in the aged TTL is likely to have a significant impact on ozone and OH that is relevant for the lifetime of brominated VSLS. The lifetime of VSLS in the TTL affects the ratio at which CBr_y is injected into the stratosphere as organic source gases or inorganic product gases (Gao et al., 2014; Nicely et al., 2016; Rex et al., 2014). Since the complex structure of Br_y in the TTL is only partially captured by a model like CAM-Chem, this suggests the need for further development and testing of models that dynamically couple the troposphere and the stratosphere.

5 Conclusions

We identify a gas-phase Br_y minimum in the aged TTL that is robust to assumptions regarding heterogeneous chemistry. Single-tailed Wilcoxon–Mann–Whitney rank tests (Mann and Whitney, 1947; refer to supplement for details) suggest that Br_y in the aged TTL is: (1) a local minimum ($> 95\,\%$ confidence), (2) lower than in the LS ($> 99\,\%$ confidence), and (3) lower than in the convective TTL and upper FT ($> 96\,\%$ confidence). To our knowledge, such a Br_y minimum has not previously been observed or hypothesized.

The Br_y minimum in the aged TTL is consistent with previous observations that BrO decreases from the upper FT into the lower TTL over the eastern Pacific Ocean (Dix et al., 2016), and with several recent Br_y estimates in the LS over the subtropical and tropical Pacific (Wang et al., 2015; Stutz et al., 2017; Werner et al., 2017). The 2.7 ppt (2.4–3.0 ppt; 95 % CI) gas-phase Br_y inferred in the aged TTL minimum and the tropospheric intercept of the fit of Br_y against CFC-11 (2.6 ± 0.6 ppt) constrain PGI into the stratosphere, and are in reasonable agreement with the latest World Meteorological Organization assessment of 1.1–4.3 ppt PGI (Carpenter et al., 2014).

Notably, a significant fraction of this Br_y may be SSA-derived. It is furthermore currently unknown how much Br_y is transported into the stratosphere as aerosol bromide, as all currently available quantitative assessments of Br_y in the UTLS rely on measurements of gas-phase Br_y species alone. The lack of quantitative aerosol bromine measurements leaves the total Br_y budget in the UTLS open to speculation. Indeed, aerosol measurements show a local maximum in aerosol halogen signals in the UTLS (Froyd et al., 2010; Murphy et al., 2006; Murphy and Thomson, 2000). Together with the Br_y minimum identified here, this suggests that the partitioning of bromine between the gas- and aerosol phases is significant and cannot be ignored. Whether this bromide is available for ozone destruction in the LS is currently unknown. The proportional contribution of bromine to ozone destruction is largest in the vicinity of the tropopause (Fernandez et al., 2014; Salawitch et al., 2005; Schmidt et al., 2016; Sherwen et al., 2016). A reduction in available bromine could thus have a significant impact on ozone in the TTL.

Our data provide evidence that a SSA-derived bromine source is necessary to reproduce the observed profiles of BrO and Br_y near the surface (up to 3.5 km), and provides corroborating evidence that marine convection lofts a source of inorganic bromine into the upper FT (Wang et al., 2015). Sensitivity studies indicate that the inferred Br_y is highly sensitive to assumptions about the rate of heterogeneous bromine recycling (depends on the surface area of ice/aerosols, among others) between 6.5 and 14.5 km, limiting reliable inferences of total gas-phase Br_y in the upper FT.

Notably, two global models that include a SSA bromine source predict gas-phase Br_y that differs by a factor of 6–12 in the MBL, and by a factor of 3–4 in the upper FT. The global models bracket the amount of Br_y inferred from the box model. CAM-Chem, which dynamically couples the troposphere and stratosphere, qualitatively reproduces the tropospheric BrO profile shape, but underestimates the BrO VCD; it captures a Br_y minimum in the TTL, though not quantitatively. GEOS-Chem with SSA has discrepancies in the profile shapes but best matches the measured BrO VCD. The most recent modeling estimates of the global impact of bromine (Schmidt et al., 2016; Sherwen et al., 2016) do not include a SSA source and are likely lower limits.

Models diverge as to the fraction of gas-phase Br_y that exists as HBr, especially in the lower atmosphere. Further modeling studies will be necessary to determine the magnitude of revised impacts that account for SSA-derived Br_y. Major areas for future development of chemistry climate transport models include uncertainties about the SSA source, a more detailed representation of aerosol and cloud chemistry (i.e., heterogeneous reactions, multiphase chemistry), and convective transport. Concurrent quantitative measurements of gas-phase Br_y species (BrO, HOBr, HBr, etc.) and aerosol bromide are currently missing to evaluate models. Reducing the uncertainties in impacts of halogens for atmospheric composition and climate will require comprehensive experimental field and laboratory work to close the total Br_y budget.

Data availability. The AMAX-DOAS BrO data are available from the CONTRAST data archive: http://data.eol.ucar.edu/master_list/?project=CONTRAST. The CONTRAST data set is open for use by the public, subject to the data policy: https://www.eol.ucar.edu/content/contrast-data-policy. The archive contains aircraft and atmosphere state parameters, in situ measurements, flight videos, and links to the concurrent ATTREX and CAST campaign data archives and other ancillary measurements.

The Supplement related to this article is available online at https://doi.org/10.5194/acp-17-15245-2017-supplement.

Author contributions. ELA, LLP, and RJS designed the CONTRAST research flights. SB, BD, TKK, and RV performed CU AMAX-DOAS measurements and analyzed data. DCA, ECA, ELA, NJB, JCB, TC, DC, VD, FMF, SRH, TFH, SBH, RH, GH, JBJ, RL, DDM, MAN, JMR, SMS, DJT, KU, AJW, and GMW performed measurements, and performed data analysis for other instruments on the GV. CAC, MJE, RPF, DJJ, DK, TKK, JFL, RJS, ASL, TS, JS, PAW, and SW provided model data and analysis tools. TKK and RV wrote the manuscript with contributions from all authors.

Competing interests. The authors declare that they have no conflict of interest.

Acknowledgements. We thank the CONTRAST team including pilots, technicians, forecasters, and scientists on the aircraft and on the ground particularly Pavel Romashkin and Louis L. Lussier for making the campaign a success and this work possible. Theodore K. Koenig, and Rainer Volkamer would like to thank Thomas Bannan, Michael Le Breton, and Carl J. Percival for sharing their published data from the CAST field campaign. CONTRAST was funded by the National Science Foundation (NSF). Rainer Volkamer acknowledges funding from NSF awards AGS-1261740, and AGS-1620530. The GV aircraft was operated by the National Center for Atmospheric Research's (NCAR) Earth Observing Laboratory's (EOL) Research Aviation Facility (RAF). CAST was funded by the National Environment Research Council.

Edited by: Dwayne Heard
Reviewed by: two anonymous referees

References

Artiglia, L., Edebeli, J., Orlando, F., Chen, S., Lee, M.-T., Corral Arroyo, P., Gilgen, A., Bartels-Rausch, T., Kleibert, A., Vazdar, M., Andres Carignano, M., Francisco, J. S., Shepson, P. B., Gladich, I., and Ammann, M.: A surface-stabilized ozonide triggers bromide oxidation at the aqueous solution-vapour interface, Nature Communications, 8, 700, https://doi.org/10.1038/s41467-017-00823-x, 2017.

Badia, A., Reeves, C. E., Baker, A. R., Saiz-Lopez, A., Volkamer, R., Apel, E. C., Hornbrook, R. S., Carpenter, L. J., Andrews, S. J., and von Glasow, R.: Importance of reactive halogens in the tropical marine atmosphere: A regional modelling study using WRF-Chem, Atmos. Chem. Phys. Discuss., https://doi.org/10.5194/acp-2017-903, in review, 2017.

Baidar, S., Oetjen, H., Coburn, S., Dix, B., Ortega, I., Sinreich, R., and Volkamer, R.: The CU Airborne MAX-DOAS instrument: vertical profiling of aerosol extinction and trace gases, Atmos. Meas. Tech., 6, 719–739, https://doi.org/10.5194/amt-6-719-2013, 2013.

Bey, I., Jacob, D. J., Yantosca, R. M., Logan, J. A., Field, B. D., Fiore, A. M., Li, Q., Liu, H. Y., Mickley, L. J., and Schultz, M. G.: Global modeling of tropospheric chemistry with assimilated meteorology: Model description and evaluation, J. Geophys. Res., 106, 23073–23095, https://doi.org/10.1029/2001JD000807, 2001.

Bloss, W. J., Camredon, M., Lee, J. D., Heard, D. E., Plane, J. M. C., Saiz-Lopez, A., Bauguitte, S. J.-B., Salmon, R. A., and Jones, A. E.: Coupling of HO_x, NO_x and halogen chemistry in the antarctic boundary layer, Atmos. Chem. Phys., 10, 10187–10209, https://doi.org/10.5194/acp-10-10187-2010, 2010.

Boucher, O., Moulin, C., Belviso, S., Aumont, O., Bopp, L., Cosme, E., von Kuhlmann, R., Lawrence, M. G., Pham, M., Reddy, M. S., Sciare, J., and Venkataraman, C.: DMS atmospheric concentrations and sulphate aerosol indirect radiative forcing: a sensitivity study to the DMS source representation and oxidation, Atmos. Chem. Phys., 3, 49–65, https://doi.org/10.5194/acp-3-49-2003, 2003.

Carpenter, L. J. and Reimann, S. (Lead Authors), Burkholder, J. B., Clerbaux, C., Hall, B. D., Hossaini, R., Laube, J. C., Yvon-Lewis, S. A., Blake, D. R., Dorf, M., Dutton, G. S., Fraser, P. J., Froidevaux, L., Hendrick, F., Hu, J., Jones, A., Krummel, P. B., Kuijpers, L. J. M., Kurylo, M. J., Liang, Q., Mahieu, E., Mühle, J., O'Doherty, S., Ohnishi, K., Orkin, V. L., Pfeilsticker, K., Rigby, M., Simpson, I. J., and Yokouchi, Y.: Update on Ozone-Depleting Substances (ODSs) and Other Gases of Interest to the Montreal Protocol, Chapter 1 in Scientific Assessment of Ozone Depletion: 2014, Global Ozone Research and Monitoring Project – Report No. 55, World Meteorological Organization, Geneva, Switzerland, 2014.

Chance, K.: Analysis of BrO measurements from the Global Ozone Monitoring Experiment, Geophys. Res. Lett., 25, 3335–3338, https://doi.org/10.1029/98GL52359, 1998.

Chance, K. and Kurucz, R. L.: An improved high-resolution solar reference spectrum for earth's atmosphere measurements in the ultraviolet, visible, and near infrared, J. Quant. Spectrosc. Ra., 111, 1289–1295, https://doi.org/10.1016/j.jqsrt.2010.01.036, 2010.

Chen, D., Huey, L. G., Tanner, D. J., Salawitch, R. J., Anderson, D. C., Wales, P. A., Pan, L. L., Atlas, E. L., Hornbrook, R. S., Apel, E. C., Blake, N. J., Campos, T. L., Donets, V., Flocke, F. M., Hall, S. R., Hanisco, T. F., Hills, A. J., Honomichl, S. B., Jensen, J. B., Kaser, L., Montzka, D. D., Nicely, J. M., Reeves, J. M., Riemer, D. D., Schauffler, S. M., Ullmann, K., Weinheimer, A. J., and Wolfe, G. M.: Airborne measurements of BrO and the sum of HOBr and Br_2 over the Tropical West Pacific from 1 to 15 km during the CONvective TRansport of Active Species in the Tropics (CONTRAST) experiment, J. Geophys. Res.-Atmos., 121, 12560–12578, https://doi.org/10.1002/2016JD025561, 2016.

Chen, Q., Schmidt, J. A., Shah, V., Jaeglé, L., Sherwen, T., and Alexander, B.: Sulfate production by reactive bromine: Implications for the global sulfur and reactive bromine budgets, Geophys. Res. Lett., 44, 7069–7078, https://doi.org/10.1002/2017GL073812, 2017.

Chiu, R., Tinel, L., Gonzalez, L., Ciuraru, R., Bernard, F., George, C., and Volkamer, R.: UV photochemistry of carboxylic acids at the air-sea boundary: A relevant source of glyoxal and other oxygenated VOC in the marine atmosphere, Geophys. Res. Lett., 44, 1079–1087, https://doi.org/10.1002/2016GL071240, 2017.

Coburn, S., Dix, B., Edgerton, E., Holmes, C. D., Kinnison, D., Liang, Q., ter Schure, A., Wang, S., and Volkamer, R.: Mercury oxidation from bromine chemistry in the free troposphere over the southeastern US, Atmos. Chem. Phys., 16, 3743–3760,https://doi.org/10.5194/acp-16-3743-2016, 2016.

Custard, K. D., Thompson, C. R., Pratt, K. A., Shepson, P. B., Liao, J., Huey, L. G., Orlando, J. J., Weinheimer, A. J., Apel, E., Hall, S. R., Flocke, F., Mauldin, L., Hornbrook, R. S., Pöhler, D., General, S., Zielcke, J., Simpson, W. R., Platt, U., Fried, A., Weibring, P., Sive, B. C., Ullmann, K., Cantrell, C., Knapp, D. J., and Montzka, D. D.: The NO_x dependence of bromine chemistry in the Arctic atmospheric boundary layer, Atmos. Chem. Phys., 15, 10799–10809, https://doi.org/10.5194/acp-15-10799-2015, 2015.

Danckaert, T., Fayt, C., van Roozendael, M., de Smedt, I., Letocart, V., Merlaud, A., and Pinardi, G.: QDOAS Software user manual v2.1, available at: http://uv-vis.aeronomie.be/software/QDOAS/QDOAS_manual.pdf (last access: 15 December 2017), 2012.

Deutschmann, T., Beirle, S., Frieß, U., Grzegorski, M., Kern, C., Kritten, L., Platt, U., Prados-Román, C., Puķíte, J., Wagner, T., Werner, B., and Pfeilsticker, K.: The Monte Carlo atmospheric radiative transfer model McArtim: Introduction and validation of Jacobians and 3D features, J. Quant. Spectrosc. Ra., 112, 1119–1137, https://doi.org/10.1016/j.jqsrt.2010.12.009, 2011.

Dix, B., Baidar, S., Bresch, J. F., Hall, S. R., Schmidt, K. S., Wang, S., and Volkamer, R.: Detection of iodine monoxide in the tropical free troposphere, P. Natl. Acad. Sci. USA, 110, 2035–2040, https://doi.org/10.1073/pnas.1212386110, 2013.

Dix, B., Koenig, T. K., and Volkamer, R.: Parameterization retrieval of trace gas volume mixing ratios from Airborne MAX-DOAS, Atmos. Meas. Tech., 9, 5655–5675, https://doi.org/10.5194/amt-9-5655-2016, 2016.

Dorf, M., Butler, J. H., Butz, A., Camy-Peyret, C., Chipperfield, M. P., Kritten, L., Montzka, S. A., Simmes, B., Weidner, F., and Pfeilsticker, K.: Long-term observations of stratospheric bromine reveal slow down in growth, Geophys. Res. Lett., 33, L24803, https://doi.org/10.1029/2006GL027714, 2006.

Dorf, M., Butz, A., Camy-Peyret, C., Chipperfield, M. P., Kritten, L., and Pfeilsticker, K.: Bromine in the tropical troposphere and stratosphere as derived from balloon-borne BrO observations, Atmos. Chem. Phys., 8, 7265–7271, https://doi.org/10.5194/acp-8-7265-2008, 2008.

Evans, M. J., Jacob, D. J., Atlas, E., Cantrell, C. A., Eisele, F., Flocke, F., Fried, A., Mauldin, R. L., Ridley, B. A., Wert, B., Talbot, R., Blake, D., Heikes, B., Snow, J., Walega, J., Weinheimer, A. J., and Dibb, J.: Coupled evolution of BrO_x-ClO_x-HO_x-NO_x chemistry during bromine-catalyzed ozone depletion events in the arctic boundary layer, J. Geophys. Res., 108, 8368, https://doi.org/10.1029/2002JD002732, 2003.

Fernandez, R. P., Salawitch, R. J., Kinnison, D. E., Lamarque, J.-F., and Saiz-Lopez, A.: Bromine partitioning in the tropical tropopause layer: implications for stratospheric injection, Atmos. Chem. Phys., 14, 13391–13410,https://doi.org/10.5194/acp-14-13391-2014, 2014.

Froyd, K. D., Murphy, D. M., Lawson, P., Baumgardner, D., and Herman, R. L.: Aerosols that form subvisible cirrus at the tropical tropopause, Atmos. Chem. Phys., 10, 209–218, https://doi.org/10.5194/acp-10-209-2010, 2010.

Gao, R. S., Rosenlof, K. H., Fahey, D. W., Wennberg, P. O., Hintsa, E. J., and Hanisco, T. F.: OH in the tropical upper troposphere and its relationships to solar radiation and reactive nitrogen, J. Atmos. Chem., 71, 55–64, https://doi.org/10.1007/s10874-014-9280-2, 2014.

Goodsite, M. E., Plane, J. M. C., and Skov, H.: A Theoretical Study of the Oxidation of Hg^0 to $HgBr_2$ in the Troposphere, Environ. Sci. Technol., 38, 1772–1776, https://doi.org/10.1021/ES034680S, 2004.

Grainger, J. F. and Ring, J.: Anomalous Fraunhofer Line Profiles, Nature, 193, 762–762, https://doi.org/10.1038/193762a0, 1962.

Harris, N. R. P., Carpenter, L. J., Lee, J. D., Vaughan, G., Filus, M. T., Jones, R. L., OuYang, B., Pyle, J. A., Robinson, A. D., Andrews, S. J., Lewis, A. C., Minaeian, J., Vaughan, A., Dorsey, J. R., Gallagher, M. W., Le Breton, M., Newton, R., Percival, C. J., Ricketts, H. M. A., Bauguitte, S. J.-B., Nott, G. J., Wellpott, A., Ashfold, M. J., Flemming, J., Butler, R., Palmer, P. I., Kaye, P. H., Stopford, C., Chemel, C., Boesch, H., Humpage, N., Vick, A., MacKenzie, A. R., Hyde, R., Angelov, P., Meneguz, E., and Manning, A. J.: Coordinated Airborne Studies in the Tropics (CAST), B. Am. Meteorol. Soc., 98, 145–162, https://doi.org/10.1175/BAMS-D-14-00290.1, 2017.

Holmes, C. D., Jacob, D. J., and Yang, X.: Global lifetime of elemental mercury against oxidation by atomic bromine in the free troposphere, Geophys. Res. Lett., 33, L20808, https://doi.org/10.1029/2006GL027176, 2006.

Hoskins, B. J.: Towards a PV-θ view of the general circulation, Tellus B, 43, 27–35, https://doi.org/10.3402/tellusb.v43i4.15396, 1991.

Jensen, E. J., Pfister, L., Jordan, D. E., Bui, T. V., Ueyama, R., Singh, H. B., Lawson, P., Thornberry, T., Diskin, G., McGill, M., Pittman, J., Atlas, E., and Kim, J.: The NASA Airborne Tropical TRopopause EXperiment (ATTREX):High-Altitude Aircraft Measurements in the Tropical Western Pacific, available at: https://ntrs.nasa.gov/search.jsp?R=20160004203 (last access: 15 March 2017), 2016.

Kley, D., Crutzen, P. J., Smit, H. G. J., Vömel, H., Oltmans, S. J., Grassl, H., and Ramanathan, V.: Observations of Near-Zero Ozone Concentrations Over the Convective Pacific: Effects on Air Chemistry, Science, 274, 230–233 https://doi.org/10.1126/science.274.5285.230, 1996.

Ko, M. K. W. and Poulet, G. (Lead Authors), Blake, D. R., Boucher, O., Burkholder, J. H., Chin, M., Cox, R. A., George, C., Graf, H.-F., Holton, J. R., Jacob, D. J., Law, K. S., Lawrence, M. G., Midgley, P. M., Seakins, P. W., Shallcross, D. E., Strahan, S. E., Wuebbles, D. J., and Yokouchi, Y.: Surface ultraviolet radiation: Past and future, Chapter 5 in Scientific Assessment of Ozone Depletion: 2002, Global Ozone Research and Monitoring Project – Report No. 47, World Meteorological Organization, Geneva, Switzerland, 2003.

Kreycy, S., Camy-Peyret, C., Chipperfield, M. P., Dorf, M., Feng, W., Hossaini, R., Kritten, L., Werner, B., and Pfeilsticker, K.: Atmospheric test of the $J(BrONO_2) / k_{BrO+NO_2}$ ratio: implications for total stratospheric Bry and bromine-mediated ozone loss, Atmos. Chem. Phys., 13, 6263–6274, https://doi.org/10.5194/acp-13-6263-2013, 2013.

Kurucz, R. L., Furenlid, I., Brault, J., and Testerman, L.: Solar flux atlas from 296 to 1300 nm, National Solar Observatory, 1984,

Sunspot, New Mexico, available at: http://adsabs.harvard.edu/abs/1984sfat.book.....K (last access: 4 August 2017), 1984.

Lamarque, J.-F., Emmons, L. K., Hess, P. G., Kinnison, D. E., Tilmes, S., Vitt, F., Heald, C. L., Holland, E. A., Lauritzen, P. H., Neu, J., Orlando, J. J., Rasch, P. J., and Tyndall, G. K.: CAM-chem: description and evaluation of interactive atmospheric chemistry in the Community Earth System Model, Geosci. Model Dev., 5, 369–411, https://doi.org/10.5194/gmd-5-369-2012, 2012.

Langford, A. O., Schofield, R., Daniel, J. S., Portmann, R. W., Melamed, M. L., Miller, H. L., Dutton, E. G., and Solomon, S.: On the variability of the Ring effect in the near ultraviolet: understanding the role of aerosols and multiple scattering, Atmos. Chem. Phys., 7, 575–586, https://doi.org/10.5194/acp-7-575-2007, 2007.

Lary, D. J.: Halogens and the chemistry of the free troposphere, Atmos. Chem. Phys., 5, 227–237, https://doi.org/10.5194/acp-5-227-2005, 2005.

Le Breton, M., Bannan, T. J., Shallcross, D. E., Khan, M. A., Evans, M. J., Lee, J., Lidster, R., Andrews, S., Carpenter, L. J., Schmidt, J., Jacob, D., Harris, N. R. P., Bauguitte, S., Gallagher, M., Bacak, A., Leather, K. E., and Percival, C. J.: Enhanced ozone loss by active inorganic bromine chemistry in the tropical troposphere, Atmos. Environ., 155, 21–28, https://doi.org/10.1016/j.atmosenv.2017.02.003, 2017.

Lelieveld, J., Crutzen, P. J., and Dentener, F. J.: Changing concentration, lifetime and climate forcing of atmospheric methane, Tellus B, 50, 128–150, https://doi.org/10.1034/j.1600-0889.1998.t01-1-00002.x, 1998.

Liang, Q., Stolarski, R. S., Kawa, S. R., Nielsen, J. E., Douglass, A. R., Rodriguez, J. M., Blake, D. R., Atlas, E. L., and Ott, L. E.: Finding the missing stratospheric Br_y: a global modeling study of $CHBr_3$ and CH_2Br_2, Atmos. Chem. Phys., 10, 2269–2286, https://doi.org/10.5194/acp-10-2269-2010, 2010.

Lin, S.-J.: A "Vertically Lagrangian" Finite-Volume Dynamical Core for Global Models, Mon. Weather Rev., 132, 2293–2307, https://doi.org/10.1175/1520-0493(2004)132<2293:AVLFDC>2.0.CO;2, 2004.

Long, M. S., Keene, W. C., Easter, R. C., Sander, R., Liu, X., Kerkweg, A., and Erickson, D.: Sensitivity of tropospheric chemical composition to halogen-radical chemistry using a fully coupled size-resolved multiphase chemistry-global climate system: halogen distributions, aerosol composition, and sensitivity of climate-relevant gases, Atmos. Chem. Phys., 14, 3397–3425, https://doi.org/10.5194/acp-14-3397-2014, 2014.

Mahajan, A. S., Gómez Martín, J. C., Hay, T. D., Royer, S.-J., Yvon-Lewis, S., Liu, Y., Hu, L., Prados-Roman, C., Ordóñez, C., Plane, J. M. C., and Saiz-Lopez, A.: Latitudinal distribution of reactive iodine in the Eastern Pacific and its link to open ocean sources, Atmos. Chem. Phys., 12, 11609–11617, https://doi.org/10.5194/acp-12-11609-2012, 2012.

Mann, H. B. and Whitney, D. R.: On a Test of Whether one of Two Random Variables is Stochastically Larger than the Other, Ann. Math. Stat., 18, 50–60, https://doi.org/10.1214/aoms/1177730491, 1947.

Meller, R. and Moortgat, G. K.: Temperature dependence of the absorption cross sections of formaldehyde between 223 and 323 K in the wavelength range 225–375 nm, J. Geophys. Res., 105, 7089–7101, https://doi.org/10.1029/1999JD901074, 2000.

Millán, L., Livesey, N., Read, W., Froidevaux, L., Kinnison, D., Harwood, R., MacKenzie, I. A., and Chipperfield, M. P.: New Aura Microwave Limb Sounder observations of BrO and implications for Br_y, Atmos. Meas. Tech., 5, 1741–1751, https://doi.org/10.5194/amt-5-1741-2012, 2012.

Molod, A., Takacs, L., Suarez, M., and Bacmeister, J.: Development of the GEOS-5 atmospheric general circulation model: evolution from MERRA to MERRA2, Geosci. Model Dev., 8, 1339–1356, https://doi.org/10.5194/gmd-8-1339-2015, 2015.

Murphy, D. M. and Thomson, D. S.: Halogen ions and NO+ in the mass spectra of aerosols in the upper troposphere and lower stratosphere, Geophys. Res. Lett., 27, 3217–3220, https://doi.org/10.1029/1999GL011267, 2000.

Murphy, D. M., Hudson, P. K., Thomson, D. S., Sheridan, P. J., and Wilson, J. C.: Observations of Mercury-Containing Aerosols, Environ. Sci. Technol., 40, 3163–3167, https://doi.org/10.1021/es052385x, 2006.

Navarro, M. A., Atlas, E. L., Saiz-Lopez, A., Rodriguez-Lloveras, X., Kinnison, D. E., Lamarque, J.-F., Tilmes, S., Filus, M., Harris, N. R. P., Meneguz, E., Ashfold, M. J., Manning, A. J., Cuevas, C. A., Schauffler, S. M., and Donets, V.: Airborne measurements of organic bromine compounds in the Pacific tropical tropopause layer, P. Natl. Acad. Sci. USA, 112, 13789–13793, https://doi.org/10.1073/pnas.1511463112, 2015.

Neale, R. B., Richter, J., Park, S., Lauritzen, P. H., Vavrus, S. J., Rasch, P. J., and Zhang, M.: The Mean Climate of the Community Atmosphere Model (CAM4) in Forced SST and Fully Coupled Experiments, J. Climate, 26, 5150–5168, https://doi.org/10.1175/JCLI-D-12-00236.1, 2013.

Neuman, J. A., Nowak, J. B., Huey, L. G., Burkholder, J. B., Dibb, J. E., Holloway, J. S., Liao, J., Peischl, J., Roberts, J. M., Ryerson, T. B., Scheuer, E., Stark, H., Stickel, R. E., Tanner, D. J., and Weinheimer, A.: Bromine measurements in ozone depleted air over the Arctic Ocean, Atmos. Chem. Phys., 10, 6503–6514, https://doi.org/10.5194/acp-10-6503-2010, 2010.

Nicely, J. M., Anderson, D. C., Canty, T. P., Salawitch, R. J., Wolfe, G. M., Apel, E. C., Arnold, S. R., Atlas, E. L., Blake, N. J., Bresch, J. F., Campos, T. L., Dickerson, R. R., Duncan, B., Emmons, L. K., Evans, M. J., Fernandez, R. P., Flemming, J., Hall, S. R., Hanisco, T. F., Honomichl, S. B., Hornbrook, R. S., Huijnen, V., Kaser, L., Kinnison, D. E., Lamarque, J.-F., Mao, J., Monks, S. A., Montzka, D. D., Pan, L. L., Riemer, D. D., Saiz-Lopez, A., Steenrod, S. D., Stell, M. H., Tilmes, S., Turquety, S., Ullmann, K., and Weinheimer, A. J.: An observationally constrained evaluation of the oxidative capacity in the tropical western Pacific troposphere, J. Geophys. Res.-Atmos., 121, 7461–7488, https://doi.org/10.1002/2016JD025067, 2016.

Oetjen, H., Baidar, S., Krotkov, N. A., Lamsal, L. N., Lechner, M., and Volkamer, R.: Airborne MAX-DOAS measurements over California: Testing the NASA OMI tropospheric NO_2 product, J. Geophys. Res.-Atmos., 118, 7400–7413, https://doi.org/10.1002/jgrd.50550, 2013.

Ordóñez, C., Lamarque, J.-F., Tilmes, S., Kinnison, D. E., Atlas, E. L., Blake, D. R., Sousa Santos, G., Brasseur, G., and Saiz-Lopez, A.: Bromine and iodine chemistry in a global chemistry-climate model: description and evaluation of very short-lived oceanic sources, Atmos. Chem. Phys., 12, 1423–1447, https://doi.org/10.5194/acp-12-1423-2012, 2012.

Pan, L. L., Paulik, L. C., Honomichl, S. B., Munchak, L. A., Bian, J., Selkirk, H. B., and Vömel, H.: Identification of the tropical tropopause transition layer using the ozone-water vapor relationship, J. Geophys. Res.-Atmos., 119, 3586–3599, https://doi.org/10.1002/2013JD020558, 2014.

Pan, L. L., Atlas, E. L., Salawitch, R. J., Honomichl, S. B., Bresch, J. F., Randel, W. J., Apel, E. C., Hornbrook, R. S., Weinheimer, A. J., Anderson, D. C., Andrews, S. J., Baidar, S., Beaton, S. P., Campos, T. L., Carpenter, L. J., Chen, D., Dix, B., Donets, V., Hall, S. R., Hanisco, T. F., Homeyer, C. R., Huey, L. G., Jensen, J. B., Kaser, L., Kinnison, D. E., Koenig, T. K., Lamarque, J.-F. J.-F., Liu, C., Luo, J., Luo, Z. J., Montzka, D. D., Nicely, J. M., Pierce, R. B., Riemer, D. D., Robinson, T., Romashkin, P., Saiz-Lopez, A., Schauffler, S., Shieh, O., Stell, M. H., Ullmann, K., Vaughan, G., Volkamer, R., and Wolfe, G.: The Convective Transport of Active Species in the Tropics (CONTRAST) Experiment, B. Am. Meteorol. Soc., 98, 106–128, https://doi.org/10.1175/BAMS-D-14-00272.1, 2017.

Parrella, J. P., Jacob, D. J., Liang, Q., Zhang, Y., Mickley, L. J., Miller, B., Evans, M. J., Yang, X., Pyle, J. A., Theys, N., and Van Roozendael, M.: Tropospheric bromine chemistry: implications for present and pre-industrial ozone and mercury, Atmos. Chem. Phys., 12, 6723–6740, https://doi.org/10.5194/acp-12-6723-2012, 2012.

Platt, U. and Stutz, J.: Differential Optical Absorption Spectroscopy – Principles and Applications, Springer, Heidelberg, 2008.

Pundt, I., Pommereau, J. -P., Chipperfield, M. P., van Roozendael, M., and Goutail, F.: Climatology of the stratospheric BrO vertical distribution by balloon-borne UV–visible spectrometry, J. Geophys. Res., 107, 4806, https://doi.org/10.1029/2002JD002230, 2002.

Read, K. A., Mahajan, A. S., Carpenter, L. J., Evans, M. J., Faria, B. V. E., Heard, D. E., Hopkins, J. R., Lee, J. D., Moller, S. J., Lewis, A. C., Mendes, L., McQuaid, J. B., Oetjen, H., Saiz-Lopez, A., Pilling, M. J., and Plane, J. M. C.: Extensive halogen-mediated ozone destruction over the tropical Atlantic Ocean, Nature, 453, 1232–1235, https://doi.org/10.1038/nature07035, 2008.

Rex, M., Wohltmann, I., Ridder, T., Lehmann, R., Rosenlof, K., Wennberg, P., Weisenstein, D., Notholt, J., Krüger, K., Mohr, V., and Tegtmeier, S.: A tropical West Pacific OH minimum and implications for stratospheric composition, Atmos. Chem. Phys., 14, 4827–4841, https://doi.org/10.5194/acp-14-4827-2014, 2014.

Richter, A., Wittrock, F., Ladstätter-Weißenmayer, A., and Burrows, J. P.: GOME measurements of stratospheric and tropospheric BrO, Adv. Space Res., 29, 1667–1672, https://doi.org/10.1016/S0273-1177(02)00123-0, 2002.

Saiz-Lopez, A. and Fernandez, R. P.: On the formation of tropical rings of atomic halogens: Causes and implications, Geophys. Res. Lett., 43, 2928–2935, https://doi.org/10.1002/2015GL067608, 2016.

Saiz-Lopez, A. and von Glasow, R.: Reactive halogen chemistry in the troposphere, Chem. Soc. Rev., 41, 6448–6472, https://doi.org/10.1039/c2cs35208g, 2012.

Saiz-Lopez, A., Lamarque, J.-F., Kinnison, D. E., Tilmes, S., Ordóñez, C., Orlando, J. J., Conley, A. J., Plane, J. M. C., Mahajan, A. S., Sousa Santos, G., Atlas, E. L., Blake, D. R., Sander, S. P., Schauffler, S., Thompson, A. M., and Brasseur, G.: Estimating the climate significance of halogen-driven ozone loss in the tropical marine troposphere, Atmos. Chem. Phys., 12, 3939–3949, https://doi.org/10.5194/acp-12-3939-2012, 2012.

Saiz-Lopez, A., Fernandez, R. P., Ordóñez, C., Kinnison, D. E., Gómez Martín, J. C., Lamarque, J.-F., and Tilmes, S.: Iodine chemistry in the troposphere and its effect on ozone, Atmos. Chem. Phys., 14, 13119–13143, https://doi.org/10.5194/acp-14-13119-2014, 2014.

Saiz-Lopez, A., Baidar, S., Cuevas, C. A., Koenig, T. K., Fernandez, R. P., Dix, B., Kinnison, D. E., Lamarque, J.-F., Rodriguez-Lloveras, X., Campos, T. L., and Volkamer, R.: Injection of iodine to the stratosphere, Geophys. Res. Lett., 42, 6852–6859, https://doi.org/10.1002/2015GL064796, 2015.

Salawitch, R. J., Weisenstein, D. K., Kovalenko, L. J., Sioris, C. E., Wennberg, P. O., Chance, K., Ko, M. K. W., and McLinden, C. A.: Sensitivity of ozone to bromine in the lower stratosphere, Geophys. Res. Lett., 32, L05811, https://doi.org/10.1029/2004GL021504, 2005.

Sander, S. P., Friedl, R. R., Abbatt, J. P. D., Barker, J. R., Burkholder, J. B., Golden, D. M., Kold, C. E., Kuylo, M. J., Moortgat, G. K., Wine, P. H., Huie, R. E., and Orkin, V. L.: Chemical Kinetics and Photochemical Data for Use in Atmospheric Studies, Evaluation No. 17, Pasadena, available at: http://jpldataeval.jpl.nasa.gov (last access: 25 October 2016), 2011.

Schmidt, J. A., Jacob, D. J., Horowitz, H. M., Hu, L., Sherwen, T., Evans, M. J., Liang, Q., Suleiman, R. M., Oram, D. E., Le Breton, M., Percival, C. J., Wang, S., Dix, B., and Volkamer, R.: Modeling the observed tropospheric BrO background: Importance of multiphase chemistry and implications for ozone, OH, and mercury, J. Geophys. Res.-Atmos., 121, 11819–11835, https://doi.org/10.1002/2015JD024229, 2016.

Serdyuchenko, A., Gorshelev, V., Weber, M., Chehade, W., and Burrows, J. P.: High spectral resolution ozone absorption cross-sections – Part 2: Temperature dependence, Atmos. Meas. Tech., 7, 625–636, https://doi.org/10.5194/amt-7-625-2014, 2014.

Sherwen, T., Schmidt, J. A., Evans, M. J., Carpenter, L. J., Großmann, K., Eastham, S. D., Jacob, D. J., Dix, B., Koenig, T. K., Sinreich, R., Ortega, I., Volkamer, R., Saiz-Lopez, A., Prados–Roman, C., Mahajan, A. S., and Ordóñez, C.: Global impacts of tropospheric halogens (Cl, Br, I) on oxidants and composition in GEOS-Chem, Atmos. Chem. Phys., 16, 12239–12271, https://doi.org/10.5194/acp-16-12239-2016, 2016.

Sherwen, T., Evans, M. J., Sommariva, R., Hollis, L. D. J., Ball, S. M., Monks, P. S., Reed, C., Carpenter, L. J., Lee, J. D., Forster, G., Bandy, B., Reeves, C. E., Bloss, W. J., Monks, P. S., Oetjen, H., Plane, J. M. C., Whitehead, J. D., Sander, R., Hall, S. R., Ullmann, K., Sharp, T., Stone, D., Heard, D. E., Fleming, Z. L., Leigh, R., Shallcross, D. E., Percival, C. J., Orr-Ewing, A. J., Plane, J. M. C., Potin, P., Shillings, A. J. L., Thomas, F., Glasow, R. von, Wada, R., Whalley, L. K., and Whitehead, J. D.: Effects of halogens on European air-quality, Faraday Discuss., 16, 11433–11450, https://doi.org/10.1039/C7FD00026J, 2017a.

Sherwen, T., Evans, M. J., Carpenter, L. J., Schmidt, J. A., and Mickley, L. J.: Halogen chemistry reduces tropospheric O_3 radiative forcing, Atmos. Chem. Phys., 17, 1557–1569, https://doi.org/10.5194/acp-17-1557-2017, 2017b.

Simpson, W. R., Brown, S. S., Saiz-Lopez, A., Thornton, J. A., and von Glasow, R.: Tropospheric Halogen Chemistry: Sources, Cycling, and Impacts, Chem. Rev., 115, 4035–4062, https://doi.org/10.1021/cr5006638, 2015.

Sinnhuber, B.-M., Sheode, N., Sinnhuber, M., Chipperfield, M. P., and Feng, W.: The contribution of anthropogenic bromine emissions to past stratospheric ozone trends: a modelling study, Atmos. Chem. Phys., 9, 2863–2871, https://doi.org/10.5194/acp-9-2863-2009, 2009.

Spinei, E., Cede, A., Herman, J., Mount, G. H., Eloranta, E., Morley, B., Baidar, S., Dix, B., Ortega, I., Koenig, T., and Volkamer, R.: Ground-based direct-sun DOAS and airborne MAX-DOAS measurements of the collision-induced oxygen complex, O_2O_2, absorption with significant pressure and temperature differences, Atmos. Meas. Tech., 8, 793–809, https://doi.org/10.5194/amt-8-793-2015, 2015.

Stachnik, R. A., Millán, L., Jarnot, R., Monroe, R., McLinden, C., Kühl, S., Pukite, J., Shiotani, M., Suzuki, M., Kasai, Y., Goutail, F., Pommereau, J. P., Dorf, M., and Pfeilsticker, K.: Stratospheric BrO abundance measured by a balloon-borne submillimeterwave radiometer, Atmos. Chem. Phys., 13, 3307–3319, https://doi.org/10.5194/acp-13-3307-2013, 2013.

Stutz, J., Werner, B., Spolaor, M., Scalone, L., Festa, J., Tsai, C., Cheung, R., Colosimo, S. F., Tricoli, U., Raecke, R., Hossaini, R., Chipperfield, M. P., Feng, W., Gao, R.-S., Hintsa, E. J., Elkins, J. W., Moore, F. L., Daube, B., Pittman, J., Wofsy, S., and Pfeilsticker, K.: A new Differential Optical Absorption Spectroscopy instrument to study atmospheric chemistry from a high-altitude unmanned aircraft, Atmos. Meas. Tech., 10, 1017–1042, https://doi.org/10.5194/amt-10-1017-2017, 2017.

Thalman, R. and Volkamer, R.: Temperature dependent absorption cross-sections of O_2–O_2 collision pairs between 340 and 630 nm and at atmospherically relevant pressure, Phys. Chem. Chem. Phys., 15, 15371–81, https://doi.org/10.1039/c3cp50968k, 2013.

Thalman, R., Zarzana, K. J., Tolbert, M. A., and Volkamer, R.: Rayleigh scattering cross-section measurements of nitrogen, argon, oxygen and air, J. Quant. Spectrosc. Ra., 147, 171–177, https://doi.org/10.1016/j.jqsrt.2014.05.030, 2014.

Theys, N., Van Roozendael, M., Hendrick, F., Fayt, C., Hermans, C., Baray, J.-L., Goutail, F., Pommereau, J.-P., and De Mazière, M.: Retrieval of stratospheric and tropospheric BrO columns from multi-axis DOAS measurements at Reunion Island (21° S, 56° E), Atmos. Chem. Phys., 7, 4733–4749, https://doi.org/10.5194/acp-7-4733-2007, 2007.

Theys, N., Van Roozendael, M., Hendrick, F., Yang, X., De Smedt, I., Richter, A., Begoin, M., Errera, Q., Johnston, P. V., Kreher, K., and De Mazière, M.: Global observations of tropospheric BrO columns using GOME-2 satellite data, Atmos. Chem. Phys., 11, 1791–1811, https://doi.org/10.5194/acp-11-1791-2011, 2011.

Vandaele, A. C., Hermans, C., Simon, P. C., Carleer, M., Colin, R., Fally, S., Mérienne, M. F., Jenouvrier, A., and Coquart, B.: Measurements of the NO_2 absorption cross-section from 42 000 cm^{-1} to 10 000 cm^{-1} (238–1000 nm) at 220 K and 294 K, J. Quant. Spectrosc. Ra., 59, 171–184, https://doi.org/10.1016/S0022-4073(97)00168-4, 1998.

Volkamer, R., Baidar, S., Campos, T. L., Coburn, S., DiGangi, J. P., Dix, B., Eloranta, E. W., Koenig, T. K., Morley, B., Ortega, I., Pierce, B. R., Reeves, M., Sinreich, R., Wang, S., Zondlo, M. A., and Romashkin, P. A.: Aircraft measurements of BrO, IO, glyoxal, NO_2, H_2O, O_2–O_2 and aerosol extinction profiles in the tropics: comparison with aircraft-/ship-based in situ and lidar measurements, Atmos. Meas. Tech., 8, 2121–2148, https://doi.org/10.5194/amt-8-2121-2015, 2015.

von Glasow, R., von Kuhlmann, R., Lawrence, M. G., Platt, U., and Crutzen, P. J.: Impact of reactive bromine chemistry in the troposphere, Atmos. Chem. Phys., 4, 2481–2497, https://doi.org/10.5194/acp-4-2481-2004, 2004.

Wagner, T., Leue, C., Wenig, M., Pfeilsticker, K. and Platt, U.: Spatial and temporal distribution of enhanced boundary layer BrO concentrations measured by the GOME instrument aboard ERS-2, J. Geophys. Res. Atmos., 106, 24225–24235, https://doi.org/10.1029/2000JD000201, 2001.

Wang, S., Schmidt, J. A., Baidar, S., Coburn, S., Dix, B., Koenig, T. K., Apel, E., Bowdalo, D., Campos, T. L., Eloranta, E., Evans, M. J., DiGangi, J. P., Zondlo, M. A., Gao, R.-S., Haggerty, J. A., Hall, S. R., Hornbrook, R. S., Jacob, D., Morley, B., Pierce, B., Reeves, M., Romashkin, P., ter Schure, A., and Volkamer, R.: Active and widespread halogen chemistry in the tropical and subtropical free troposphere, P. Natl. Acad. Sci. USA, 112, 9281–9286, https://doi.org/10.1073/pnas.1505142112, 2015.

Werner, B., Stutz, J., Spolaor, M., Scalone, L., Raecke, R., Festa, J., Colosimo, S. F., Cheung, R., Tsai, C., Hossaini, R., Chipperfield, M. P., Taverna, G. S., Feng, W., Elkins, J. W., Fahey, D. W., Gao, R.-S., Hintsa, E. J., Thornberry, T. D., Moore, F. L., Navarro, M. A., Atlas, E., Daube, B. C., Pittman, J., Wofsy, S., and Pfeilsticker, K.: Probing the subtropical lowermost stratosphere and the tropical upper troposphere and tropopause layer for inorganic bromine, Atmos. Chem. Phys., 17, 1161–1186, https://doi.org/10.5194/acp-17-1161-2017, 2017.

Wilmouth, D. M., Hanisco, T. F., Donahue, N. M., and Anderson, J. G.: Fourier Transform Ultraviolet Spectroscopy of the A $^2\Pi_{3/2} \leftarrow X\,^2\Pi_{3/2}$ Transition of BrO, J. Phys. Chem. A, 103, 8935–8945, https://doi.org/10.1021/JP991651O, 1999.

Wofsy, S. C., McElroy, M. B., and Yung, Y. L.: The chemistry of atmospheric bromine, Geophys. Res. Lett., 2, 215–218, https://doi.org/10.1029/GL002i006p00215, 1975.

Yang, X., Cox, R. A., Warwick, N. J., Pyle, J. A., Carver, G. D., O'Connor, F. M., and Savage, N. H.: Tropospheric bromine chemistry and its impacts on ozone: A model study, J. Geophys. Res., 110, D23311, https://doi.org/10.1029/2005JD006244, 2005.

Supplement of Atmos. Chem. Phys., 17, 15245–15270, 2017
https://doi.org/10.5194/acp-17-15245-2017-supplement

Atmospheric Chemistry and Physics
Open Access
EGU

Supplement of

BrO and inferred Br_y profiles over the western Pacific: relevance of inorganic bromine sources and a Br_y minimum in the aged tropical tropopause layer

T. K. Koenig et al.

Correspondence to: Rainer Volkamer (rainer.volkamer@colorado.edu)

Glossary of abbreviations and symbols

Abbreviation	Definition
2D-C	2D-C Hydrometeor Probe
AMAX-DOAS	Airborne MAX-DOAS
AMF	Air Mass Factor
AP1	AMAX-DOAS Acton Pixis covering 330-470 nm
AP2	AMAX-DOAS Acton Pixis covering 440-700 nm
ATTREX	Airborne Tropical TRopopause EXperiment
AWAS	Advanced Whole Air Sampler
BAe-146	British Aerospace 146 aircraft
box-AMF	Air Mass Factor computed in Radiative Transfer Model gridbox
Br	Bromine atom, atomic bromine
BrCl	Bromine chloride
$BrNO_2$	Bromine nitrite
BrO	Bromine monoxide
BrO_3^-	Primary bromide ozonide
$BrONO_2$	Bromine nitrate
BrO_x	Active bromine (= Br + BrO)
Br_y	Total inorganic bromine (= Br + Br_2 + BrO + $BrNO_2$ + $BrONO_2$ + HBr + HOBr + BrCl + IBr)
CAST	Coordinated Airborne Studies in the Tropics
CalNex	California Nexus field campaign
CAM-Chem	Community Atmospheric Model with Chemistry
CCD	Charge Coupled Device
CDP	Cloud Droplet Probe
CFC-11	Trichlorofluoromethane
CH_4	Methane
CH_2Br_2	Dibromomethane, methylene bromide
CH_2BrCl	Bromochloromethane
CH_2IBr	Briomoiodomethane
$CHBrCl_2$	Bromodichloromethane
$CHBr_2Cl$	Dibromochloromethane
$CHBr_3$	Bromoform

CHOCHO	Glyoxal
CI	Confidence Interval
CIMS	Chemical Ionization Mass Spectrometry
CO	Carbon monoxide
CO_2	Carbon dioxide
CONTRAST	CONvective TRansport of Active Species in the Tropics
CRDS	Cavity Ring Down Spectrometer
CU	University of Colorado
dSCD	Differential Slant Column Denisty
DOAS	Differential Optical Absorption Spectroscopy
EA	Elevation Angle
FT	Free Troposphere
FWHM	Full width half maximum
GC-MS	Gas Chromatograph - Mass Spectrometer
GEOS CCM	Goddard Earth Observing System with Chemistry-Climate Model
GEOS-Chem	Goddard Earth Observing System with Chemistry model
GEOS-FP	Goddard Earth Observing System Forward-Processing data products
GMAO	Global Modelling and Assimilation Office
GT	Georgia Institute of Technology
GV	NCAR/NSF Gulfstream V aircraft (synonym for HIAPER)
H_2O	Water
HARP	HIAPER Atmospheric Radiation Package
HAIS	Hyper Aircraft Instrumentation Solicitation
HBr	Hydrogen bromide, hydrobromic acid
HCR	Heterogeneous Chemical Regimes
HCHO	Formaldehyde
HEFT-10	HAIS Experimental Flight Test 2010
HIAPER	High-Performance Instrumental Airborne Platform for Environmental Research (synonym for NSF/NCAR GV)
HSRL	High Spectral Resolution Lidar
HOBr	Hypobromous acid
HO_2	Hydroperoxy radical
HO_x	Hydrogen oxide radicals (= OH + HO_2)

IBr	Iodine bromide
ISAF	In Situ Airborne Formaldehyde
IO	Iodine monoxide
J	Photolysis rate
k	Reaction rate
LLS	Longer Lived Species (of organohalogens)
LS	Lower Stratosphere
MAX-DOAS	Multi AXis - DOAS
MBL	Marine Boundary Layer
MU	Manchester University
NASA	National Aeronautics and Space Administration
NCAR	National Center for Atmospheric Research
NIR	Near infrared
NSF	National Science Foundation (USA)
NO	Nitrogen monoxide
NO_2	Nitrogen dioxide
NO_x	Active nitrogen oxides (= NO + NO_2)
O_3	Ozone
O_4	Oxygen collision pair (O_2-O_2)
OH	Hydroxy radical
OVOC	Oxygenated Volatile Organic Compound
PGI	Product Gas Injection (of organohalogens)
PMT	Photon Multiplier Tube
ppb	Parts per billion (nmol mol^{-1})
ppm	Parts per million (μmol mol^{-1})
ppt	Parts per trillion (pmol mol^{-1})
QDOAS	DOAS analysis software
RF	Research flight
RTM	Radiative Transfer Model
S(IV)	The +4 oxidation state of sulfur
SA	Surface Area
SCD	Slant Column Density
SGI	Source Gas Injection (of organohalogens)

SSA	Sea-Salt Aerosol
SZA	Solar Zenith Angle
TL	Transition Layer
TOGA	Trace Organic Gas Analyzer
TTL	Tropical Tropopause Layer
TTL-LMS	Tropical Tropopause Layer – LowerMost Stratosphere
tWPO	tropical Western Pacific Ocean
UHSAS	Ultra-High Sensitivity Aerosol Spectrometer
UTC	Coordinated Universal Time
UTLS	Uppper Troposphere - Lower Stratosphere
VCD	Vertical Column Density
VCSEL	Vertical Cavity Surface Emitting Laser
VSLS	Very Short Lived Species (of organohalogens)
VMR	Volumn Mixing Ratio
VUV	Vacuum Ultra-Violet
WS-CRDS	Wavelength-Scanned CRDS
γ	Surface reaction/uptake probability
θ	Potential temperature
λ	Wavelength

Jet Cross Case Studies Description

Results from two jet cross flights are included in this work, the flight tracks are shown in Fig. 1. The jet location as crossed in RF15 is also shown. The location of the jet during RF06 is not fully corroborated by measurements as in RF15, but was forecast to be very near the northernmost point of RF06 at 32°N.

The atmospheric context of RF06 is shown in Fig. S5. The data included for modeling starts at 01:16 UTC on 25 January, when the aircraft was at 23.65°N, 148.41°E, and 13.1km altitude. The flight path was NNW almost level at 13.2 km altitude, with small stepwise ascents in the latter portion of the flight. Figure S5 shows that horizontal wind increased as the aircraft approached the subtropical jet stream. At 01:35 UTC the aircraft crossed from the convective TTL to the aged TTL, changes in CO and θ corroborate those in O_3 and H_2O. The aircraft entered the jet at 13.2 km and 28.42°N, horizontal wind peaked just below 70 m s^{-1}. At 02:18 UTC, 32.12°N, 149.90°E, and 13.3 km the GV reversed course, heading SSW continuing to climb. Between 03:20 and 04:00 UTC the aircraft flew at a consistent altitude between 14.3 km and 14.4 km, traveling through the convective TTL transition. The remainder of the flight from 04:00 to 04:56 UTC sampled the more typical convective TTL, including instances of convection.

Figure 3 shows a number of atmospheric tracers for RF15. The data included for modeling start at 00:26Z on 25 February, when the aircraft was at 24.01°N, 145.14°E, and 13.1 km altitude. The aircraft traveled almost due north, with occasional climbs as geopotential altitude gradually decreased. The tropospheric approach of the jet was similar to RF06. The GV transitioned from the convective TTL to the aged TTL at 01:01 UTC, and the jet was first encountered at 01:12 UTC, reaching peak windspeed near 80 m s^{-1}. A second component of the jet with the slower windspeed (~65 m s^{-1}) was similar to the most stratospheric of the air masses encountered during RF 06: i.e., 100 ppb < O_3 < 200 ppb, and H_2O/O_3 ~ 0.02 ppm/ppb, characteristic of the TTL. At 01:35 UTC, 32.92°N and 12.9 km, O_3 increased sharply indicating the transition into the stratosphere, and windspeed decreased as the GV crossed into the middleworld LS. Although not shown on Fig. 4, this transition was marked the first time CFC-11 deviated consistently from tropospheric values, indicating long residence at high altitude with photochemical processing of the sampled air masses. At 02:25 UTC the aircraft encountered a second rapid O_3 gradient, traveled to the maximum flight latitude of 40.13°N, climbed from 12.6 to 12.9 km, reversed course to due south, and transitioned from the middleworld to the overworld at 02:32 UTC. At 03:26 UTC at 13.5 km and 33.14°N the GV crossed from the overworld back to the aged TTL, skipping the LS middleworld. Nothing analogous to the convective TTL "transition" in RF06 was encountered during RF15. Instead there was a smooth change from the aged TTL to the convective TTL at 4:21 UTC. Instances of convection were first encountered at 04:38 UTC.

Gas Phase Measurements Used to Constrain the Box Model

The measurements used to constrain the box model to infer Br_y from BrO are summarized in Table 1. The handling of AMAX-DOAS data is described in detail in the main text (Sect. 2.1). Other data were used in the following manner with specific exceptions outlined here after. Where data were below detection limit the nominal value of ½ the detection limit was used. With the exception of NO_2 discussed below no parameter impacted Br_y partitioning significantly at the relevant level when near its respective detection limit. Where data was quality flagged it was interpolated across.

High frequency data ~1 Hz, namely Chemiluminescence (NO, NO_2, and O_3), HARP photolyses, ISAF HCHO, PICARRO CH_4, UHSAS aerosols, Aerolaser VUV fluorescence CO, and state parameters were averaged over the relevant interval. For profiles this was at the 500 m of flight altitude, for level flight relevant periods of ~ 5 minutes. Lower frequency data, namely AWAS and TOGA were interpolated to the mean; for level flight they were interpolated in altitude, for level flight they were interpolated in time.

Early research flights including the profile case studies had incomplete data coverage. In particular, AWAS data were not available for RF03 and RF04; PICARRO and Aerolaser VUV fluorescence for RF03; and ISAF for a portion of RF04. For AWAS measurements with the exception of ethane TOGA measurements were available which were substituted. For ethane, AWAS ethane was compared to Picarro methane for tropical profiles from RF05, RF06, and RF07 to obtain an average ratio of ethane:methane of 1.59×10^{-4}:1. This ratio was used to obtain an ethane concentration from the methane concentration for RF03 and RF04. For RF03 where CO and CH_4 were not available the mean profiles for each species from GEOS-Chem were used. For the portion of RF04 where ISAF HCHO is not available, TOGA HCHO is substituted.

AWAS and TOGA measure some of the same species used in the box model (propane, isobutane, n-butane, and benzene). AWAS data were used for these species for level flight data, where detection limits give more complete coverage in stratospheric air; while TOGA data were used for the profile case studies, where it has a higher frequency and more consistent coverage, further AWAS data is unavailable for RF03 and RF04. The agreement between TOGA and AWAS differs among the species measured, but very rarely exceeds their respective reported errors. CFC-11 and bromocarbon measurements were examined to further understand differences, corroborating the level of agreement for hydrocarbons. The species used in the box model (propane, isobutane, n-butane, and benzene) impact Br_y partitioning via alkylperoxy radicals which do not impact sufficiently by differences to have a significant impact.

NO_2 can have a significant impact on Br_y partitioning, not only via direct reaction but indirectly through impacts on HO_x. At high altitude, some Chemiluminescence measurements of NO_2 were less than zero. These data were averaged with GEOS-Chem NO_2 in order to have a physically meaningful value but remain generally consistent with the observations of NO_2 below the levels elsewhere. Further for the RF15 case study, the Leighton ratio deviates significantly from model predictions, and AMAX-DOAS NO_2 was used to constrain the box model for this flight (Fig. S1). In the TTL, despite different measurement principles, AMAX-DOAS and Chemiluminescence NO_2 were roughly consistent and generally elevated relative to box models and global model predictions. In the stratosphere high ambient O_3 may impact Chemiluminescence measurements of NO_2, which deviated further from model predictions. AMAX-DOAS NO_2, however, while elevated relative to box models, is roughly consistent with CAM-Chem.

Gas Phase Measurement Techniques

Advanced Whole Air Sampler (AWAS)

The Advanced Whole Air Sampler (AWAS) consists of modules of 12 custom stainless-steel 1.3 L sampling canisters. Typically five modules (60 canisters) were collected in a flight, sampling was determined by an inflight operator. Sample flow was altitude dependent and varied between 5 slpm and 30 slpm. These samples can then be analyzed for a wide variety of hydrocarbons, halocarbons, organonitrates, and other species.

Samples are analyzed on the ground after flight using a Markes Canister Interface 5 (CIA) and a Unity II system connected to an Agilent 5975 GC/MSD. Samples were dried and pre-concentrated on Markes Ozone Precursor Trap (Markes UT17O3P-2S). Samples of 800 scc are thermally desorbed at 300 °C and split between two GC, 1) a 30 m x 0.25 mm x 5 micron Alumina 10 PLOT column (HP-AL/S, Agilent Technologies) followed by a 1 m GasPro with a flame ionization detector, and 2) a 20 m x 0.2 mm x 1.12 μm DB-624 column (128-1324, Agilent Technologies) to both an electron capture detector and the MSD. Further details on sampling and analysis can be found in Andrews et al. (2016) and Navarro et al. (2015). Calibration was done every five samples against a cryogenically collected standard which in turn is calibrated by a procedure described in Schauffler et al. (1999).

Chemical Ionization Mass Spectrometer (CIMS)

The Georgia Tech CIMS (GT CIMS) measured gas phase bromine species (BrO, and HOBr +Br_2), it is more fully described in Chen et al. (2016). In brief the instrument sampled air from outside the GV through a Teflon tube, ionized

by water-iodide clusters in a flow tube, ions are further processed in a collisional dissociation chamber (CDC), guided by an octopole field, and then analyzed on a mass spectrometer. Air was sampled at 5.2 standard litres per minute (sLpm). HOBr is known to process to Br_2 on the inlet and the sum of the detected signals is used as a result. Up to 1.7 sLpm of this was sampled off the line by an automatic variable orifice with the remainder exhausted to maintain a constant 50 Torr pressure in the flow tube. CH_3I at a few ppm in 2.9 sLpm N_2 buffer gas was flowed over a ^{210}Po source to generate iodide and then mixed with 0.1 sLpm humidified N_2 to provide hydrated iodide ions in the flow tube. Gas phase bromine species reacted with these to form clusters. Water was removed from the clusters by the electric field in the CDC which in addition has a vacuum maintained independent of the flow tube. The core ions, dehydrated iodide-analyte clusters, were then guided by the octopole then selected and detected on the quadrapole. The consistency of detected signals from the bromine isotopes ^{79}Br and ^{81}Br was used as a data quality check.

Chemiluminescence

Two instruments measure the trace gasses NO, NO_2, and O_3 using chemiluminescence of the $NO+O_3$ reaction. The first is a two channel detector for NO and NO_2. Air sampled from outside the aircraft is split onto the channels. On the NO_2 channel, UV light at 395 nm is used to photolyse NO_2 to NO. Both channels are then reacted with O_3 from two ozonizers, PMT detectors measure the emission of the NO_2^* product at 600 nm - 2800 nm. NO in N_2 is used as a calibration gas. The Fast-O_3 detects O_3 using a similar system. Ambiently sampled O_3 is reacted with reagent grade (> 99%) NO, and the same product is detected using a PMT.

In Situ Airborne Formaldehyde (ISAF)

The In Situ Airborne Formaldehyde (ISAF) instrument utilizes laser induced fluorescence (LIF) at 353.16 nm to selectively measure formaldehyde in air collected off an inlet. A pulsed tunable fiber laser is rapidly tuned on and off of the rotational resonance feature which minimizes interference and serves as a real time monitoring of background. The resulting fluorescence is monitored by a PMT. The instrument was calibrated by standard addition of formaldehyde before and after the campaign. A more complete description of ISAF is available in Cazorla et al. (2015).

Piccaro CO_2/CH_4 Flight Analyzer

The Piccaro G1301-c Methane/Carbon Dioxide Analyzer utilizes Wavelength-Scanned Cavity Ring Down Spectroscopy (WS-CRDS) driven by an NIR laser. Gas sampled from outside the aircraft is circulated through a cavity with an effective path length of 20km. The instrument has been ruggedized for aircraft operation and utilizes a patented, high-precision wavelength monitor to minimize interference from other trace gasses. Only methane is used in the box model.

Trace Organic Gas Analyzer (TOGA)

TOGA consists of a custom GC-MS system which measures a variety of species including hydrocarbons, halocarbons, and non-acid oxygenated volatile organic compound (OVOC). Samples are collected off the main inlet line at 15 ml

per minute for 35 seconds through a series of three cold traps, then run on a custom GC with a Restek MXT-624 column. Effluent from the GC is analyzed on an Agilent Technologies 5973N quadrupole mass spectrometer system ruggedized for aircraft use by substitution of the vacuum pump with a Varian Model V301 NAV. Total time to process a single sample is 2.0 minutes. Further details on TOGA can be found in Andrews et al. (2016) and Apel et al. (2003, 2010, and 2015).

VUV Carbon Monoxide

The VUV carbon monoxide instrument generates vacuum UV light through RF plasma discharge, this is bandpass filtered (8 nm FWHM) around 150 nm to excite CO fluorescence while minimizing interference from water. Fluorescence is monitored by PMT. A more complete description of the instrument is available in Gerbig et al. (1999).

Particle Measurements

2D-C Hydrometeor Probe (2D-C)

The 2D-C Hydrometeor Probe is customized through installation on high speed electronics and installation of a 64 element photodiode array from a product originally produced by Particle Measuring Systems Inc. An open path between two arms perpendicular to flight is illuminated and images of individual particles are imaged on the 64 element array. Particles with diameters between 62.5 μm and 1587.5 μm are detected, though the depth of field limits sensitivity to smaller particles. Furthermore, the arms are known to shatter larger particles, though they have been designed to minimize this effect. 2D-C images were not directly referenced, rather, a processed data product classifying particles into 60 size bins was used an indication of cirrus clouds. Calculations of cirrus ice surface area were used to inform box model sensitivity studies as discussed in Section 2.3.1.

Cloud Droplet Probe (CDP)

The Cloud Droplet Probe (CDP) manufactured by Droplet Measurement Technologies, Inc. utilizes forward scattering to detect particles in the range of 2 μm to 50 μm in size. A diode laser is run across an open path perpendicular to flight. Particles which pass through the depth of field in the open path are counted and sized into one of 30 bins in the size range. A more complete description of the CDP is available in Lance et al. (2010). CDP data was referenced and utilized in sensitivity studies but not ultimately utilized in the box model. This is discussed in Section 2.3.1.

Ultra-High Sensitivity Aerosol Spectrometer (UHSAS)

The wing-mounted Ultra-High Sensitivity Aerosol Spectrometer utilizes a laser at 1054 nm to optically detect particles along the GV flight path. The instrument is sensitive to particles in the 0.060 μm to 1.0 μm diameter range and records particles into 99 roughly logarithmic size bins covering this size range. During CONTRAST, however, frequent noise necessitated discarding the smallest twelve bins, making 0.084 nm the effective lower bound of the probe. A more complete description of a ground-based version of the UHSAS may be found in Cai et al. (2008). UHSAS data were used in the box model for all flights to compute aerosol surface area for heterogeneous reactions. Furthermore,

sensitivity studies were conducted increasing diameter by a factor of two based on the results of a previous optical closure study (Volkamer et al., 2015); this is further illustrated for the RF03 profile in Fig. S3. Increasing particle size by a factor of two leads to general agreement between AMAX-DOAS retrieved extinction using O_4 and extinction computed from UHSAS using Mie theory above ~3 km. In the boundary layer even increasing particle size and including supermicron particles from the CDP still yields sub-Rayleigh scattering at 360 nm, significantly below the extinction measured by AMAX-DOAS.

Meteorological Parameters

HIAPER Airborne Radiation Package (HARP)

The HIAPER Airborne Radiation Package (HARP) includes CCD spectroradiometers, and irradiance detectors measuring upwelling and downwelling radiation. Detectors are mounted on an actively motion stabilized platform to maintain horizontal stability despite aircraft deviations of up to 5 degrees. Data from the spectroradiometers was used in this work. These measure actinic flux in the range of 280 nm to 680 nm. These are then processed using a modified version of the Tropospheric Ultraviolet and Visible (TUV) radiative transfer model to generate photolysis frequencies for a wide variety of species including O_3, NO_y species, small aldehydes and ketones, organonitrates, Br_y species, and Cl_y species. These were used for all photolysis reactions used in the box model. Further details on HARP can be found in Pilewskie et al. (2003) and Shetter and Müller (1999).

Vertical Cavity Surface Emitting Laser (VCSEL) hygrometer

The Vertical Cavity Surface Emitting Laser (VCSEL) a tunable NIR laser based hygrometer measuring absolute water concentration. The instrument achieves a high dynamic range by monitoring two different water absorptions at two similar wavelengths, a 'strong' absorption at 1854.03 nm and a 'weak' one at 1853.37 nm. The cavity has a physical extent of 14.95 cm which is passed 25 times for a path length of 3.74 m. Measurement is typically done by second harmonic detection except in the mid-troposphere where the second harmonic of the strong band is nonlinear and direct absorption is used. Further information on VCSEL is available in Zondlo et al. (2010).

GV State Parameters

The National Science Foundation/National Center for Atmospheric Research Gulfstream V (NSF/NCAR GV) aircraft records a wide variety of state parameters. Some of these such as temperature and pressure were utilized in the box model. Others such as θ and horizontal wind speed were used as context for model results. Finally, in order to match the spatial scale probed by in situ sensors and remote sensors, the median photon sampled by the AMAX-DOAS was calculated by radiative transfer, and the in situ data were averaged, and shifted in time to match DOAS sampled air volumes. For the horizontal case studies – RF06 and RF15 – the lateral wind speed was strong, such that the aircraft heading and the measurement vector are offset by approximately 5°. No further corrections were made to attempt account for this perpendicular offset. However, the air masses probed remotely are blown towards the aircraft, and the time delay at which the in situ data were averaged partially account for this offset.

Statistical tests of the local maxima/minima of Br_y in the convective upper FT and aged TTL

We test whether there is a local minimum in the aged TTL in three steps, first we assess the likelihood that Br_y in the aged TTL is less than Br_y in the convective TTL and upper FT ($B_{ry\ aTTL} < B_{ry\ uFT,cTTL}$), second the probability that Br_y in the aged TTL is less than Br_y in the lower stratosphere ($B_{ry\ aTTL} < B_{ry\ LS}$), and finally the joint probability that these are simultaneously true.

Comparison of inferred Br_y in the upper FT and convective TTL with the aged TTL presents a challenge, the distribution of inferred Br_y values in the upper FT and convective TTL is skew and not normally distributed; to tackle this a Wilcoxon-Mann-Whitney rank test is used (Mann and Whitney, 1947). In brief, this method sums for elements from one distribution the number of elements from the other distribution which they are greater than, termed the *U*-statistic. The *U*-statistic is assessed against a null hypothesis; because the distributions (e.g. variance and skew) of Br_y in the upper FT and convective TTL, and in the aged TTL are dissimilar a one-tailed null hypothesis is stated in terms of stochastic ordering. Specifically, we test against the null hypothesis, H_0: $Br_{y\ a} \geq_{st} Br_{y\ b}$, i.e. that for any and all concentrations of Br_y the likelihood of a random inferred Br_y in region a is greater than that concentration is greater than the likelihood that a random inferred Br_y in region b is greater than the same concentration. A statistic related to U, ρ, assesses the overlap of the data sets; a value of 0.5 indicates a statistical tie, while values of 0 and 1 indicate a sweep for one set or the other.

Applying Wilcoxon-Mann-Whitney rank tests we find that Br_y in the aged TTL is lower than in the convective TTL and in the upper FT ($U = 2781$, $n_{uFT,cTTL}=111$, $n_{aTTL}=60$, $\rho=0.4176$, $p<0.04$, reject H_0: $Br_{y\ aTTL} \geq_{st} Br_{y\ uFT,cTTL}$), and that it is lower than in the lower stratosphere (LS) ($U = 4$, $n_{uFT,cTTL}=51$, $n_{aTTL}=60$, $\rho=0.0013$, $p<<0.01$, reject H_0: $Br_{y\ aTTL} \geq_{st} Br_{y\ LS}$). The p value for the second test is vanishingly small; applying the Vysochanskij-Petunin modification of the Chebyschev inequality obtains a more conservative value of $p \approx 0.02$. Taking the more conservative significance and using the Bonforroni-Holm (Holm, 1979) method we can reject both null hypotheses with $p<0.05$. With 95% confidence there is a Br_y minimum in the aged TTL.

The Wilcoxon-Mann-Whitney rank tests was also applied to assess whether Br_y in the mid FT is lower than in the convective TTL and in the upper FT ($U = 2034$, $n_{uFT,cTTL}=111$, $n_{mFT}=51$, $\rho=0.3593$, $p<0.02$, reject H_0: $Br_{y\ mFT} \geq_{st} Br_{y\ uFT,cTTL}$). This is used to infer that the tropospheric profile has a maximum at altitude and is C-shaped with 98% confidence.

Supplemental Tables and Figures

Table S1: Parameters input and output for optimal estimation.

Parameter	**RF03**	**RF04**	**RF07**
p, T, H_2O, NO_2, O_3, O_4	in situ data where available, model above flight altitude		
Aerosol Properties			
AOD (360 nm)	0.304	0.272	0.231
g-parameter	0.77 (0-2.4 km), 0.72 (2.4-6.0 km), 0.7 (>6.0 km)		
Single Scattering Albedo	0.98		
Surface Albedo	0.05		
Inversion Properties			
ab initio profile	1.0 ppt constant tropospheric mixing ratio		
ab initio error	2,000%	10,000%	10,000%
Inversion Grid	500 m (aerosol at 200 m resolution)		
Degrees of Freedom	18.2	17.2	26.9
Mean Averaging Kernel	0.728	0.953	0.962

Table S2: Comparisons of partial and total tropospheric HBr VCDs predicted by different models.

Altitude	**HBr VCD $\times 10^{12}$ (box-model -case 1)**	**HBr VCD (GEOS-Chem no SSA source)**	**HBr VCD (GEOS-Chem w/ SSA source)**	**HBr VCD (CAM-chem)**
MBL	0.0 (0.0, 0.0)	0.1 (0.0, 0.8)	5.2 (0.8, 9.0)	0.8 (0.4, 2.9)
TL	0.0 (0.0, 0.0)	3.1 (1.5, 5.4)	18.9 (9.3, 28.4)	3.1 (1.1, 6.5)
Lower FT	0.0 (0.0, 0.1)	6.2 (3.7, 9.2)	14.6 (7.6, 27.3)	9.0 (3.9, 17.0)
Mid FT	0.3 (0.1, 0.8)	1.5 (0.9, 2.6)	2.3 (1.0, 4.4)	2.7 (0.7, 5.2)
Upper FT	2.7 (2.1, 5.2)	2.2 (1.6, 2.7)	3.4 (2.6, 4.1)	1.0 (0.0, 1.7)
TTL	0.1 (0.0, 0.8)	1.0 (0.6, 1.3)	1.5 (0.9, 1.9)	0.3 (0.0, 0.9)
Troposphere	3.2 (2.1, 6.8)	14.1 (8.3, 22.0)	46.0 (22.2, 75.2)	17.0 (6.2, 34.3)

Values in parentheses are the 1st and 3rd quartile. Global models have much more HBr, especially in the lower atmosphere. This is likely related to the handling of HBr uptake as discussed in the text. The global models also show an HBr minimum in the upper FT and TTL, which is the box model maximum.

Table S3: Summary of BrO and Br_y over the tWPO.

Region	BrO ppt	Br_y ppt			
		case 0	**case 1**	**case 2**	**case 3**
MBL	1.7 (0.2, 1.0, 3.8, 4.4)	13.8 (2.0, 5.5, 30.2, 35.0)	13.8 (2.0, 5.5, 30.2, 35.0)	13.8 (2.0, 5.5, 30.2, 35.0)	13.8 (2.0, 5.5, 30.2, 35.0)
TL	1.2 (0.3, 0.6, 1.3, 1.8)	5.8 (1.9, 3.4, 8.7, 12.4)	5.8 (1.9, 3.4, 8.7, 12.4)	5.8 (1.9, 3.4, 8.7, 12.4)	5.8 (1.9, 3.4, 8.7, 12.4)
lFT	0.7 (-0.1, 0.4, 0.9, 1.2)	2.8 (0.9, 1.6, 5.0, 6.1)	2.8 (0.9, 1.6, 5.0, 6.1)	2.8 (0.9, 1.6, 5.0, 6.1)	2.8 (0.9, 1.6, 5.0, 6.1)
mFT	0.6 (0.1, 0.5, 1.0, 1.3)	3.6 (0.8, 1.7, 5.1, 6.0)	1.6 (0.8, 1.2, 3.5, 4.1)	1.6 (0.7, 1.2, 3.4, 3.9)	1.6 (0.7, 1.2, 3.4, 3.9)
uFT	0.6 (0.2, 0.3, 0.7, 0.8)	6.2 (2.1, 2.6, 7.6, 10.9)	2.1 (0.8, 1.5, 3.1, 6.2)	1.7 (0.5, 0.7, 2.1, 2.3)	1.7 (0.5, 0.7, 2.1, 2.3)
cTTL	0.9 (0.3, 0.5, 1.1, 1.1)	4.8 (2.9, 4.0, 6.5, 10.5)	3.3 (1.7, 2.6, 4.2, 5.3)	2.6 (1.4, 1.8, 3.1, 3.4)	2.6 (1.4, 1.8, 3.1, 3.4)
aTTL	1.2 (0.7, 0.9, 1.8, 1.9)	2.7 (1.7, 2.1, 3.6, 4.2)	2.7 (1.6, 2.0, 3.5, 4.1)	2.6 (1.6, 2.0, 3.4, 3.9)	2.6 (1.6, 2.0, 3.2, 3.7)
LS	3.1 (2.6, 2.8, 3.2, 3.3)	6.9 (5.5, 6.5, 7.5, 8.2)	6.8 (5.5, 6.4, 7.5, 8.2)	6.9 (5.5, 6.5, 7.5, 8.2)	6.0 (4.9, 5.7, 6.5, 7.0)

Values in table are reported as follows: median, (1^{st} decile, 1^{st} quartile, 3^{rd} quartile, 9^{th} decile). Air masses are classified as elsewhere, see Sects. 3.1 and 3.2.

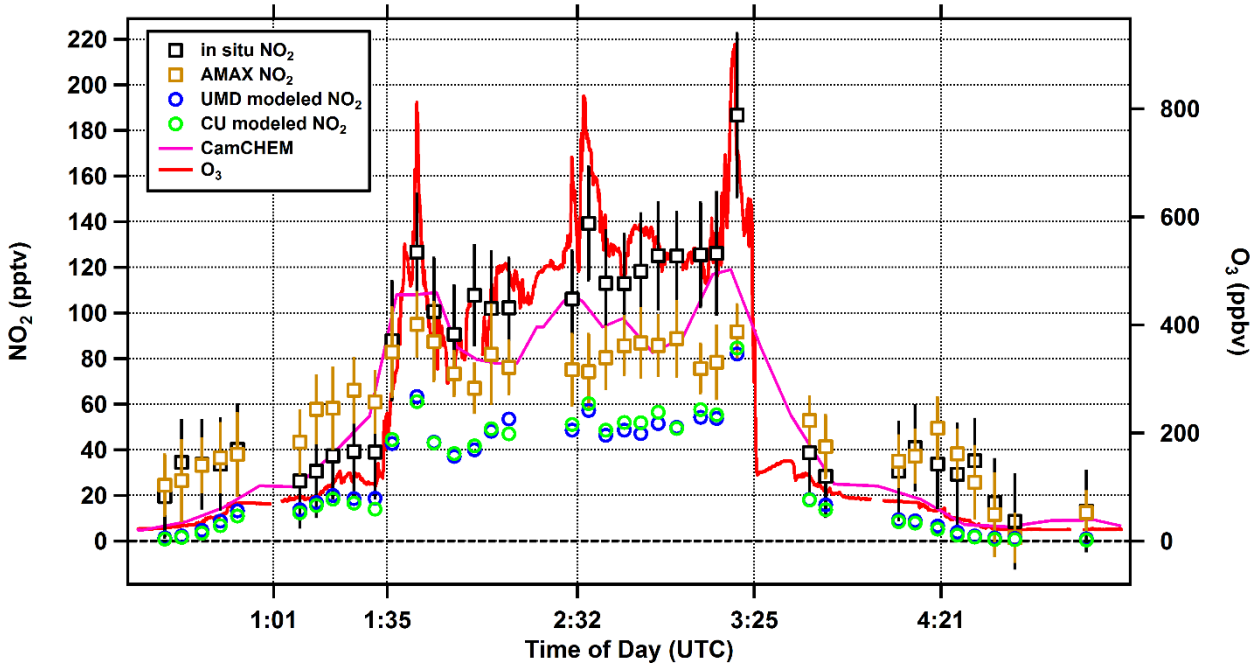

Figure S1: Comparison of NO_2 between (black) in situ NO_2, (gold) DOAS NO_2, (green) NO_2 modeled using the box model constrained by in situ measured NO, (blue) NO_2 modeled by a second box model operated at the University of Maryland, constrained by in situ measured NO. AMAX-DOAS and in-situ NO_2 agree within error bars in the troposphere. However, DOAS is systematically lower than in-situ NO_2 in the stratosphere, where high O_3 is believed to introduce a high bias to the in situ NO_2 measurements; O_3 is shown in red on the right axis. DOAS NO_2 was used to constrain the box model in this case study.

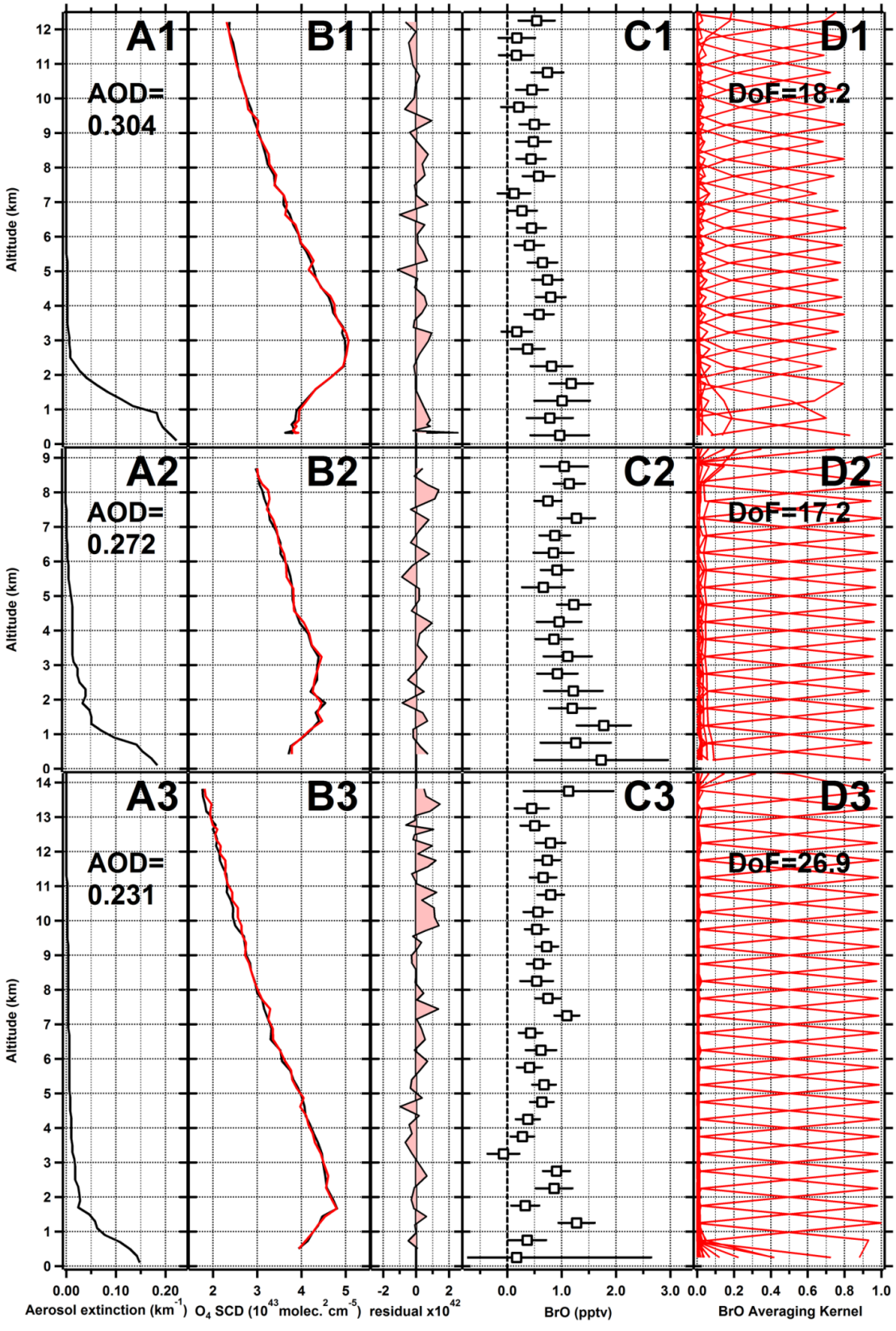
A1
AOD=
0.304
B1
C1
D1
DoF=18.2
A2
AOD=
0.272
B2
C2
D2
DoF=17.2
A3
AOD=
0.231
B3
C3
D3
DoF=26.9
Altitude (km)
Aerosol extinction (km-1)
O4 SCD (1043 molec.2 cm-5)
residual x1042
BrO (pptv)
BrO Averaging Kernel

Figure S2: Optimal estimation of BrO profiles for case studies 1) RF03, 2) RF04, 3) RF07. Panels A: the retrieved aerosol extinction profile at 360 nm, the aerosol optical depth is integrated over the column retrieved assuming zero above maximum flight altitude. Panels B: left subpanel in black measured O_4 SCDs, in red modeled O_4 SCDs, right subpanel the residual (modeled-measured), individual residuals are within $\pm 2\times10^{42}$. Panels C: The BrO profiles retrieved by optimal estimation, error bars include fit error, and optimal estimation errors. Panels D: averaging kernels for the BrO optimal estimation. Sharp peaks near 1 indicate independent information in each altitude bin. The Degrees of Freedom (DoF) is the trace of the matrix here truncated to flight altitudes.

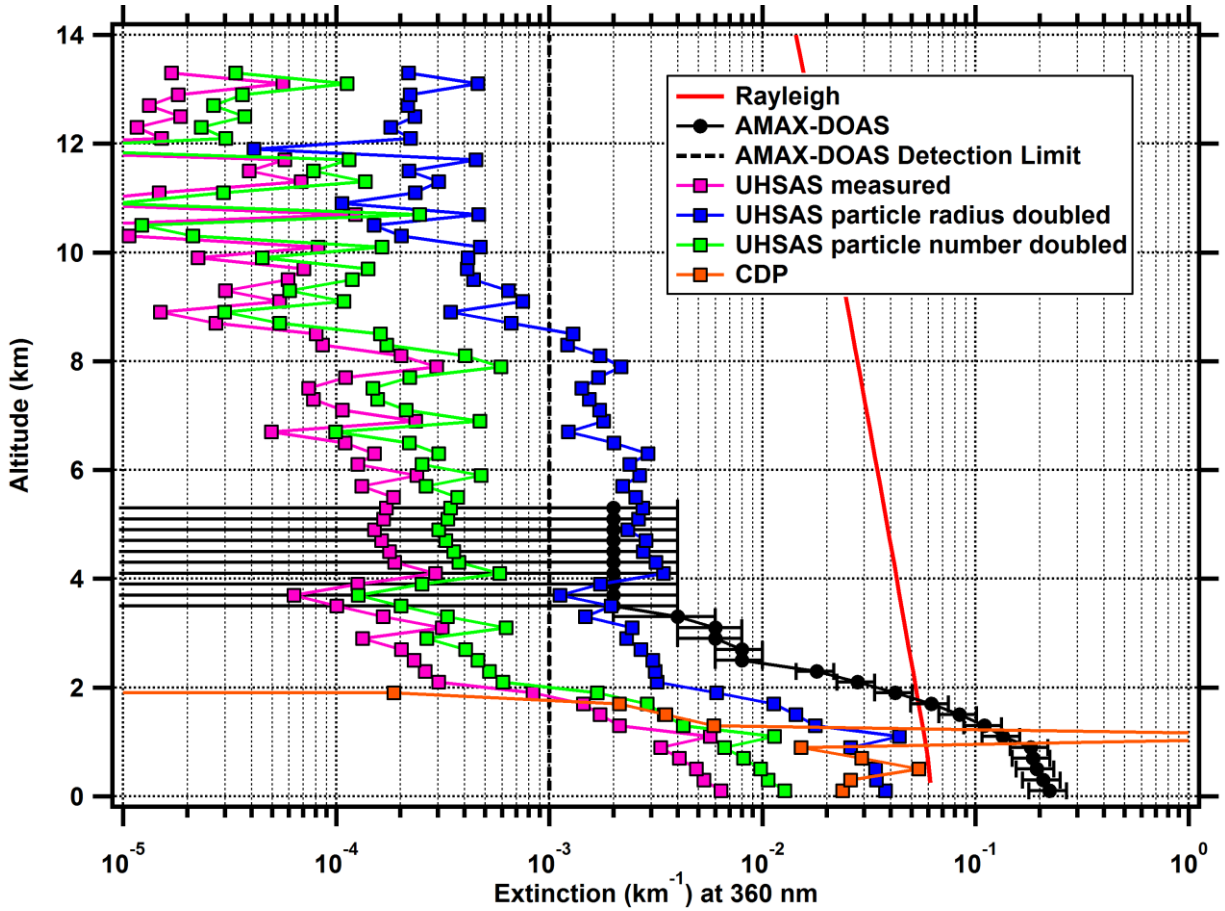

Figure S3: Comparison of aerosol extinction at 360 nm for the RF03 case study profile. AMAX-DOAS extinction is retrieved based on O_4 dSCDs. Particle instrument extinctions are determined by using Mie theory with measured particle size distributions and concentrations as input. Consistent with the findings in Volkamer et al. (2015) measured size distributions do not reproduce the observed extinction and are sub-Rayleigh even in the boundary layer. Increasing particle size improves agreement.

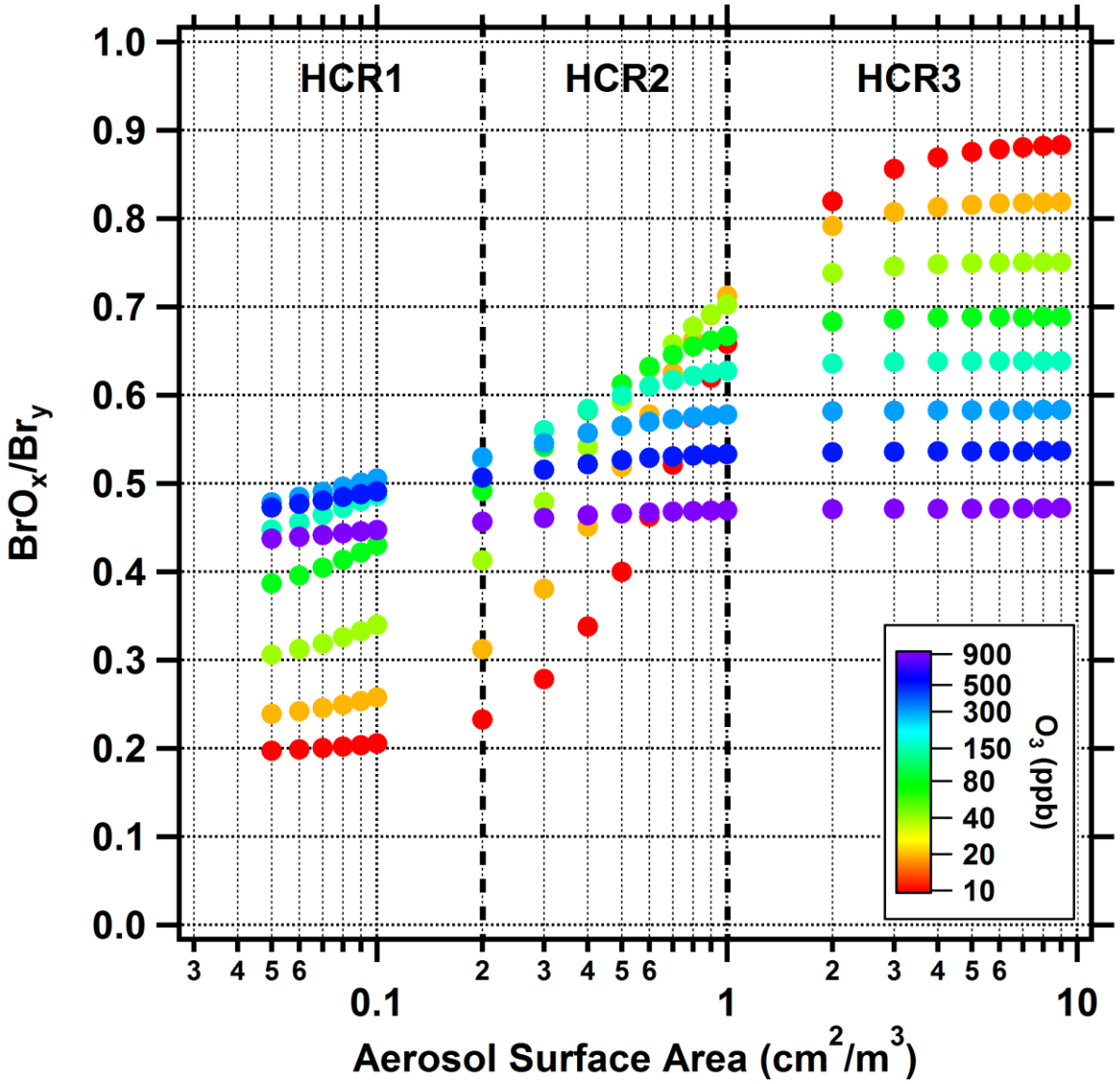

Figure S4: Sensitivity of the BrO_x/Br_y ratio to SA and O_3, under conditions typical of the upper troposphere. (dashed vertical lines) the heterogeneous chemical regimes (HCR, see Sect. 2.3.1). The decreasing HBr fraction with increasing O_3 is visible in HCR1, and is a result of lower bromine atom concentrations (and thus HBr formation rates). HCR2 exhibits the largest sensitivity at low/moderate O_3, typical of the upper FT (uFT) and convective TTL (cTTL). In HCR3 the ratio is largely insensitive to SA, but strongly depends on O_3.

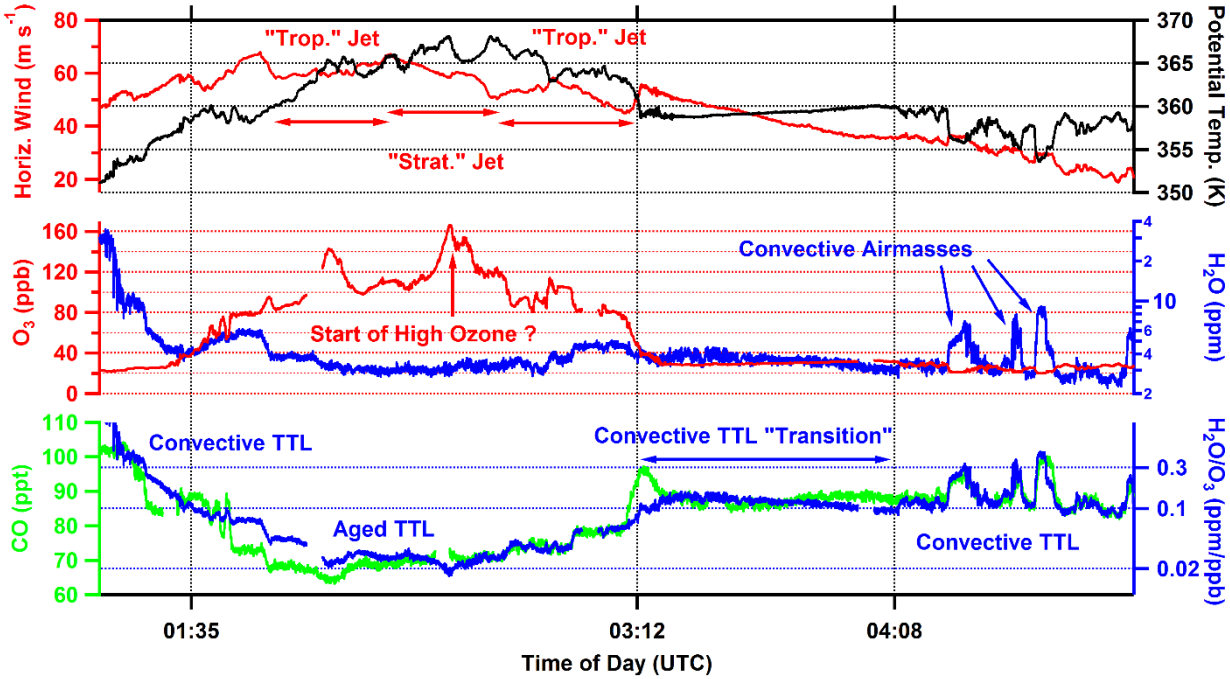

Figure S5: Same as Fig. 3 for RF06.

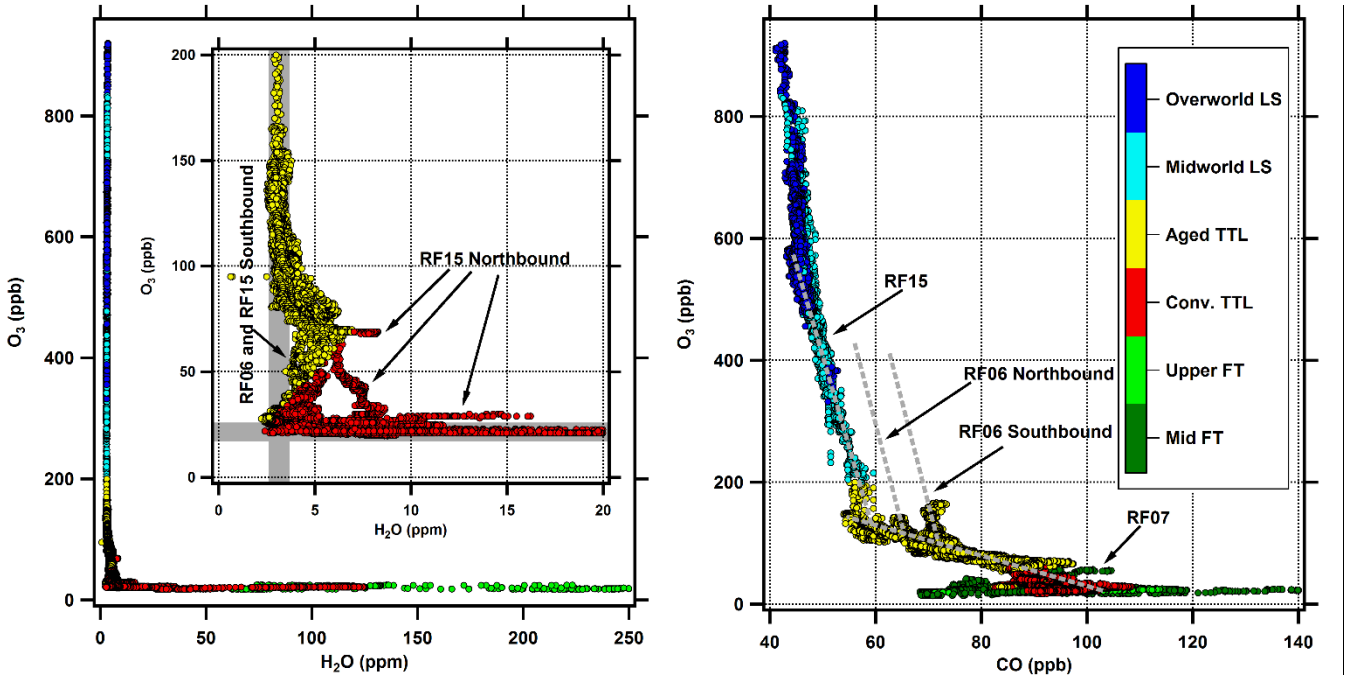

Figure S6: Air mass classification in the context of tracer-tracer classification schemes. Left panel, the scheme from Pan et al., 2014. Air masses that have neither stratospheric H_2O nor tropospheric O_3 (outside the grey regions) are in the TTL. Under such a scheme the convective TTL includes tropospheric air and the aged TTL includes stratospheric air. Right panel, the scheme from Chen et al., 2016, which defines a TTL-LMS transition where the slope between CO and O_3 is -0.4 (CO/O_3), this generally corresponds to the aged TTL in this work, but also includes portions of the convective TTL and a low altitude filament from RF07. Some aged TTL air masses fall on parallel lines with a CO/O_3 slope of -0.03 consistent with the stratosphere in the Chen et al. scheme.

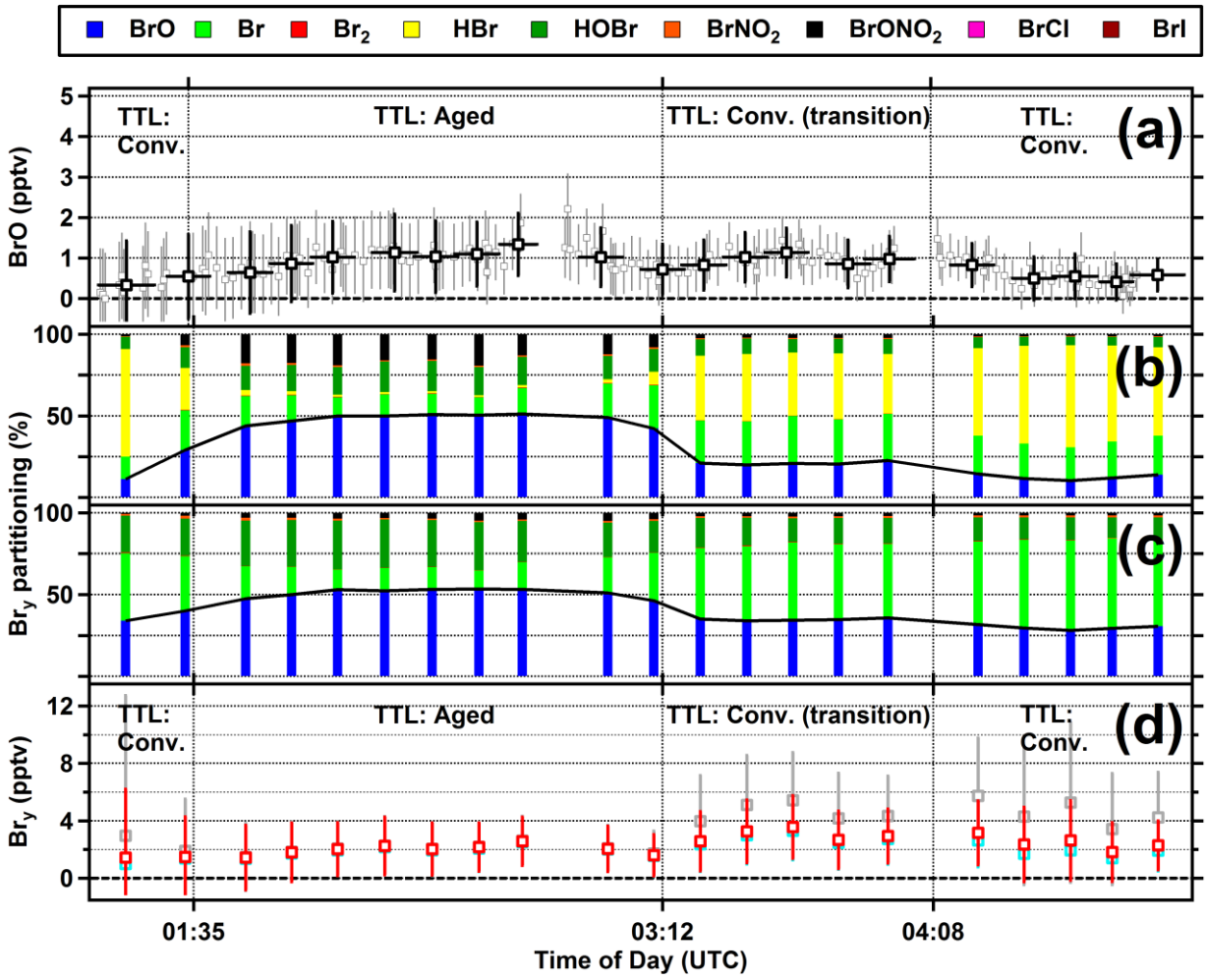

Figure S7: Same as Fig. 4 for RF06.

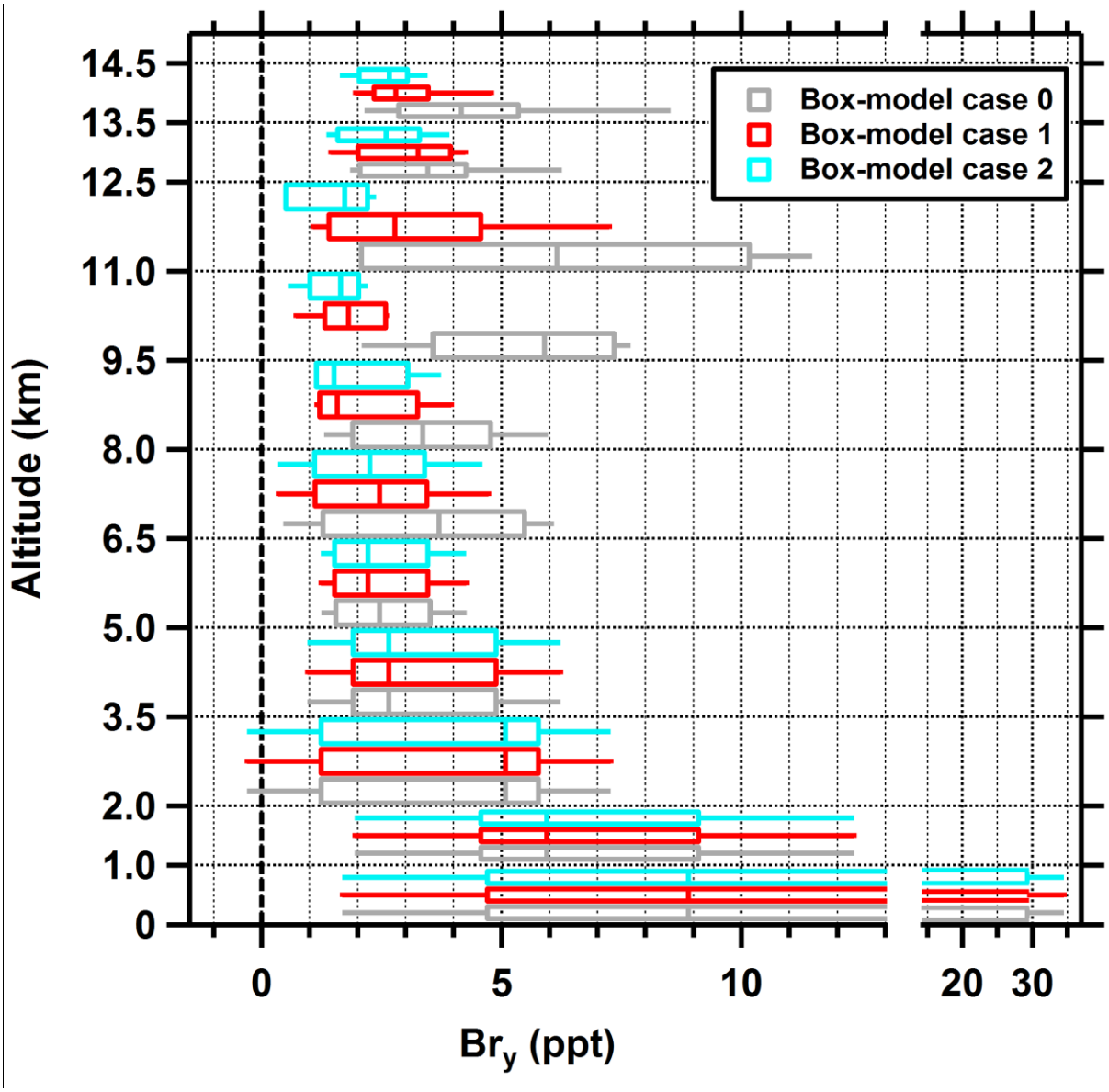

Figure S8: Comparison of modeled Br_y for different box model cases: (grey) case 0, (red) case 1, and (cyan) case 2. Boxes indicate the 25th and 75th percentiles and whiskers indicate the 10th and 90th percentiles. All statistics are computed across the altitudes indicated by the horizontal dashes. The different cases are offset vertically in each box for better visualization.

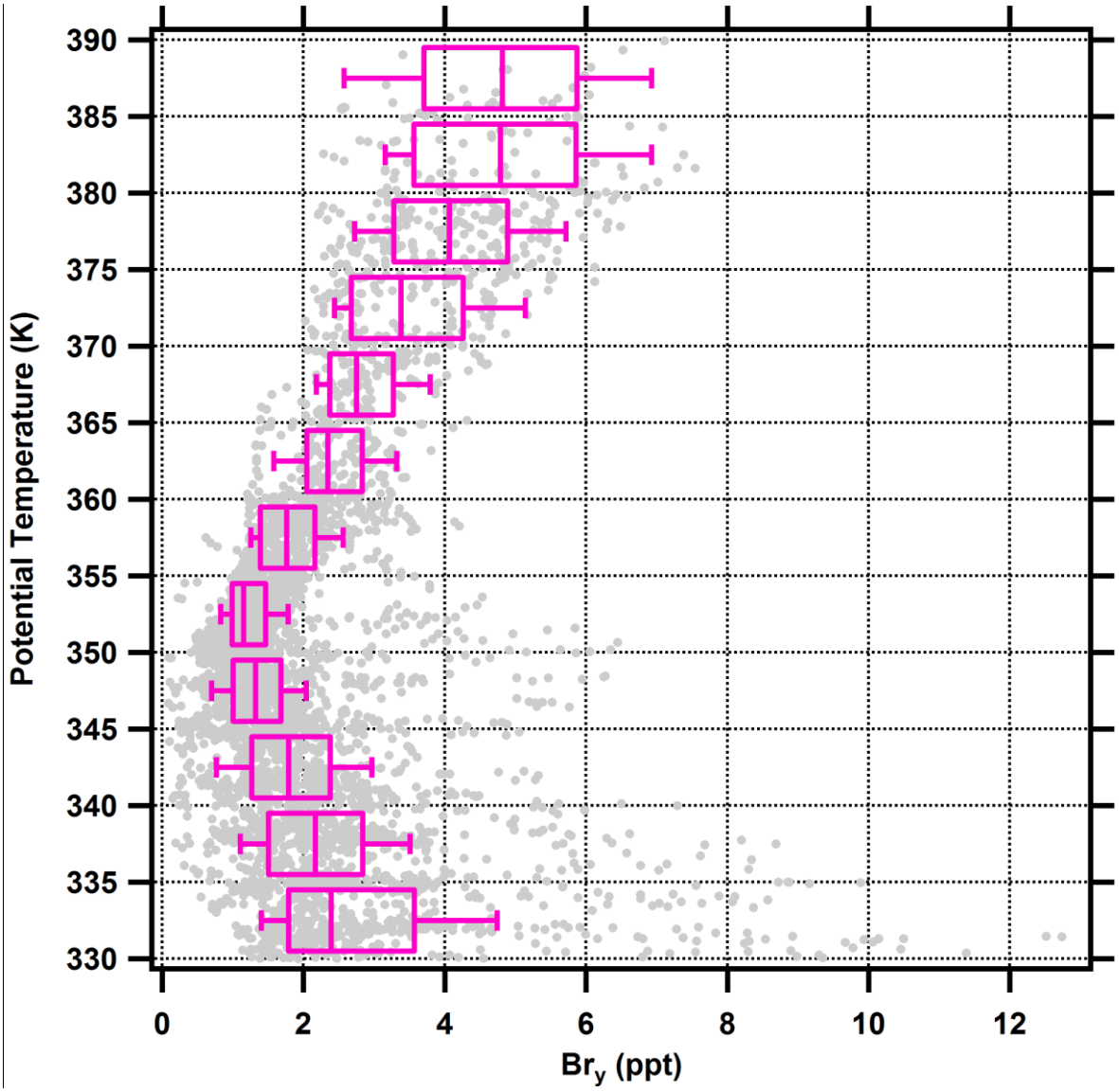

Figure S9: Br$_y$ from CAM-chem for the flights discussed in this work. Grey points in background are individual data points from the extraction, red boxes represent medians, 25th and 75th percentiles, whiskers indicate 10th and 90th percentiles. Consistent with the observations, a Br$_y$ minimum is found in the UTLS, though unlike the observations, at lower θ. CAM-chem has a median (quartile range) of 1.2 (1.0, 1.5) ppt Br$_y$ near 350-355 K, and 2.3 (2.0, 2.8) ppt for 360-365 K. The median and quartile range are consistent with the observed Br$_y$ minimum for 360-365 K, but less Br$_y$ is predicted at lower θ.

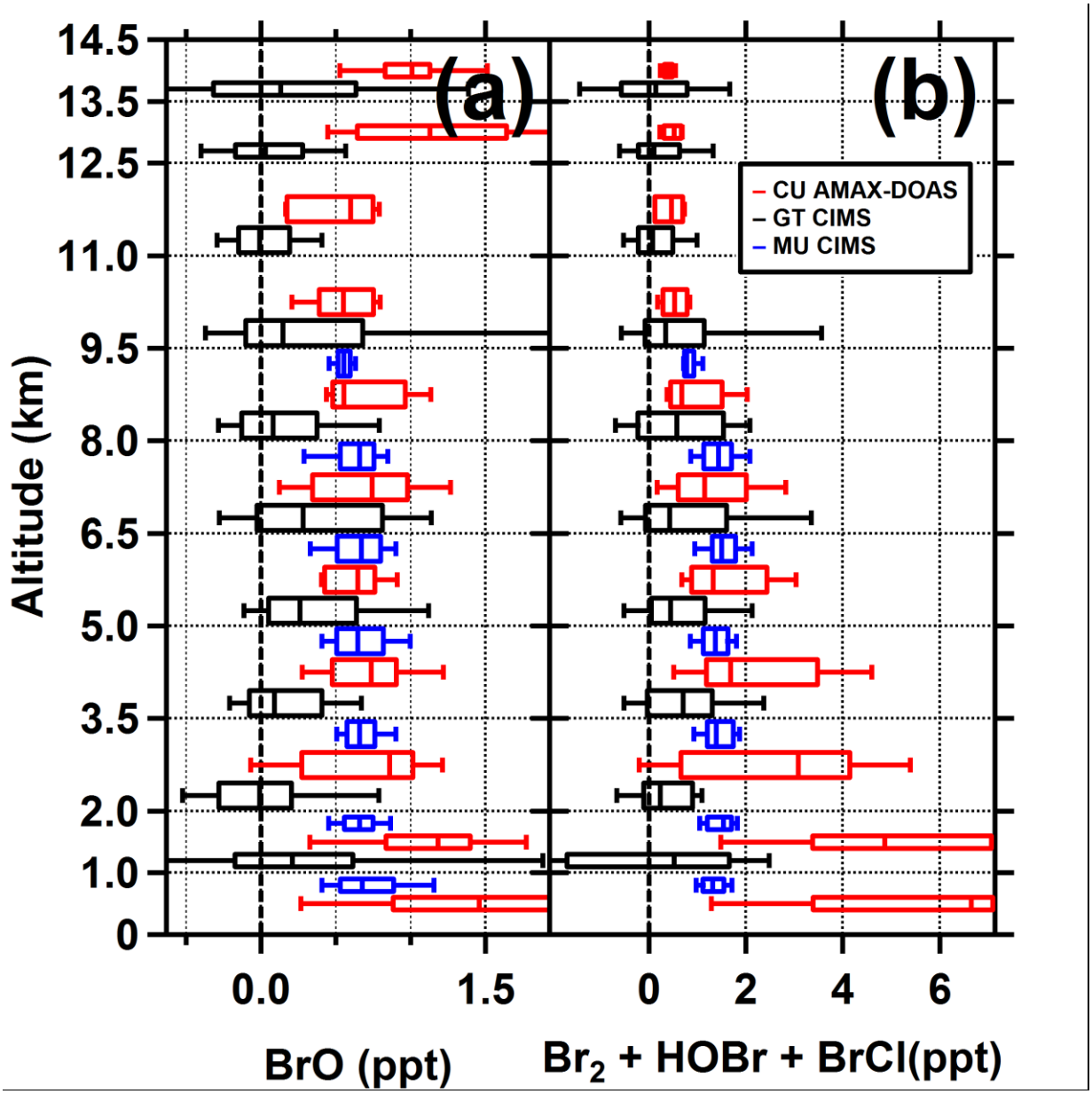

Figure S10: Comparison of bromine measurements by the CU Boulder AMAX-DOAS (blue), Georgia Tech CIMS (Chen et al., 2016) (black) aboard the NSF/NCAR GV during CONTRAST, and the Manchester University CIMS (Le Breton et al., 2017) (red) aboard the FAAM aircraft during CAST. Data are presented as box and whisker plots, where boxes show the interquartile range and median, and whiskers show the 10th and 90th percentile. (a) BrO measurements. Data for the CONTRAST instruments are filtered to exclude stratospheric data (using the LS definition described in the main text). (b) Other Br$_y$ species. Manchester reports Br$_2$, HOBr, and BrCl separately, these are added and statistics gathered on the resulting sum. Georgia Tech reports a single value for the sum of Br$_2$ and HOBr. AMAX-DOAS values are inferred using the box model (case 1), and taken as the sum Br$_2$+HOBr (the model was run with zero chlorine and hence zero BrCl).

References

Andrews, S. J., Carpenter, L. J., Apel, E. C., Atlas, E., Donets, V., Hopkins, J. F. R., Hornbrook, R. S., Lewis, A. C., Lidster, R. T., Lueb, R., Minaeian, J., Navarro, M., Punjabi, S., Riemer, D. and Schauffler, S. S.: A comparison of very short-lived halocarbon (VSLS) and DMS aircraft measurements in the Tropical West Pacific from CAST , ATTREX and CONTRAST, Atmos. Meas. Tech., 9(10), 5213–5225, doi:10.5194/amt-2016-94, 2016.

Apel, E. C., Hills, A. J., Lueb, R., Zindel, S., Eisele, S. and Riemer, D. D.: A fast-GC/MS system to measure C_2 to C_4 carbonyls and methanol aboard aircraft, J. Geophys. Res., 108(D20), 8794, doi:10.1029/2002JD003199, 2003.

Apel, E. C., Emmons, L. K., Karl, T., Flocke, F., Hills, A. J., Madronich, S., Lee-Taylor, J., Fried, A., Weibring, P., Walega, J., Richter, D., Tie, X., Mauldin, L., Campos, T., Weinheimer, A., Knapp, D., Sive, B., Kleinman, L., Springston, S., Zaveri, R., Ortega, J., Voss, P., Blake, D., Baker, A., Warneke, C., Welsh-Bon, D., de Gouw, J., Zheng, J., Zhang, R., Rudolph, J., Junkermann, W. and Riemer, D. D.: Chemical evolution of volatile organic compounds in the outflow of the Mexico City Metropolitan area, Atmos. Chem. Phys., 10(5), 2353–2375, doi:10.5194/acp-10-2353-2010, 2010.

Apel, E. C., Hornbrook, R. S., Hills, A. J., Blake, N. J., Barth, M. C., Weinheimer, A., Cantrell, C., Rutledge, S. A., Basarab, B., Crawford, J., Diskin, G., Homeyer, C. R., Campos, T., Flocke, F., Fried, A., Blake, D. R., Brune, W., Pollack, I., Peischl, J., Ryerson, T., Wennberg, P. O., Crounse, J. D., Wisthaler, A., Mikoviny, T., Huey, G., Heikes, B., O'Sullivan, D. and Riemer, D. D.: Upper tropospheric ozone production from lightning NOx -impacted convection: Smoke ingestion case study from the DC3 campaign, J. Geophys. Res. Atmos., 120(6), 2505–2523, doi:10.1002/2014JD022121, 2015.

Le Breton, M., Bannan, T. J., Shallcross, D. E., Khan, M. A., Evans, M. J., Lee, J., Lidster, R., Andrews, S., Carpenter, L. J., Schmidt, J., Jacob, D., Harris, N. R. P., Bauguitte, S., Gallagher, M., Bacak, A., Leather, K. E. and Percival, C. J.: Enhanced ozone loss by active inorganic bromine chemistry in the tropical troposphere, Atmos. Environ., 155, 21–28, doi:10.1016/j.atmosenv.2017.02.003, 2017.

Cai, Y., Montague, D. C., Mooiweer-Bryan, W. and Deshler, T.: Performance characteristics of the ultra high sensitivity aerosol spectrometer for particles between 55 and 800nm: Laboratory and field studies, J. Aerosol Sci., 39(9), 759–769, doi:10.1016/j.jaerosci.2008.04.007, 2008.

Cazorla, M., Wolfe, G. M., Bailey, S. A., Swanson, A. K., Arkinson, H. L. and Hanisco, T. F.: A new airborne laser-induced fluorescence instrument for in situ detection of formaldehyde throughout the troposphere and lower stratosphere, Atmos. Meas. Tech., 8(2), 541–552, doi:10.5194/amt-8-541-2015, 2015.

Chen, D., Huey, L. G., Tanner, D. J., Salawitch, R. J., Anderson, D. C., Wales, P. A., Pan, L. L., Atlas, E. L., Hornbrook, R. S., Apel, E. C., Blake, N. J., Campos, T. L., Donets, V., Flocke, F. M., Hall, S. R., Hanisco, T. F., Hills, A. J., Honomichl, S. B., Jensen, J. B., Kaser, L., Montzka, D. D., Nicely, J. M., Reeves, J. M., Riemer, D. D., Schauffler, S. M., Ullmann, K., Weinheimer, A. J. and Wolfe, G. M.: Airborne measurements of BrO and the sum of HOBr and Br_2 over the Tropical

West Pacific from 1 to 15 km during the CONvective TRansport of Active Species in the Tropics (CONTRAST) experiment, J. Geophys. Res. Atmos., 121(20), 12,560-12,578, doi:10.1002/2016JD025561, 2016.

Gerbig, C., Schmitgen, S., Kley, D., Volz-Thomas, A., Dewey, K. and Haaks, D.: An improved fast-response vacuum-UV resonance fluorescence CO instrument, J. Geophys. Res. Atmos., 104(D1), 1699–1704, doi:10.1029/1998JD100031, 1999.

Holm, S.: A Simple Sequentially Rejective Multiple Test Procedure, Scand. J. Stat., 6, 65–70, doi:10.2307/4615733, 1979.

Lance, S., Brock, C. A., Rogers, D. and Gordon, J. A.: Water droplet calibration of the Cloud Droplet Probe (CDP) and in-flight performance in liquid, ice and mixed-phase clouds during ARCPAC, Atmos. Meas. Tech, 3(6), 1683–1706, doi:10.5194/amt-3-1683-2010, 2010.

Mann, H. B. and Whitney, D. R.: On a Test of Whether one of Two Random Variables is Stochastically Larger than the Other, Ann. Math. Stat., 18(1), 50–60, doi:10.1214/aoms/1177730491, 1947.

Navarro, M. A., Atlas, E. L., Saiz-Lopez, A., Rodriguez-Lloveras, X., Kinnison, D. E., Lamarque, J.-F., Tilmes, S., Filus, M., Harris, N. R. P., Meneguz, E., Ashfold, M. J., Manning, A. J., Cuevas, C. A., Schauffler, S. M. and Donets, V.: Airborne measurements of organic bromine compounds in the Pacific tropical tropopause layer., Proc. Natl. Acad. Sci. U. S. A., 112(45), 13789–13793, doi:10.1073/pnas.1511463112, 2015.

Pilewskie, P., Pommier, J., Bergstrom, R., Gore, W., Howard, S., Rabbette, M., Schmid, B., Hobbs, P. V. and Tsay, S. C.: Solar spectral radiative forcing during the Southern African Regional Science Initiative, J. Geophys. Res. Atmos., 108(D13), doi:10.1029/2002JD002411, 2003.

Schauffler, S. M., Atlas, E. L., Blake, D. R., Flocke, F., Lueb, R. A., Lee-Taylor, J. M., Stroud, V. and Travnicek, W.: Distributions of brominated organic compounds in the troposphere and lower stratosphere, J. Geophys. Res. Atmos., 104(D17), 21513–21535, doi:10.1029/1999JD900197, 1999.

Shetter, R. E. and Müller, M.: Photolysis frequency measurements using actinic flux spectroradiometry during the PEM-Tropics mission: Instrumentation description and some results, J. Geophys. Res. Atmos., 104(D5), 5647–5661, doi:10.1029/98JD01381, 1999.

Volkamer, R., Baidar, S., Campos, T. L., Coburn, S., DiGangi, J. P., Dix, B., Eloranta, E. W., Koenig, T. K., Morley, B., Ortega, I., Pierce, B. R., Reeves, M., Sinreich, R., Wang, S., Zondlo, M. A. and Romashkin, P. A.: Aircraft measurements of BrO, IO, glyoxal, NO_2, H_2O, O_2–O_2 and aerosol extinction profiles in the tropics: comparison with aircraft-/ship-based in situ and lidar measurements, Atmos. Meas. Tech., 8(5), 2121–2148, doi:10.5194/amt-8-2121-2015, 2015.

Zondlo, M. A., Paige, M. E., Massick, S. M. and Silver, J. A.: Vertical cavity laser hygrometer for the National Science Foundation Gulfstream-V aircraft, J. Geophys. Res., 115(D20), D20309, doi:10.1029/2010JD014445, 2010.